JIANG, Zongyu

Experimental investigation of ice loads on vertical and slope offshore structures

Master's thesis submitted in partial fulfillment of the requirements for the degree of Master of Science in Technology.

Espoo 30.07.2020
Supervisor: Professor KUJALA, Pentti (Aalto University)
            Professor HØYLAND, Knut Vilhelm (NTNU)

Author JIANG, Zongyu

Title of thesis Experimental investigation of ice loads on vertical and slope offshore structures

Abstract

An experiment was carried out to study the ice loads of level ice and ridge on the vertical and slope structures. The prototype of the model is the lighthouse Nordströmsgrund, which is a vertical structure and locates in the north Baltic sea. Nevertheless, a conical part was added to the model to study the ice loads on slope structures in addition to the study of the ice loads on vertical structures. Three ice sheets with ridges were targeted to design the ice condition around Nordströmsgrund, including the flexural strength, ice thickness, geometrical cross-sectional profile of ridge, etc. Every ice sheet had a constant thickness, ranging from 0.04m to 0.043m in model-scale, but its flexural strength could be changed by using tempering procedure. Eight tests were successfully conducted and the ice loads were measured and recorded with three components divided according to the Cartesian coordinate system. The effect of ice properties and degrees of consolidation were also observed and analyzed with the measured data.

The history curve and its envelope were utilized to study the ice loads on structures. The ice loads were decomposed into rubble loads (loads induced by accumulated rubbles) and level ice/consolidated layer loads (loads induced by breaking the level ice/consolidated layer). The upper envelope was assumed to represent the total ice loads and the lower envelope was assumed to represent the rubble loads. Thus, the difference between the upper and lower envelopes could be considered the level ice/consolidated layer loads. Fast Fourier Transform is applied to study the energy distribution of ice loads. The splitting of level ice was observed in front of the ridge at three tests. The histogram and return period are employed to study the distribution of ice loads and affecting parameters.

The most important discovery of this research was that the horizontal range of rubbles moved by the structure had stronger influence on the ice ridge loads than the depth of rubble accumulation in front of the structure. Actually, the ridge loads were proportional to the volume of rubble accumulation and the strength of freeze bond in the keel. The zigzag pattern in the curve of horizontal range reflected the process of breaking the keel. This resulted in that the accumulation volume increased with a zigzag pattern in the curve of volume against the structure's penetration distance into the ridge.

Preface

This thesis is submitted for the degree of Master of Science as a final report of the education at Aalto University and NTNU.

This thesis is dedicated to analyze the data from model tests conducted in the Aalto Ice Tank. The work was carried out under the supervision of Professor Knut V. Høyland and Professor Pentti Kujala. These two supervisors have distinctive styles of instruction. Professor Høyland always helped me discover interesting points and inspired me to find the solution on myself. In contrast, Professor Kujala showed me many ideas which helped me discover potential solutions. Even though the ways are different, they all effectively strengthen my capability of scientific research.

I first encountered the issue of sea ice in a project of offshore wind farm in the Bohai Bay, China. The ice mechanics is challenging and interesting, which encouraged me to look for an opportunity to study it with a systematic training. The programme of Nordic Master in Cold Climate Engineering offered me such precious opportunity. During the two-years' study, I have learnt much knowledge about ice and ice mechanics from a number of world-class scholars in Aalto University and NTNU.

While studying at Aalto, I also worked as a research assistant in Professor Kujala's team. This team has a dynamic and creative spirit, which makes a deep impression on me. All team members provided a lot of support to help me complete my assignment. Especially, Li Fang, a PhD candidate, helped me a lot with invaluable discussions and suggestions when I compiled the paper published in POAC 2019.

When I studied at NTNU, the main work was to analyze the ice loads data of the experiment. Dr. Otto Puolakka, the manager of Aalto Ice Tank, and PhD candidate Evgenii Salganik helped me a lot on the data and document collection.

Besides the people mentioned above, there are a lot of people I shall express my gratitude to for their assistance to achieving my second Master degree. For example, Dr. Lu Wenjun, PhD candidate Lv Chuangxin and PhD candidate Li Hongtao showed me a lot of valuable information about how to reach the research resource at NTNU. Without their great help, my journey of pursuing the Master degree could not be so smooth, especially in the crazy year with COVID-19.

I also should express my gratitude to the team of Cold Climate Engineering programme: Professor Arttu Polojärvi, Professor Gunvor M. Kirkelund, and Professor Jukka Tuhkuri. Without their invaluable work, I could not achieve the opportunity of absorbing the knowledge of ice and ice mechanics.

Finally, I wish to thank my wife Liu Jie for discussing problems of statistics and other scientific issues, and my parents for their silent but enormous love. Even though I am thousands of miles away from my parents, I know they are there, standing like mountains.

Espoo 30.07.2020

JIANG, Zongyu

Contents

List of Figures

List of Tables

x

1 Introduction

Along with the development of global warming, the extent of ice coverage in the Arctic area is obviously reduced at the dimensions of time and space. As a result, the activities of human being are increasingly frequent in the Arctic area. More offshore, coastal structures and ships are deployed in the cold region where human being seldom visited in the past. For example, the Northern Sea Route currently attracts many countries' attention due to its promising advantage to the global economy. It can be predicted that more ships will commute between the Asia-Pacific countries and European countries in the near future. The demand of coastal infrastructures will also increase to satisfy the more intensive shipping activity.

Fig. 1.1 Northern Sea Route (Source: https://www.economist.com/)

The marine structures and ships inevitably face the threat of sea ice. The ice loads can damage the structures, locally and globally. The prediction of ice loads has huge uncertainty due to the complicated micro structure of sea ice and its various formation. The complex of ice structure results in complicated and various failing mechanisms of sea ice, which tremendously increase the difficulty of predicting the ice loads. Therefore, a large amount of research is required to improve our understanding of sea ice and the precision of ice loads prediction. It is necessary and essential to enhance the safety of marine structures running in the Arctic and cold area.

So far, a large number of structures have been deployed in the cold region, where the ice load is an important factor that should be seriously considered while designing the structures. Figure 1.2 shows some examples of these structures (lighthouse, bridge pier, wind turbine and oil & gas platform). It is predictable that human being will develop more structures in the Arctic sea area and many of them will be column-type. For example, the offshore wind farm is booming in the last two decades because it brings a new and promising source of the renewable power. The Arctic region could be an ideal place for the offshore wind farm due to its rich wind resource.
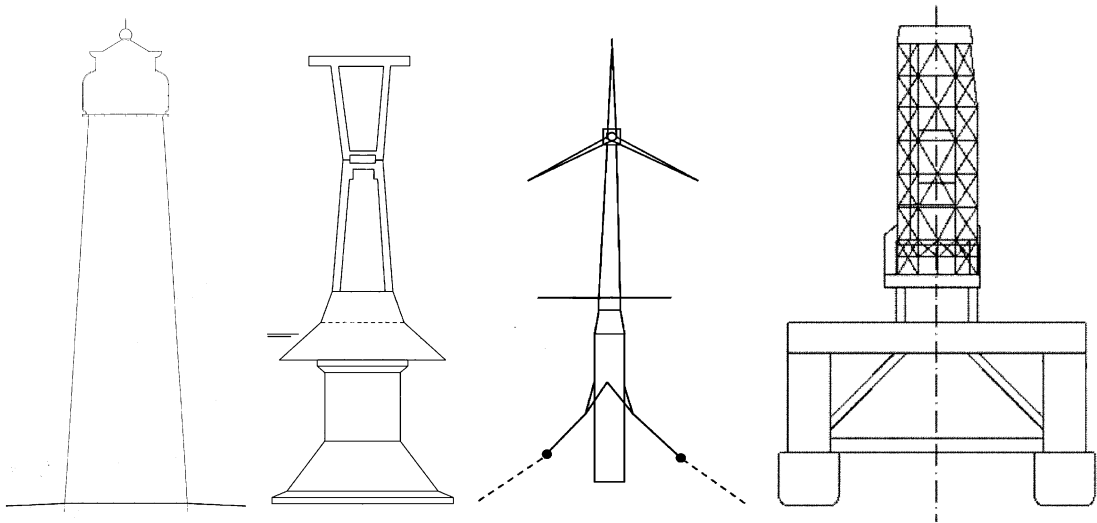
Fig. 1.2 Example of marine structures existing in the cold region

When the ice floes cover 70% sea surface and above, the floes will compress and / or scratch each other and finally generate ice ridges. The ice floes and ridges can be drift by wind and current and induce horizontal loads on the marine structures. It is known that the slope structures experience less ice loads than the vertical structures (Ralston, 1977). However, the mechanism and ice-structure interaction process are not well understood and described due to the complexity of ice material and interaction process.

So far, the techniques employed to study the ice loads could be divided into three groups: 1) theoretical-empirical studies, 2) full-scale investigation, and 3) model-scale experiments.

The theoretical-empirical methods have been developed based on the systematic observation and mechanical theories. However, the formulas are restricted to ideal ice conditions and structural configurations. It is difficult to extend the semi-empirical formulas to normal ice conditions or structures because the formulas only consider certain empirical parameters. In addition, the ice action contains many ice failure mechanisms in real engineering cases. Thus, the semi-empirical approaches can only provide conservative predictions. Therefore, the full-scale and model-scale tests are employed to achieve more reliable and precise data.

The full-scale tests are carried out in field so they can measure the ice structure interaction and ice loads with parameters of the real world. They reflect the real behavior of structures undergoing the ice loads. However, it is difficult to control the test parameters and boundary conditions. It is also difficult to precisely measure the field conditions. Consequently, the data achieved from in-situ tests are difficult to analyze. Furthermore, the full-scale test requires a large financial support, which results in the scarcity of reported full-scale data.

The model-scale experiments have the advantages at various aspects, which are exactly disadvantages of full-scale investigation. It is easier to control the test parameters and boundary conditions. As a result, the systematic parameter study can be conducted to analyze the effect of specific parameters. The cost of model-scale experiments is lower than the full-scale investigations. The model-scale experiments have disadvantages as well. For example, it is difficult to precisely reproduce the ice conditions in the real world. It is hard to apply appropriate scales to every concerned physical parameter.

Therefore, the ice-structure interaction could be better investigated and comprehended if multiple techniques are employed to the study. This thesis reports an investigation of ice loads on marine structures by using a series of model basin tests, which were conducted to systematically study the effect of cone on the loads of level ice and ridge.

This model-scale tests studied the ice loads on the round section structures in the condition of level ice and ice ridge. Two types of structures were conducted to the ice conditions: 1) cylindrical structures, with a shell perpendicular to the level ice; 2) conical structures, with a shell intersecting the level ice at the angle of 74.8 degree to the level ice. With these two types of structures, a comparative research was conducted to study the ice loads on the vertical structure and slope structure. In this research, the ice loads are divided into two groups: 1) loads induced by breaking the level ice; 2) loads induced by the ice ridge. For both groups, the influence of structure type is analyzed in time domain. The energy distribution of ice loads is analyzed by using the Fast Fourier Transform in frequency domain. The ice structure interaction is analyzed by using the distribution and return period of peak value of ice load in every oscillating cycle.

Six cameras were installed above and under water to observe the process of ice breaking and rubble accumulation around the structure. The most interesting observation is that the rubble loads are more closely connected to the maximum horizontal range of rubbles pushed by the structure rather than the depth of accumulation.

The research is presented with the following chapters:

Chapter 1: This chapter introduces the application background, motivation, objective of this research.

Chapter 2: This chapter presents the theory background and literature review relevant to this research, including level ice and ridge properties, ice failing mechanisms, ice loads prediction, etc.
Chapter 3: The experiment and full-scale measurement setups are presented in this chapter, including the ice tank, testing facilities, model ice type, level ice and ridge properties, structure profile, testing procedure, etc.

Chapter 4: The interested experimental data is processed and analyzed in this chapter. Firstly, the level ice loads are separated with their origin and analyzed by comparing the loads on vertical cylinder and conical cylinders. Secondly, the ridge loads are analyzed by comparing the loads on vertical cylinder and conical cylinders. At last, the ice load frequency is analyzed based on the failing mechanism of the ice while the ice interacted with different structure types.

Chapter 5: Summary of main findings and discussions are drawn out according to the analysis of experimental data combined with well-known and proved theories and knowledge. The experimental results are compared with other researches and theoretical models. It is clearer to understand how the cylindrical / conical structures interact with the level ice and ice ridges.

Chapter 6: Conclusions

2 Theoretical background and literature review

This chapter describes the knowledge and research development related to this research. Firstly, the material properties of level ice and ridge are introduced because these properties, like flexural strength, compressive strength, ice thickness, etc., define the strength of the ice, which can strongly influence the amplitude of ice loads (Tuhkuri, 2018). Secondly, some ice failure modes are described with the affecting factors. Generally, the ice loads occur along with the procedure of ice failure. Different failure modes can generate different ice loads. Thus, to study the ice failure modes could be of great help to investigate the ice loads. The ice loads are also closely related to the structural forms because the forms could affect the ice failure modes or the weighing of the combination of failure modes. This is the content of the third section. At last, some theories and methodologies of scale model testing are presented in the last section.

2.1 Formation and properties of level ice and ridge

In this section, the knowledge relevant to the experiment is described as the theory background. The thermodynamic theory of ice growth is described accompanied with the Stefan's law, which is introduced to predict the ice growth of level ice. This part of knowledge is of help to comprehend the formation of level ice sheet and consolidating procedure in this experiment. In addition, the ridging and rafting are described as the deformation of sea ice. This description and introduction are of help to understand the formation of the ridge in this experiment. At last, some ice properties relevant to the ice strength is presented, which is of help to understand the generation and tempering of level ice in the experiment.

2.1.1 Growth and structure of ice

To study the formation and growth of sea ice is to study the solidification of solutions of water with some NaCl and other salts. Typically, sea ice consists of

- ✧ ice
- ✧ brine
- ✧ no, one, or two salts depending on the temperature of the sea ice
- ✧ air bubbles

The sea ice formation and its properties are essentially influenced by salt and the amount of salt. The density of water depends on temperature and salinity. The temperature of density maximum depends on salinity. The relationship is inversely proportional. The freezing point of water is also inversely proportional to salinity, as shown in Fig. 2.1.
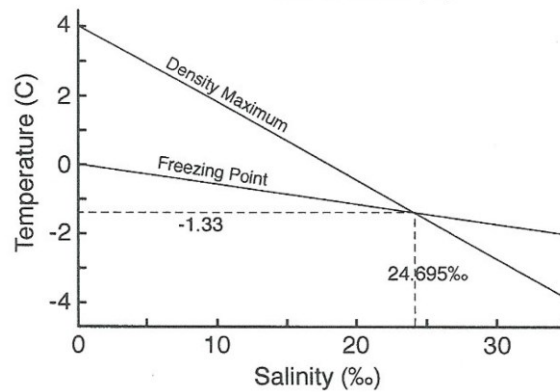
Fig. 2.1 Relationship between the salinity, density maximum and freezing point (Weeks, 2010).

As the water with a salinity over 24.7‰ cools, the density increases. As a result, the surface water sinks and replaced by warmer water below. This pattern of convection continues until the whole water column is at the freezing temperature and ice starts to form. Therefore, the temperature of water under the ice should be evenly close to the freezing point in the experimental tank.
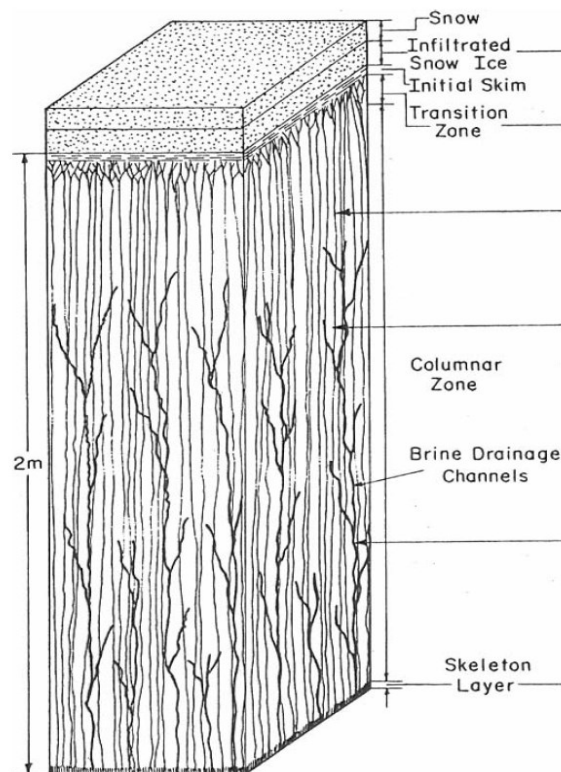
Fig. 2.2 Structure of sea ice (Gow and Tucker, 1991)

Figure 2.2 shows the structure of natural sea ice. The initial layer forms in clam water in the lab so the ice grain in this layer should be larger than that of natural sea ice, which is disturbed by sea waves and wind. When a continuous layer has formed, the freezing of ice is determined by heat flux. The heat flows from the warmer sea water to the cold air, through the ice layer. The growth of ice crystal is restricted by the neighboring crystals. Thus, the ice crystals prefer growing vertically, and consequently, their c-axis is horizontal. This procedure happens at the transition zone. As the ice thickness increases, the average grain diameter increases. As a result, the strength of ice decreases. This layer is called columnar

zone. The skeleton layer lays beneath the columnar zone and it is partially water and partially ice, as shown in Fig. 2.3, so the skeleton layer has the lowest strength.
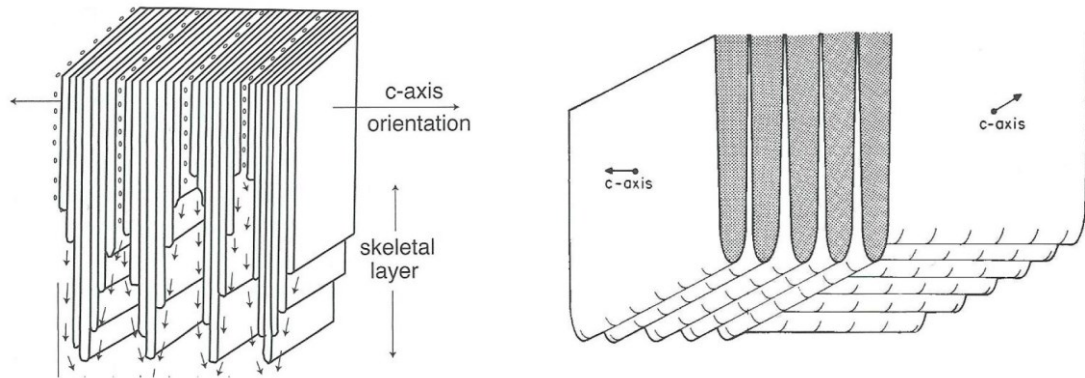
Fig. 2.3 The skeleton layer (Gow and Tucker, 1991)

Along with the growth of ice, the salt is ejected out of ice and the remaining solution (brine) contains more salt. The brine coexisting among ice can generate brine pocket and brine channel between basal planes. The salinity at the surface part is relatively high because the freezing rate is high and less brine is expelled. When the ice thickness increases, the speed of thermal transmission decreases. Thus, more brine can be expelled to the lower part of ice. Consequently, the salinity at bottom layer is higher than the middle part. Figure 2.4 shows an example of salinity profile of sea ice.
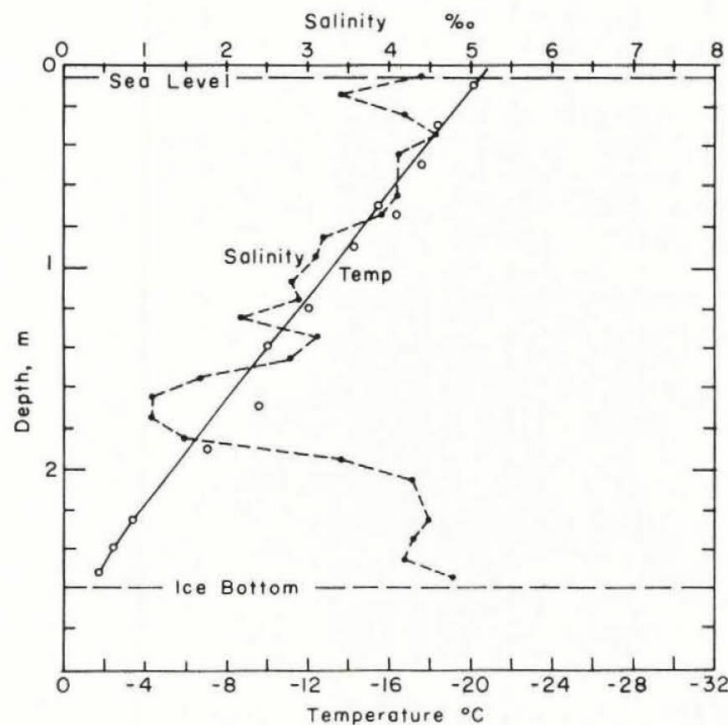
Fig. 2.4 Salinity and temperature profile of sea ice (Cox and Weeks, 1974)

2.1.2 The thermodynamics of ice growth and relevant theoretical models

The heat flux F from sea water to the cold air through the ice layer, as shown in Fig. 2.5.
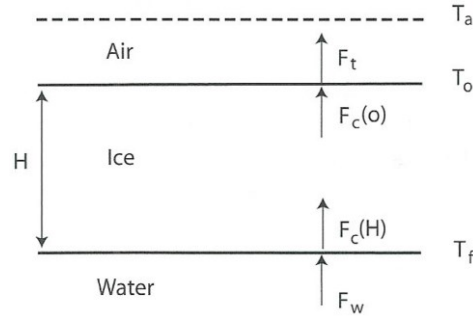
Fig. 2.5 Heat flux from sea water to cold air (Weeks, 2010)

According to the conservation of energy, $F_c(o) = F_c(H)$ and

$$F_c = k_i \frac{T_o - T_f}{H} \tag{2.1}$$

where H is thickness, k_i is the thermal conductivity, T_f is the freezing point of sea water, T_o is surface temperature. The ice is assumed thin enough so the temperature gradient through ice thickness can be considered linear.

Ice growth at the bottom of the sheet is determined by $F_c(H)+F_w$, where F_w is the heat flux from the sea. If this sum is negative, ice grows; if it is positive, ice melts. The ice growth is thus described through the equation

$$-\rho_i L \frac{dH}{dt} = F_c + F_w \tag{2.2}$$

where ρ_i is the density of ice and L is the latent heat of ice. When $F_w=0$, the following equation can be obtained

$$-\rho_i L \frac{dH}{dt} = k_i \frac{T_o - T_f}{H} \tag{2.3}$$

If the above equation is integrated and assume the temperature of ice surface is equal to the air temperature $T_o = T_a$,

$$H^2(t) - H_0^2 = \frac{2k_i}{\rho_i L} \int_0^t (T_f - T_a) dt \tag{2.4}$$

where $H(t)$ and H_0 are the current and the initial ice thickness. This equation is originally proposed by Stefan and named as Stefan' law (Weeks, 2010).

2.1.3 Deformation of level ice (rafting and ridging)

Ice sheets are often driven by forces of wind and current. In such condition, one ice sheet may be overridden by another ice sheet, which is called rafting. The rafting is easy to be observed in thin ice. When ice sheets, especially ice sheets with different thickness, move towards each other, it is easy to induce failure of ice sheets and ridging starts with accumulation of ice blocks. The cross section of ridge can be roughly divided into three parts: sail, keel and consolidated layer, as shown in Fig. 2.6. The keel consists of rubbles, which transforms from individual pieces with freeze bonds to a porous ice block field. The ice blocks directly beneath the sea surface can be frozen in to solid, which is called consolidated layer. The properties of consolidated layer are similar to the level ice. Ashton proposed an equation to evaluate the relationship between the level ice thickness and the consolidated layer thickness (Ashton, 1989)

$$h_{i,c} = \sqrt{\frac{2k_i}{\rho_i L_{i,c}} \int_0^t (T_f - T_a)dt + \left(\frac{k_i}{H_{ia}}\right)^2} - \frac{k_i}{H_{ia}} \tag{2.5}$$

where H_{ia} is the convectional heat transfer coefficient and $L_{i,c}$ is the latent heat of consolidated layer. The value of H_{ia} can be significantly increased by the sail of ridge because the sail increases the roughness of ridge top.
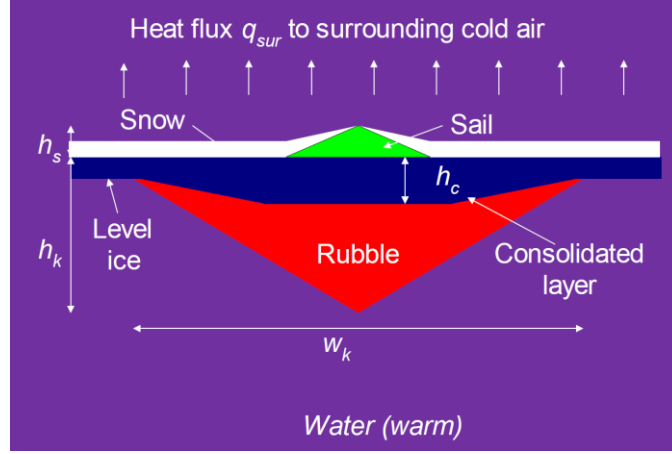
Fig. 2.6 Schematic cross-section of a First-year ice ridge (Høyland, 2019)

The thickness of consolidated layer is influenced by the porosity of ridge η and its relationship with the thickness of level ice can be estimated with the following equation (Leppäranta and Hakala, 1992; Høyland, 2002)

$$h_c^2 = h(t_0)_c^2 + \frac{h(t)_i^2 + h(t_0)_i^2}{\eta} \tag{2.6}$$

where the subscript c and i denote the consolidated layer and level ice, respectively. The equation 2.5 and 2.6 provide different ways to estimate the thickness of consolidated layer. The equation 2.5 estimates the thickness by considering the heat transferred from the water to the cold air whereas the equation 2.6 estimates the thickness of consolidated layer by using the thickness of surrounding level ice.

2.1.4 Properties of ice relevant to this experiment

The sea ice contains air bubbles and brine volume so it is porous. The porosity of ice is important for the thermo-mechanical behavior of ice. The total porosity η_T of sea ice is

$$\eta_T = \eta_a + \eta_b \tag{2.7}$$

where η_a is the porosity of air and η_b is the porosity of brine.

Simple measurements of ice temperature (T_i), ice salinity (S_i) and ice density (ρ_i) are used to derive the porosity. Cox and Weeks (1983) proposed the derivation for ice colder than -2 ^{o}C and Leppäranta and Manninen (1988) proposed another derivation for warm ice.

Brine volume is the amount of liquid present within the ice. Brine volume is a function of both ice salinity (S_i) and temperature (T_i)

$$\eta_b = S_i \left[\frac{49.185}{|T_i|} + 0.532\right] \tag{2.8}$$

where T_i in ^{o}C, $-22.9\ ^oC \leq T_i \leq -0.5\ ^oC$. The common unit of S_i and η_b is ‰.

Sea ice includes brine and has brine drainage channels, through which the brine can drainage while the ice is lift up from the sea. Thus, it is difficult to exactly measure the properties of sea ice.

The density of sea ice depends on temperature and salinity. Usually, the value of ice ranges from 720 to 940 kg/m^3. The variation is partially due to the actual characteristic of ice and another origin of variation is from the accuracy of different measurement techniques. According to situ measurement, the first-year sea ice has density from 840 to 910 kg/m^3 above the water line and from 900 to 940 kg/m^3 beneath the water line.

Ice fails in compression when it collides or presses the structure with surface perpendicular to the ice. The compressive strength of ice is much higher than another type of strength, such as the tensile strength. The compressive strength can be measured by the uniaxial compressing test. During the test, the load frame must be stiff enough because the ice could suddenly fail when brittle failure occurs, which is accompanied with sudden energy release. Stiff frame has large control of the ice failure because the stiff system stores less energy. In addition, the specimen ends need to be parallel within a small tolerance to maintain the compressive load in the axial direction of ice sample. The loading platens should not induce lateral constraint because it can generate a tri-axial stress state. Thirdly, Specimen size should be large enough to include a sufficient number of grains across the load bearing section.

The strain rate is an important factor to the compressive strength. It can also influence the stress-strain relationship and failure type, as shown in Fig. 2.7.
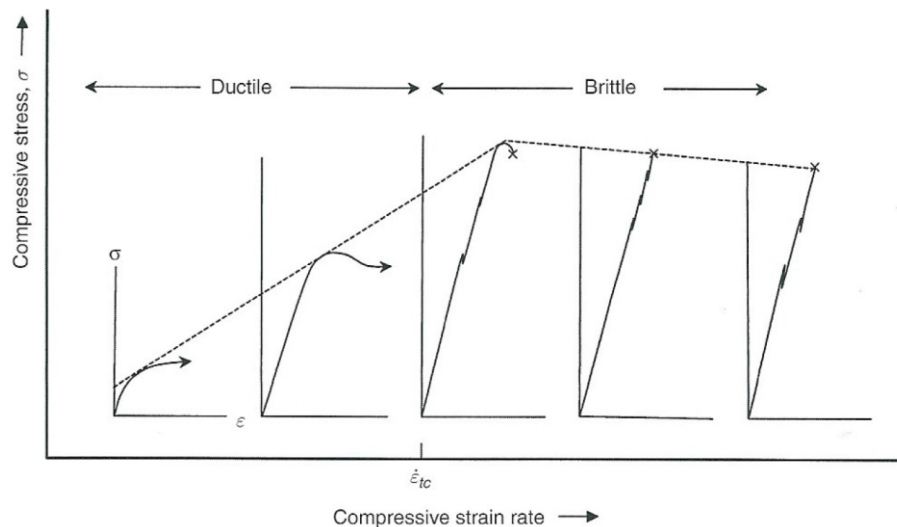
Fig. 2.7 Relationship between the strain rate and compressive strength. (Schulson and Duval, 2009)

Figure 2.7 shows the maximum value of ductile strength increases with increasing strain rate. A transition can be observed from ductile to brittle behavior when the strain rate exceeds some critical value. The transition occurs at an order of magnitude lower strain rate for vertical loading than horizontal loading according to the micro structure of ice. The ratio of vertical to horizontal strength is around 3.6 in the ductile regime and around 2 in the brittle regime.

Compressive strength has an inversely proportional relationship with the temperature and the total porosity (Vaudrey, 1975). Han et al. (2015) studied the uniaxial compressive strength of the Arctic summer sea ice. The results show that the uniaxial compressive strength decreases linearly with increasing total porosity. The dependence of the strength on

the temperature shows that the average strength in the brittle-ductile transition range increases steadily in the temperature range from −3 to −9°C.

Both the failure stress and the failure mode are sensitive to confinement (Weeks, 2010). Schulson et al. (1991) discovered that the influence of confinement is related to the level of confinement. For low levels of confinement, the fracture stress rises sharply with confinement. For higher levels, the fracture stress still rises, but less sharply.

In most cases, the flexural strength is employed to describe sea ice strength because the ice is destroyed by bending in many engineering applications. The flexural strength is the maximum tensile stress calculated with the measured maximum load and the beam dimensions. The flexural strength is just an index value but not a basic material property. The assumption is that the ice is homogenous and perfectly elastic.

Three different test set-ups have been used: cantilever beam, simple beam (3 and 4 points bending). The amount of work is large in situ measurement, especially when the ice is thick. The water influence can be measured at high loading rate in situ beams. Therefore, the test time should be approximately 1 second (Timco and Weeks, 2010; Schwarz et al., 1981; Aly, 2018). Maattanen (1975) also provided a correction factor to deal with the hydrodynamic effect.

The flexural strength decreases with increasing brine volume and temperature. Figure 2.7 shows the influence of brine volume and Fig. 2.9 presents the influence of temperature. Karulina et al. (2019) reported that the flexural strength decreases along with the increase of brine volume but the influence of temperature was not observed during their full-scale tests. Nevertheless, Han et al. (2015) observed the influence of temperature on fresh water ice as shown in Fig. 2.9.
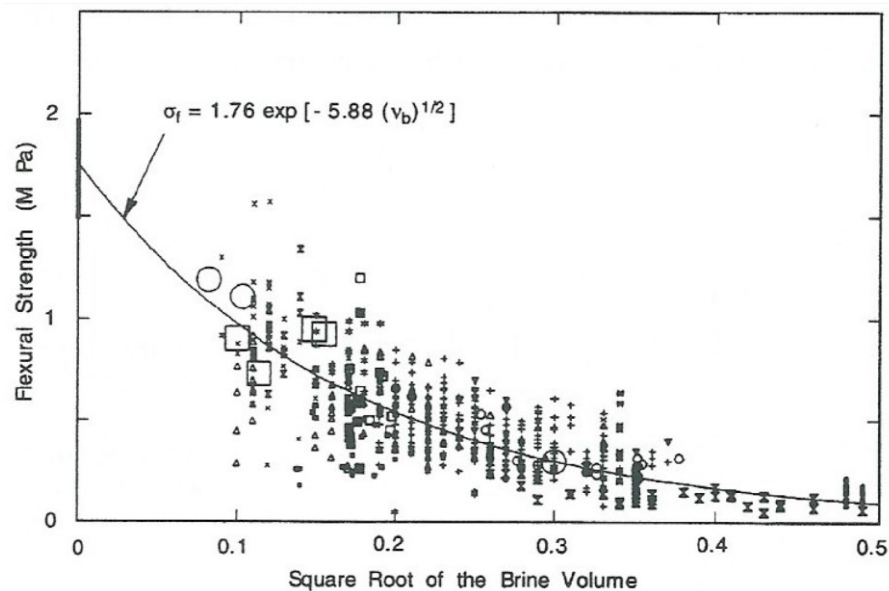
Fig. 2.8 Influence of the brine volume on the flexural strength (Weeks, 2010)
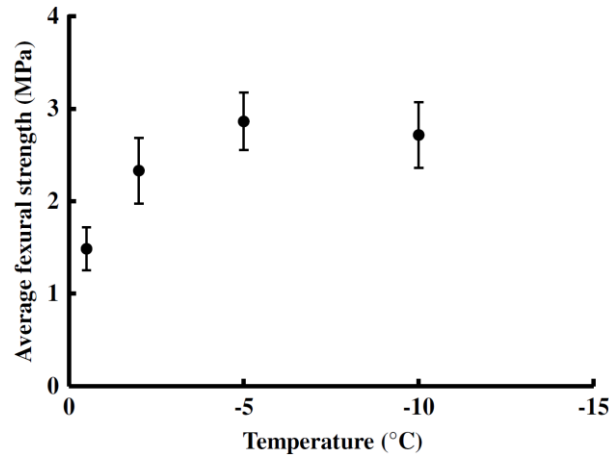
Fig. 2.9 Influence of the temperature on the flexural strength (Han et al., 2015)

The flexural strength of ice can be estimated by using the formula of the breaking of linear elastic beams

$$\sigma_f = \frac{6M}{bh^2} \tag{2.9}$$

where M denotes the breaking moment, b denotes the beam width, and h denotes the ice beam thickness.

However, this equation assumes the beam is isotropic and homogeneous, which is not in compline with the real sea ice because the sea ice contains air bubbles, brine bags, which strongly affect the flexural strength. Nadreau and Michel (1984) considered the influence of brine volume in the ice and proposed a formula to calculate the flexural strength

$$\sigma_f = 0.75\left(1 - \sqrt{\frac{\eta_b}{0.202}}\right) Mpa \tag{2.10}$$

where η_b denotes the porosity of brine. The porosity of brine is affected by the salinity and temperature so the flexural strength is indirectly affected by these two factors too. According to the same consideration, some scholars also proposed their formulas

Vaudrey (1977): $\qquad\qquad \sigma_f = 0.96 - 1.92\sqrt{\eta_b}\ \ Mpa \tag{2.11}$

Timco & O'Brien (1994): $\qquad \sigma_f = 1.76\exp\left(-0.588\sqrt{\eta_b}\ \right) Mpa \tag{2.12}$

2.2 Ice failure modes and affecting factors (creep, crushing, buckling, bending)

When the ice contacts the structures, ice forces are loaded on a structure due to relative movements between the structure and ice. As a result, various ice failure modes or their combination occurs in front of the structure. If the structure is vertical, the occurring of the failure modes is influenced by the indentation rate and aspect rate, as shown in Fig. 2.10. The indentation rate is the rate between the drifting velocity of ice and the characteristic dimension of structure (usually the width). The aspect rate is the rate between the characteristic dimension of structure and the ice thickness.
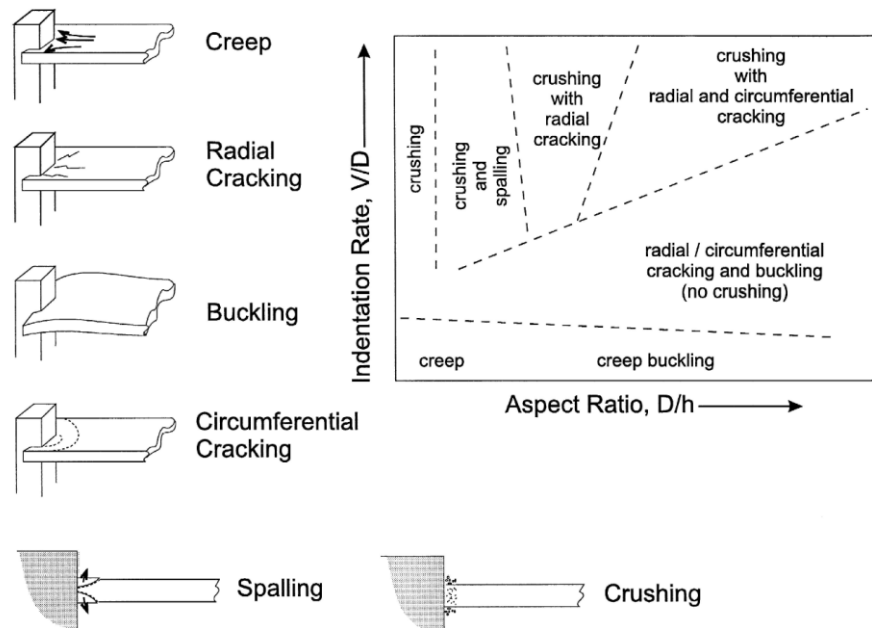
Fig. 2.10 Demonstration of ice failure modes and affecting factors (Daley, Tuhkuri, and Riska, 1998)

When the ice contacts the structure with low velocity, micro cracking evenly occurs through the ice thickness and small ice fragments evenly distribute along with the contacting surface. This phenomenon is called creeping. While the indenting velocity increases, the ice fragments close to the upper and lower surface of ice will be faked out but the micro cracking still happened at the middle layer of ice. The thickness of micro cracking layer continually decreases along with the increase of velocity. This phenomenon was firstly discovered by Joensuu & Riska in 1989. The typical contact mode is described in Fig. 2.12. Rist et al. (1994) studied the relationship between the micro cracking and ice strength by using triaxial apparatus. They observed that the shear fracture is rapid and unstable with no previous tensile failure.
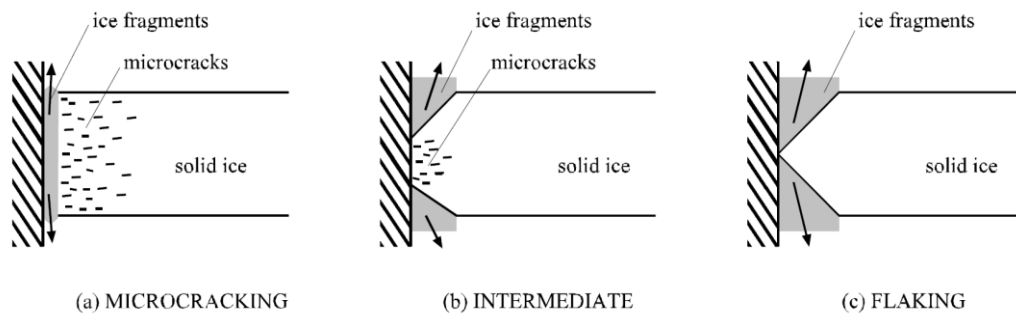
Fig. 2.11 Influence of indenting velocity
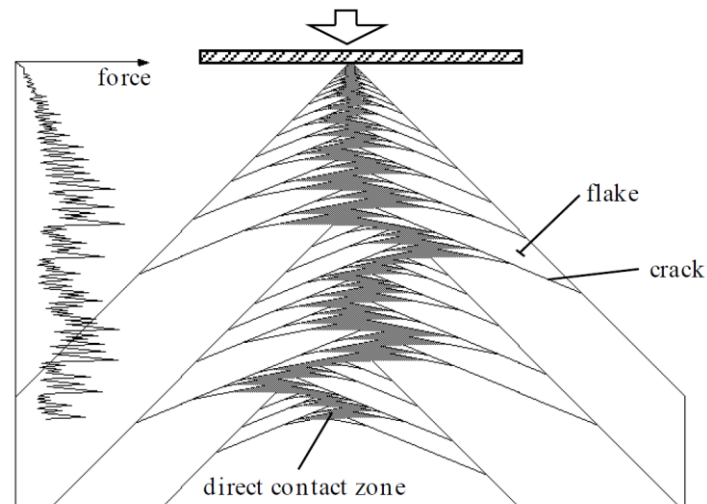
Fig. 2.12 Typical behavior of the CONTACT model (Daley, 1991)

Buckling occurs when the thin ice sheet, usually less than 0.4 m thick, contacts vertical structures, as shown in Fig. 2.13. One difference between the crushing and buckling is that the crushing is in-plane failure but the buckling is out-of-plane failure. The aspect ratio (the ratio between the structure width and the ice thickness) is another factor which strongly influences the ice breaking mode. When the thin ice contacts a wide structure, the ice sheet is favorable to buckle and finally fail when the buckling induced stress exceeds the tension strength at the surface of ice sheet. Sodhi, et al. (1983) reported an experimental study on the ice buckling against vertical structures. In the experiment, the ice sheet was pushed against structures with different widths. The results show good agreement with the theoretical values of normalized buckling loads for frictionless and hinged boundary conditions.
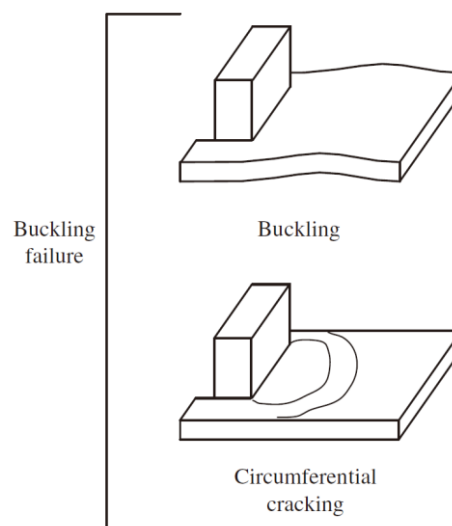
Fig. 2.13 Typical buckling failure in front of a vertical structure (Hendrikse and Metrikine, 2016)

When the ice sheet contacts the structure with slope side, the total load can be separated into two components: vertical force and horizontal force, as shown in Fig. 2.14. The vertical force generates a moment on the ice sheet and destroys the ice by bending. The capability of resisting the bending can be described and defined by the ice thickness and flexural strength. Thus, the failure mode of bending can be affected by the factors which influence the flexural strength of ice, such as temperature, porosity, strain rate, etc.
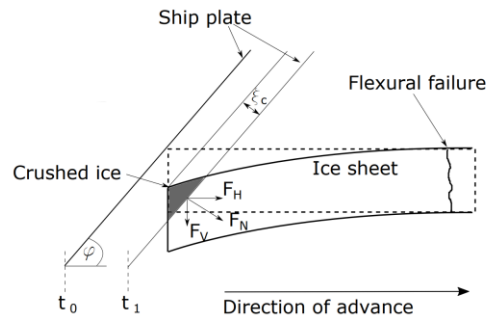
Fig. 2.14 Forces on ice sheet and flexural failure induced by bending (Varsta, 1983)

If the ice floe is not much larger than the characteristic dimension of the structure, the ice floe may fail in splitting during the interaction with the structure (Kärnä and Jochmann, 2003). It is considered that the limit size of ice floe reduces its lateral confinement, which could be the main reason of the splitting. However, it is still not fully clear that at what kind of conditions the splitting can happen. Michel (1978) reported the splitting failure is a kind of shear of tension cracking. Figure 2.15 shows a typical pattern of splitting in an ice floe with finite size. Recent research shows that the splitting can not only occur under the interaction with vertical structures but also under the interaction with slope structures (Lu et al., 2015). One observation of splitting is shown in Fig. 2.16, which is induced by an icebreaker.
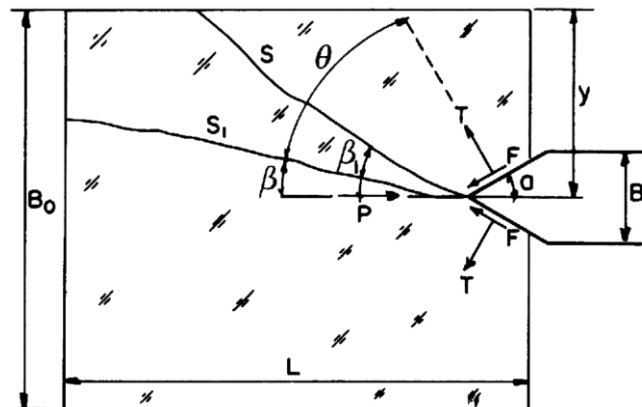
Fig. 2.15 Typical splitting of an ice floe induced by a structure (Michel, 1978)
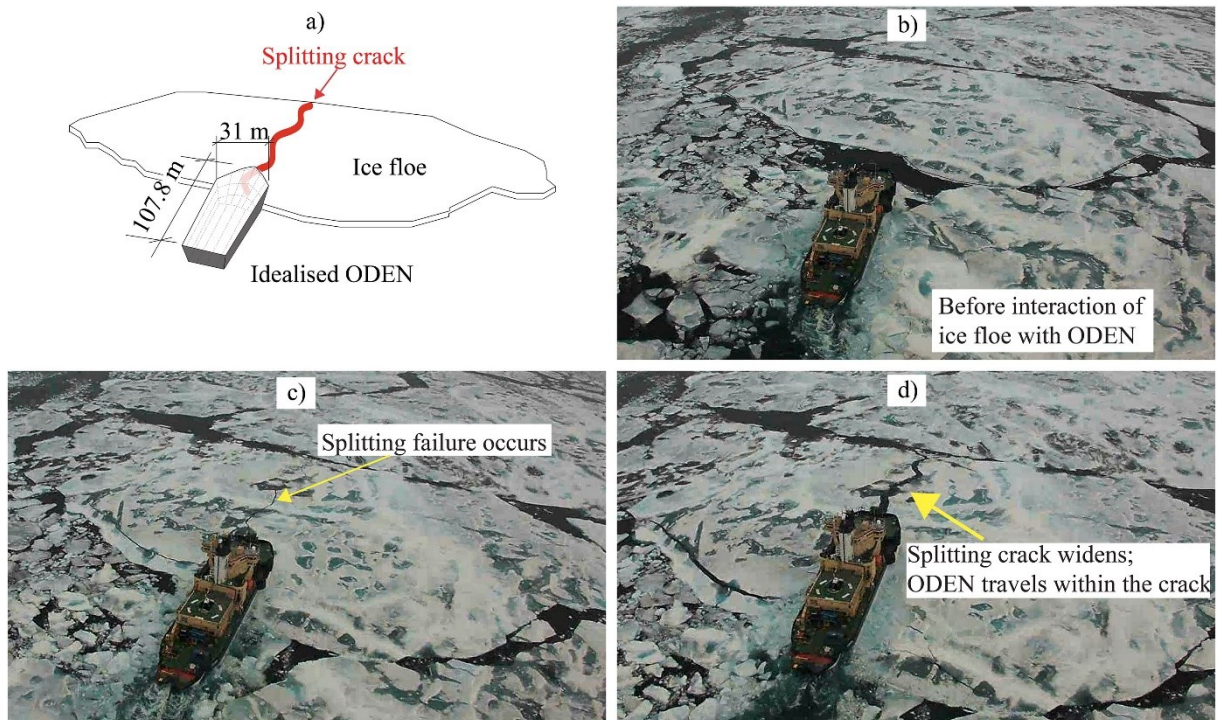
Fig. 2.16 Ship induced splitting in an ice floe (Lu et al., 2015)

2.3 Ice loads formula related to vertical and slope structures

Marine structures can experience various ice loading scenarios in waters with ice. The primary factors, which affect the ice loads, are structural configuration, ice features, ice mechanical properties, ice drifting velocity, etc.

The structural configuration can be divided according to the following features:

- Vertical vs. slope structures

- Rigid vs. flexible structures

- Fixed vs. floating structures

- Narrow vs. wide structures

The following ice features can also be used to analyze ice loads on marine structures:

- Land-fast ice

- Pack ice (drifting ice sheet)

- Ice ridge

- Rubble field

- Iceberg

This research investigates the loads on vertical and slope fixed structures from level ice and ridge so the herein introduced theories are limited to fixed vertical and slope structures from the aspect of structural configuration, and limited to level ice (pack ice) and ice ridge from the aspect of ice feature.

2.3.1 Ice loads on vertical structures

Herein, the vertical structure means the structure surface perpendicularly contacts the pack ice or the consolidated layer of ice ridge. The vertical structure is common in marine structures because it is easy and economical to design and build. The dominating ice failure modes are crushing, buckling and splitting for vertical structures ice interaction. All interaction starts with local ice crushing at the contact area and subsequently with the increase of contact area until the force is strong enough to fail the ice. After the ice failure, the ice load decreases to a much lower level. A continuous crushing process dominates the ice failing process in front of the vertical structures. The structures cut into the ice with in-plane crushing and without any out-of-phase deformation, except buckling for thin ice sheets. The sequence of ice crushing is demonstrated in Fig. 2.17.
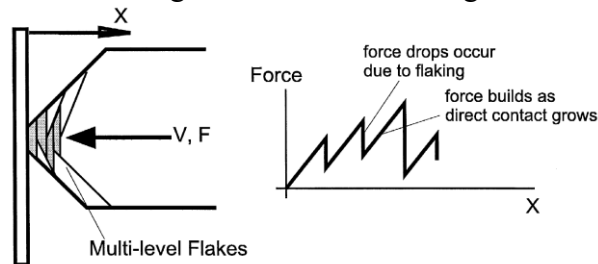
Fig. 2.17 Flaking sequence and load history in ice crushing (Daley et al., 1998)

The flaking continuously occurs during the ice crushing and the local failure of ice is non-simultaneous. This results in uneven and unstable contact between the ice and structure. Consequently, the pressure is not even and stable at the interface, as demonstrated in Fig. 2.18 and 2.19. At a specific time point, the nominal contact area contains high pressure area and low pressure area. Furthermore, the nominal contact area even contains a part of area where no contact exists. Thus, the real contact area would be far less than the nominal contact area and the pressure would be much higher than the nominal pressure at high pressure zones.
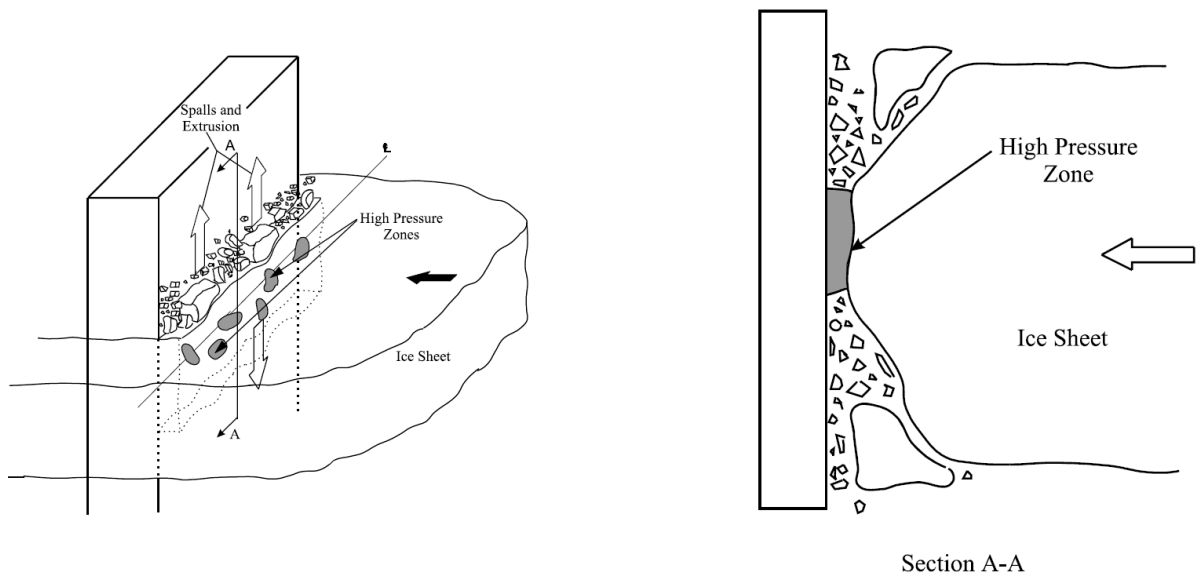
Fig. 2.18 Ice structure contact and pressure distribution (Jordaan, 2001)
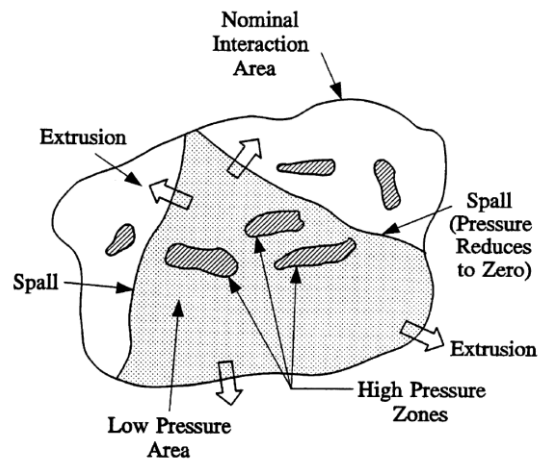
Fig. 2.19 Nominal contact area and contributing components (Jordaan, 2001)

This type of uneven pressure phenomenon was also observed during a full-scale test onboard icebreaker Sampo. A small window with transparent PVDF plate was installed at the water line to observe the contact between ice and hull (Riska et al., 1990). A narrow high pressure band was observed through the window, as shown in Fig. 2.20, which shows the observation through the window at different time. The time proceeds from left to right and down. The dark line is the high pressure area, where the light could not pass through the ice due to high density under high pressure. It is described that the high pressure band is almost horizontal and the incline was induced by the relative location of the camera to the window. It is also shown that the high pressure band moves down along with the moving of broken ice floe, which was pushed down by the icebreaker.
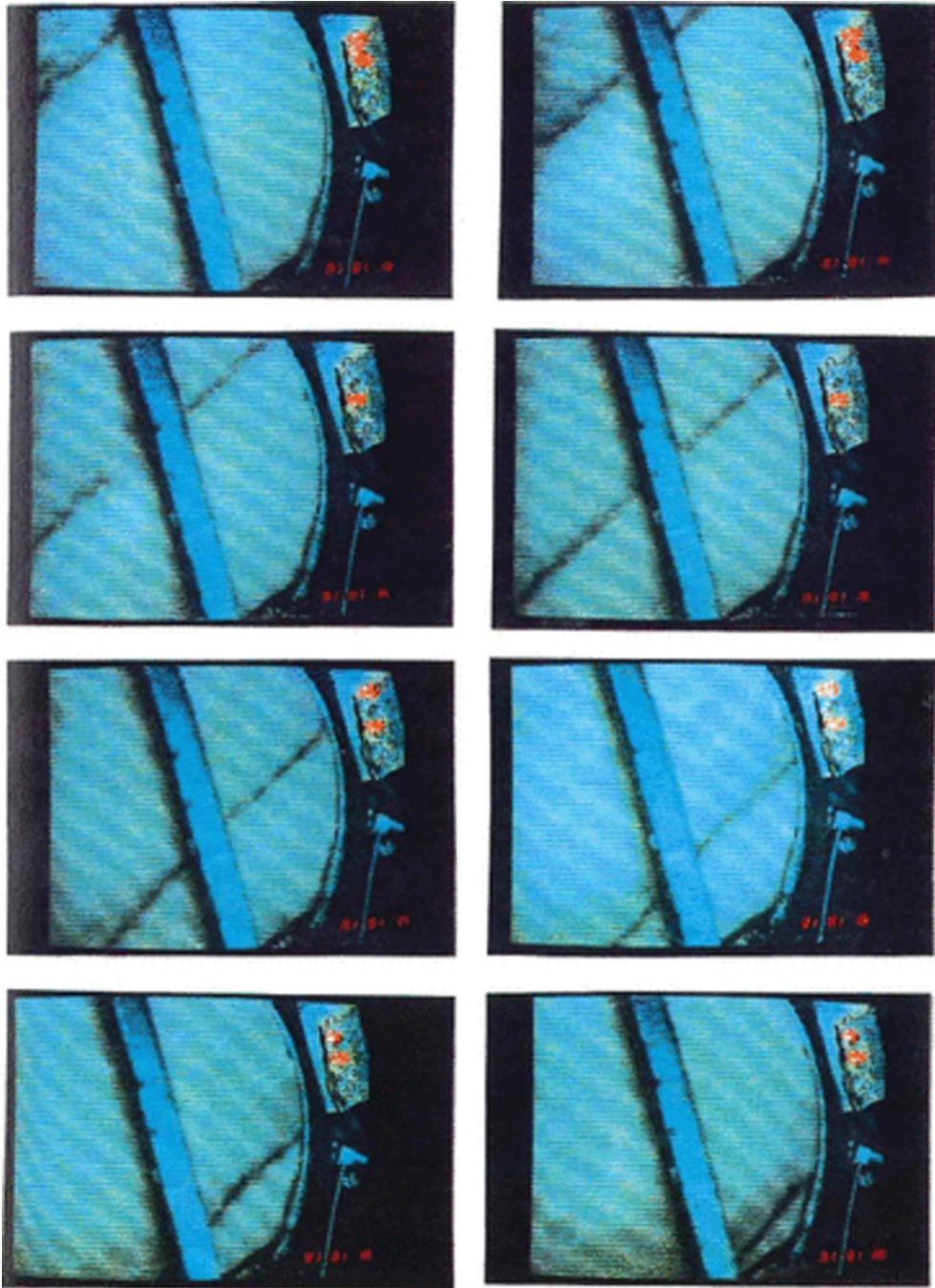
Fig. 2.20 Line like pressure in the full-scale test onboard IB Sampo (Riska et al., 1990)

Muhonen (1991) also observed the uneven pressure phenomenon at the medium scale indentation tests. Figure 2.21 shows that the high pressure area lines link the center area and four corners. Gagnon (1994) and Gagnon & Bugden (2007) explain this phenomenon based on the formation of cracks and consequent spalls. In their theory, the spalls firstly happen in the dark areas as shown in Fig. 2.22 so the high pressure concentrates in the crossing area, which connects the four corners.
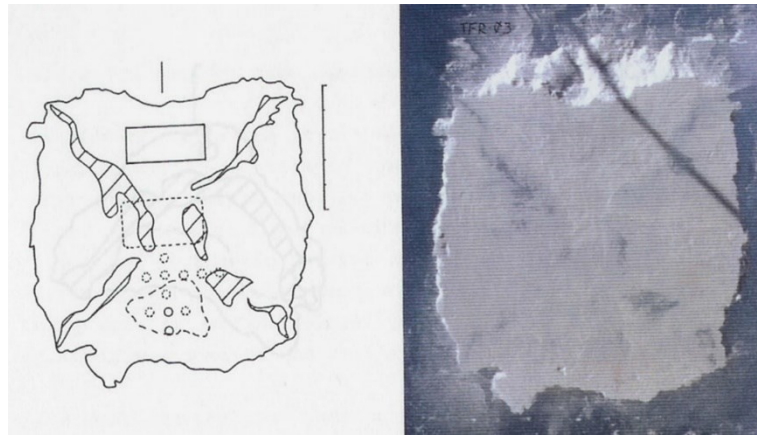
Fig. 2.21 Interpretation of the high pressure area and photograph of the final contact area after the test (Muhonen, 1991)

(a)
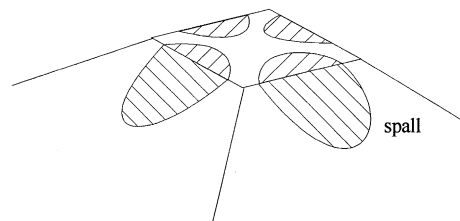
(b)
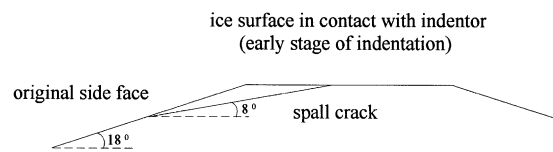
(c)
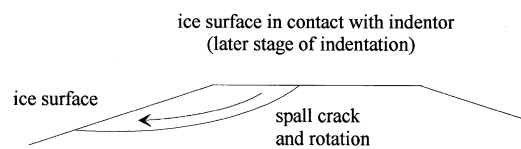
Fig. 2.22 Relationship between spalls and crossing high pressure area (Gagnon, 1998)

Masterson et al. (2007) collected a large number of field measurements and assembled the data to generate new diagram. This diagram presents a revised pressure-area relationship for the nominal areas less than 10 m². According this diagram, the relationship between the area and pressure can be expressed with the following formula

$$p = 7.4A^{-0.7} \qquad (2.13)$$

where A denotes the nominal contact area in m² and p is the contact pressure in MPa. For the nominal contact area larger than 10 m², the pressure is considered constant 1.48 MPa.

The international standard (ISO 19906, Petroleum and natural and industries – Arctic offshore structures) provides another equation to estimate the global ice pressure on the rigid vertical structures

$$p_G = C_R \left(\frac{h}{h^*}\right)^n \left(\frac{w}{h}\right)^m \tag{2.14}$$

where h is the ice thickness, h^* is the reference thickness and equal to 1 m, w is the projected width of structure, $m = -0.16$ is an empirical constant, n is an empirical constant

$$n = -0.50 + h/5 \qquad for\ h < 1.0\ m$$

$$n = -0.30 \qquad\qquad for\ h \geq 1.0\ m$$

and C_R is an ice strength coefficient ($C_R = 2.8$ MPa for the Arctic area and $C_R = 1.8$ MPa for Baltic sea). Thus, the global force on the rigid vertical structure can be calculated

$$F = whp_G \tag{2.15}$$

The equation considers the influence of the nominal area, which is a product of ice thickness h and structure width w.

If the ice sheet is thin enough, usually less than 0.4 m, it could fail in buckling. In this case, the problem is analyzed by using the elastic model. The ice sheet is assumed to be a truncated wedge-shaped elastic plate floating on an elastic foundation (balance of weight and buoyancy). The force P is loaded on the edge of ice sheet with a width D, as shown in Fig. 2.23.
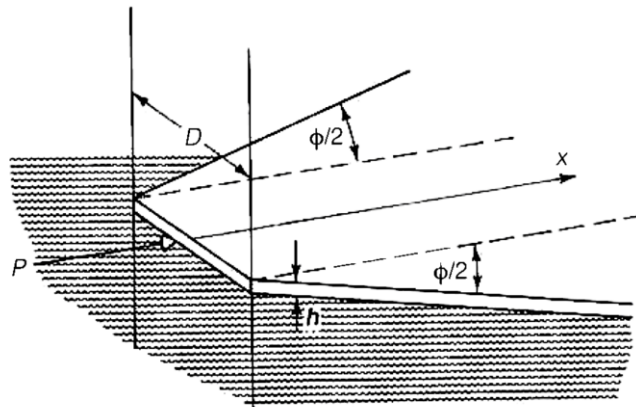
Fig. 2.23 Elastic model for solving buckling problem (Sanderson, 1988)

The wedge angle ϕ can vary from $0°$ to $180°$. According to the research of Sanderson (1988), the angle is usually $45°$ before buckling when the radial cracks are generated by the interaction with structures. Figure 2.24 shows the formation of cracking in front of a rectangular pier and a circular pier.
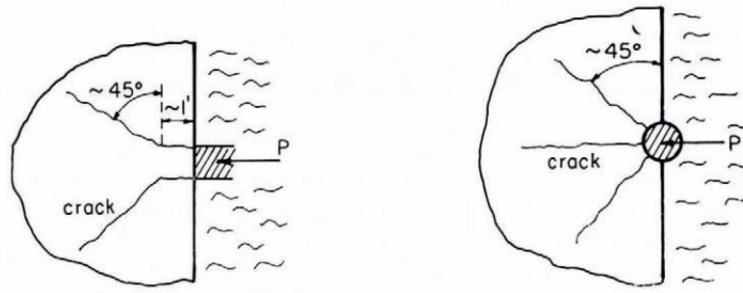
Fig. 2.24 Form of observed cracking due to buckling (Kerr, 1978)

Based on the boundary condition at the interacting edge, Kerr (1978) proposed an equation to calculate the buckling force

$$P_b = 5.3 B_f \kappa \left(\kappa D + 2 tan \frac{\phi}{2} \right) \tag{2.16}$$

where B_f denotes the flexural rigidity of the ice sheet

$$B_f = \frac{Eh^3}{12(1-v^2)} \tag{2.17}$$

$$\kappa = \left(\frac{g\rho_w}{4B_f} \right)^{1/4} \tag{2.18}$$

and ρ_w is the water density, g is the gravity acceleration, h is the ice thickness, D is the structure width, v is the Poisson's ratio of ice and E is the Young's modulus of ice.

Sodhi and Hamza (1977) provided another formula to calculate the buckling force

$$F_b = kl^3 \left[\frac{D}{l} + 3.32 \left(1 + \frac{D}{4l} \right) \right] \tag{2.19}$$

where k is the foundation modulus, which is equal to the weight density of water, l is the characteristic length

$$l = \sqrt[4]{Eh^3/12k(1-v^2)} \tag{2.20}$$

h is the ice thickness, D is the structure width, v is the Poisson's ratio of ice and E is the Young's modulus of ice. In this model, the ice sheet is assumed to be semi-infinite and with fixed boundary condition at infinite edge and frictionless boundary conditions at the loaded edge.

2.3.2 Ice loads on slope structures

The tensile strength of ice is weaker than the compressive stress at every orientation, as shown in Fig. 2.25. The solid dots denote compressive strength and the open circles denote the tensile strength in Fig. 2.25. Thus, the ice loads can be reduced if it fails by tension. When the ice sheet is bent, one surface suffers compression and the opposite surface suffers tension. The ice usually fails at the tense surface due to weaker tensile strength. This is the philosophy of reducing the ice load by using slope contact surface between the ice and structure.
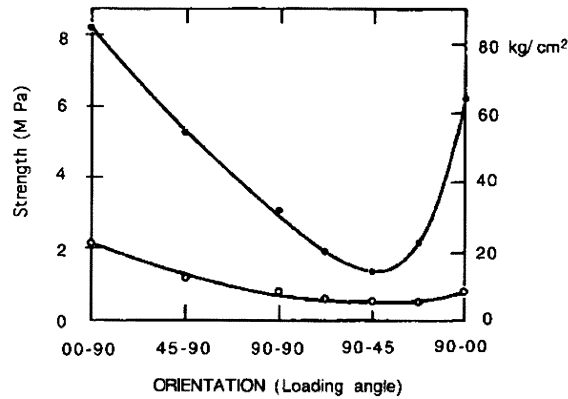
Fig. 2.25 Average measured tensile strength and compressive strength vs. sample orientation (Peyton, 1966)

The out-of-plane force component is needed to moment to bend the ice, which can be generated by slope surface of the structure. When the ice sheet contacts the slope structure, the force on the ice can be simply decomposed
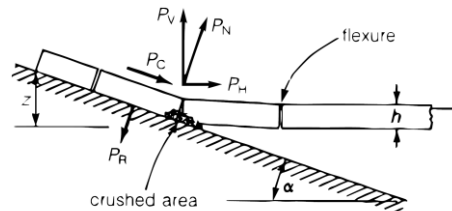
Fig. 2.26 Force on ice while contacting the slope structures (Sanderson, 1988)

Here, the flexural strength is used to study the bending instead of the tensile strength. It should note that the flexural strength is not a basic material property. It is just an index value to describe the ice strength. Because bending can obviously reduce the ice loads on structures, it plays an important role in the ice-structure interaction process. Many marine structures are designed with slop surface to reduce the ice loads.

If the ice sheet is considered as a cantilever beam, the flexural strength can be described as

$$\sigma_f = \frac{6P_V l}{W h^2} \tag{2.21}$$

where P_V is the load perpendicular to the ice plane, l is the distance between the load and supporting point, W is the width of the beam and h is the ice thickness.

According to the decomposition in the Fig. 2.26, the relationship between the vertical and horizontal force can be described as

$$P_H = \left(\frac{sin\alpha + \mu cos\alpha}{cos\alpha - \mu sin\alpha}\right) P_V \tag{2.22}$$

where μ is the coefficient of friction between the ice and structure.

The ice floats on the water surface so it can be assumed that the foundation is elastic and directly proportional to the deflection of the beam at every point, which acts like stiffness. The foundation modulus

$$k = \rho_w g \tag{2.23}$$

where ρ_w is the water density and g is the gravity acceleration.

According to the beam theory, the differential equation of the beam deflection can be described

$$\frac{d^4y}{dx^4} + \lambda^4 y = 0 \tag{2.24}$$

where $\lambda = \sqrt[4]{k/4EI}$, E is the Young's modulus of the beam, I is the section modulus of the beam. Hetényi (1946) proposed the general solution of the beam deflection by assuming the beam is semi-infinite and the load is perpendicularly loaded on the end

$$y = e^{\lambda x}(C_2 sin\lambda x + C_1 cos\lambda x) + e^{-\lambda x}(C_4 sin\lambda x + C_3 cos\lambda x) \tag{2.25}$$

The bending process contains four stages: 1) Local crush at the contact edge; 2) Possible fail due to shearing before bending; 3) Failure due to bending induced tension; 4) Rubble formation. This process can be treated as a hierarchy of failures, each can be superseded by lower lever failure (Daley et al., 1998). Figure 2.27 presents the concept of nested hierarchy of discrete events.
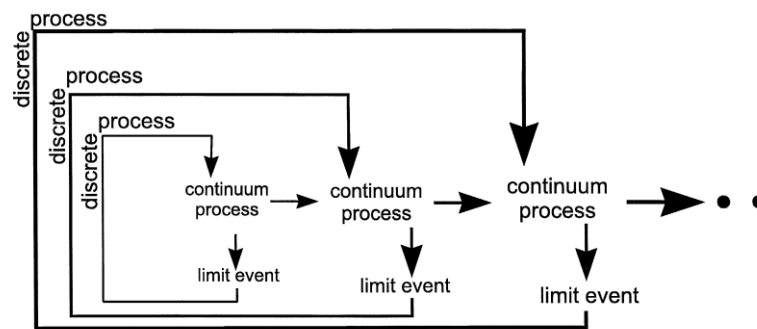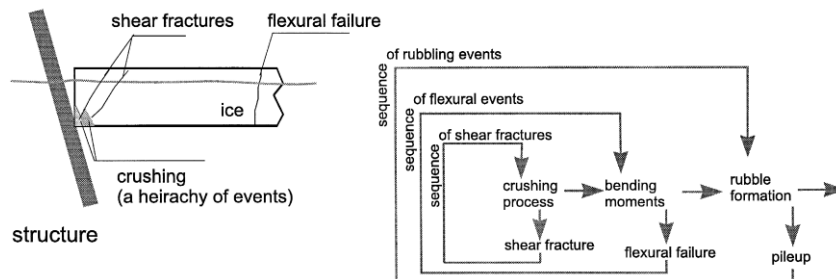
Fig. 2.27 Nested hierarchy of failure events (Daley et al., 1998)

The bending failure generates rubbles in front the structures, which can influence the accumulation of the rubbles. If the structure is narrow, broken ice blocks can be cleared to the both sides of the structure. On the other hand, the ice blocks are seldom cleared to the sides of wide structures. Thus, it is a two-dimensional problem to analyze the ice failing in front of a wide slope structure. The aspect ratio h/D is used to distinguish the wide and narrow structures, where h is the ice thickness and D is the width of the structure.

Ralston (1977) presented a model to calculate the ice loads induced by level ice on a conical structure. The situation of the model is shown in Fig. 2.28. The model is based on a plastic analysis of pure bending failure of an ice sheet.
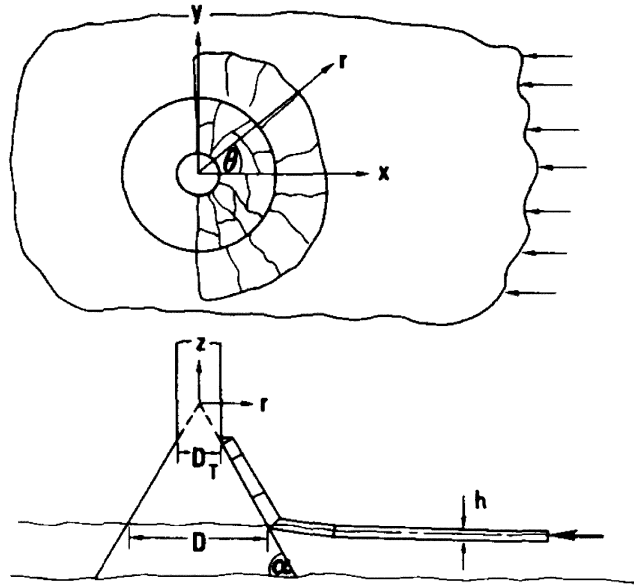
Fig. 2.28 Ice sheet failure against a conical structure (Ralston, 1977)

According to this model, the vertical ice load F_V and horizontal ice load F_H are given respectively

$$F_H = A_4\left[A_1\sigma_f h^2 + A_2\rho_w ghD^2 + A_3\rho_w gh(D^2 - D_T^2)\right] \qquad (2.26)$$

$$F_V = B_1 F_H + B_2\rho_w gh(D^2 - D_T^2) \qquad (2.27)$$

where σ_f is the flexural strength, h is the ice thickness, ρ_w is the water density, g is the gravity acceleration, D is the cone diameter at the waterline, D_T is the cone diameter at the top, and A_i, B_i are coefficients as functions of ice structure friction coefficient μ, the inclined angle α, h, ρ_w, g, D and σ_f. The first two terms of F_H are derived from the breaking of the advancing ice sheet so the coefficients A_i $(i = 1, 2)$ are related to the parameter $\rho_w gD^2/(\sigma_f h)$. The third term of F_H is from the broken ice blocks riding over the slope surface. A_i $(i = 3, 4)$ are function of the slope angle and ice structure friction coefficient. The first term of F_V is the horizontal component of force for breaking the ice and the second term is relevant to the force generated by the riding ice blocks. By using Fig. 2.29, the coefficients A_i $(i = 1\sim 4)$ and B_i $(i = 1, 2)$ can be determined based on the known parameters.

2.3.3 Rubble and ridge loads on structures

The ice ridge mainly contains three parts: ridge sail, consolidated layer and ridge keel. The ridge sail is normally small compared to the consolidated layer and ridge keel. As a result, this part can be ignored for estimating the ridge loads on structures. The ridge loads F_k can be predicted (Croasdale, 1980; Kärna and Nykänen, 2004)

$$F_k = F_c + F_r \qquad (2.28)$$

where F_c is the loads induced by the consolidated layer and F_r is the loads induced by the rubbles in keel.

The method for estimating the level ice loads can be used to estimate the loads form the consolidated layer (Kärna and Nykänen, 2004). According to the proposal of Dolgopolov et al. (1975), the loads from consolidated layer can be estimated
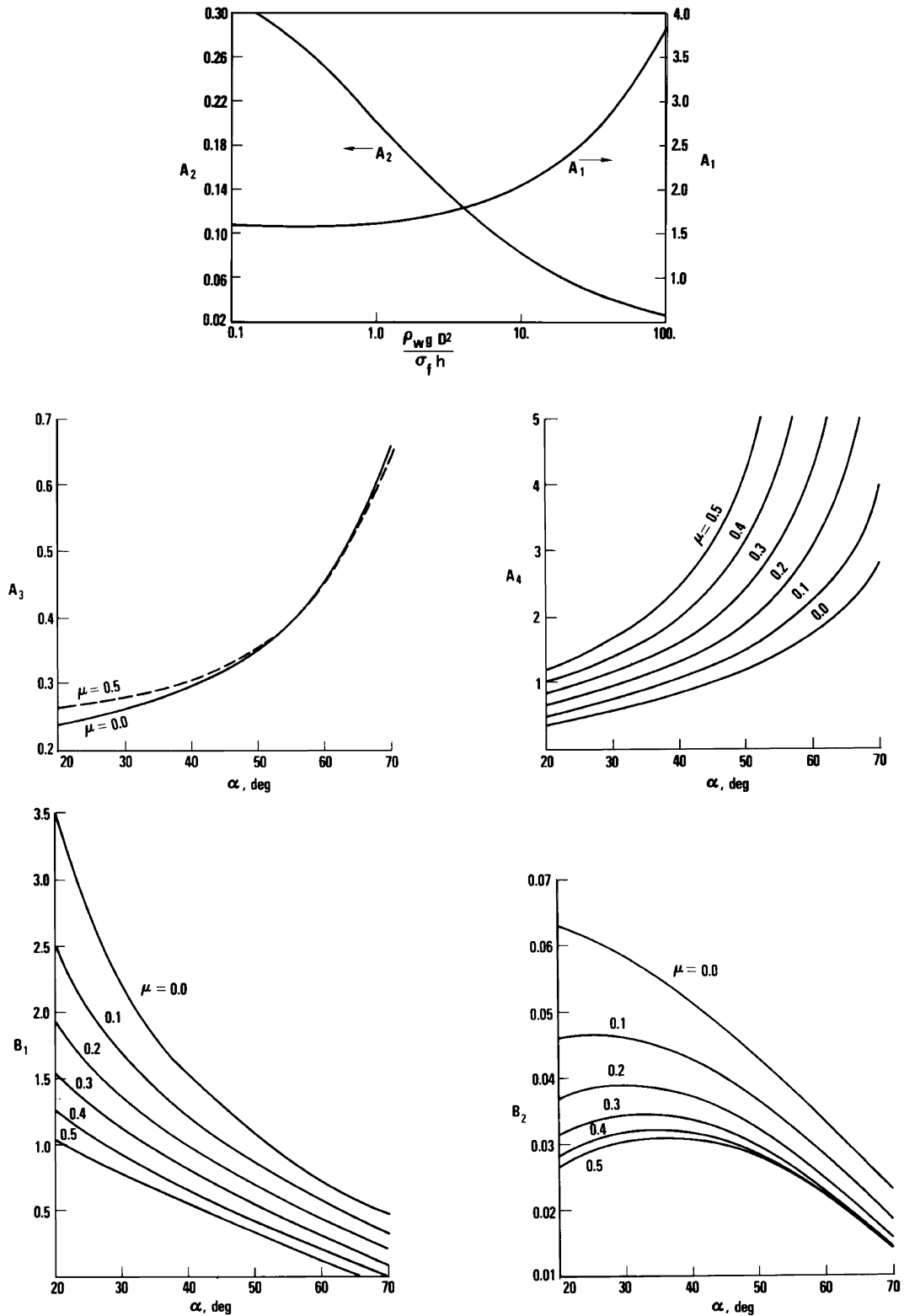
Fig. 2.29 Dimensionless coefficients for plastic analysis (Ralston, 1977)

$$F_r = \mu_\phi \hat{h}_r w \left(\frac{\mu_\phi \hat{h}_r \gamma_e}{2} + 2c \right) j \qquad (2.29)$$

where $\mu_\phi = tg(45° + \phi/2)$ is the passive pressure coefficient, ϕ is the angle of internal friction, $\hat{h}_r$ is the rubble thickness measured from bottom of consolidated layer, w is the

width of structure, $\gamma_e = (1 - \eta)(\rho_w - \rho_i)g$ is the effective buoyancy, in units consistent with c, η is the macro porosity, ρ_w is the water density, ρ_i is the ice density, c is the apparent keel cohesion, $j = 1 + 2l_s/(3w)$ is an aspect ratio factor and l_s is the length of the sail. This formula is derived from the soil mechanics for estimating the passive failure of granular material. This method includes the influence of sail by considering the length sail. Kärna and Nykänen (2004) used the $\hat{h}_r$ instead of l_s to modify Dolgopolov's formula and consequently neglected the influence of sail

$$F_r = \mu_\phi \hat{h}_r w \left(\frac{\mu_\phi \hat{h}_r \gamma_e}{2} + 2c\right)\left(1 + \frac{\hat{h}_r}{6w}\right) \tag{2.30}$$

The above equation, which applies the Mohr-Coulomb criterion, shows that there are three parameters (ϕ, η and c) other than the geometric dimensions, which can affect the rubble loads. These three parameters of first-year ridge are different from those of multi-year ridge. Thus, the ridge loads would be different. Herein, only the first-year ridge is investigated in this research. Even in the first-year ice ridge, these three parameters vary in temporal and special dimensions. Liferov and Bonnemaire (2005) recommend a range between 25 and 45 degrees for the friction angle. The rubble cohesion varies from 0 to 100kPa (Ettema and Urroz-Aguirre, 1989) and it is a result of freeze bonds in between ice rubbles. Thus, the temperature of rubbles and sea water can influence the cohesion because the temperature can influence the strength of freeze bonds. The measured values of macro porosity are usually between 30% and 40% (Leppäranta et al., 1995), (Kankaanpää, 1998), (Surkov, 2001), (Timco et al., 2000), (Høyland, 2002). Leppäranta et al. (1995) and Kankaanpää (1998) report that the highest porosity is in the lower part (50%) of the keel with a mid-keel minimum porosity in the Baltic. Nevertheless, Høyland (2007) reports a different porosity distribution in the ridge of northwest Barents Sea: The porosity increases downwards throughout the rubble, 20% beneath the consolidated layer and 50% close to the keel bottom.

2.4 Scale model testing

The scale model testing is an important method to study the ice loads on structures and the structural response, e.g. displacement, vibration and motion. In order to obtain reliable data, which can reflect the physical mechanism of prototype, the scaling laws shall be obeyed carefully. The scaling laws are relationship between the scaled mode and prototype in different variables, which can be used to predict the environmental/external loads and the behavior of the structures.

Three types of similarity are commonly used in the scale model testing of ice loads on structures: geometric scale λ, kinematic scale λ_k and dynamic (kinetic) scale λ_d.

$$\lambda = \frac{L_p}{L_m} \tag{2.31}$$

$$\lambda_k = \frac{v_p}{v_m} \tag{2.32}$$

$$\lambda_d = \frac{F_p}{F_m} \tag{2.33}$$

where the subscript p and m denotes the prototype and model, respectively. The kinematic scale and dynamic scale can be represented by using the function of geometric scale

$$\lambda_k = \lambda^\beta \tag{2.34}$$

$$\lambda_d = \lambda^\alpha \tag{2.35}$$

The superscript β are different in different parameters and α is in the same situation. Some examples are presented in Table 2.1.

Table 2.1 Different force contributions and their scales

Process	Force
Inertia	$F_{in} = ma = m\dfrac{v^2}{L} = \rho L^3 \dfrac{v^2}{L} = \rho L^2 v^2$
Gravity	$F_g = mg = \rho g L^3$
Viscous fluid (fluid friction)	$F_{viscous} = \tau L^2 = \mu v L$
Linear elastic material	$F_{elastic} = \sigma L^2 = E\varepsilon L^2 \sim E L^2$
Strength of material	$F_{SOM} = \sigma L^2 = \sigma_f L^2$

Three dimensionless ratios of forces are commonly used in the scale model testing: 1) Froude number Fr; 2) Reynold's number Re; 3) Cauchy number Ca.

$$Fr = \frac{F_{in}}{F_g} = \frac{v^2}{gL} \tag{2.36}$$

$$Re = \frac{F_{in}}{F_{viscous}} = \frac{vL}{v} \tag{2.37}$$

$$Ca = \frac{F_{in}}{F_{elastic}} = \frac{\rho v^2}{E} \tag{2.38}$$

These three dimensionless numbers show different relationships between the inertia force and another three kinds of force. Thus, it is impossible to maintain all the three numbers same in the model-scale and full-scale. Langhaar (1951) analyzed the derivation of the Froude number and Reynold's number by using the force ratio and dimensional analysis. Barker et al. (2005) summarized the modelling scales of various physical parameters in the model tests, which are shown in Table 2.2.

Table 2.2 Modelling scales used in model tests

Property	Scale by	Property	Scale by
Length	λ	Ice strength	λ
Time	$\lambda^{1/2}$	Ice thickness	λ
Speed	$\lambda^{1/2}$	Elastic modulus	λ
Acceleration	1	Ice fracture toughness	$\lambda^{3/2}$
Mass	λ^3	Ice-structure friction	1
Force	λ^3	Ice-ice friction	1
Density	1		
In-line transverse			
Stiffness	λ^2	Damping	1
Frequency	$\lambda^{-1/2}$	Mass	λ^3

For the research of ice loads, the SOM number is often used

$$SOM = \frac{F_{in}}{F_{SOM}} = \frac{\rho v^2}{\sigma_f} \tag{2.39}$$

The SOM number is similar to the Cauchy number but uses the flexural strength instead of elastic modulus. The flexural strength is often used to index the strength of ice practically so the SOM number is often used as well. In the scale model test of ice, the SOM number should be maintained between the model-scale and full-scale. Thus, the model ice should be weakened by a scale of λ according to the equation 2.39.

The geometrical scale λ should be less than 200 in order to minimize the scale effect (Huse and Matsumoto, 1989; Larsen and Huse, 1993; Fernandes and Kroff, 2000, Park et al., 1999). When the scale is too large, the effect of water surface tension will be large too. The Weber number W is used to express the ratio of inertia force and surface tension

$$W = \frac{F_{in}}{F_{tension}} = \frac{\rho v^2 L}{\sigma^*} \tag{2.40}$$

where σ^* is the surface tension. According to the equation of Weber number, the Weber number of models will decrease by λ^2 times if the geometric scale is λ. This means the influence of surface tension increases by λ^2 times so the effect of surface tension cannot be ignored.

Another reason is that the ice thickness should be large enough to contain sufficient ice grains. Table 2.2 shows that the scale of ice thickness is λ so the thickness of model ice is in the order of *cm*. The grain size of model ice should be smaller than the natural sea ice, which contains the ice grains with size in the order of *cm* too. Whereas, the thickness of model ice would be in the order of *mm* if the scale is too large. Consequently, it is too hard to contain enough number of ice grains within the ice thickness.

In practice, researchers pay most attention to achieve the proper scale of the flexural strength because it is considered the critical parameter (Li et al., 2002; Nortala-Hoikkanen, 1990). The cantilever beam is often used to test the flexural strength of model ice. It is relatively easy to achieve proper ice grain size by using some seeding technique, such as spraying fog with small water particles over undercooled water.

According to the materials of model ice, it can be divided into two groups: 1) Doped ice, which is made from water with additives, such as salt, carbamide (urea), glycol, ethanol and sugar (Niskanen, 2005); 2) Sythetic ice, which is made from non-water material, usually paraffin. The doped ice is used by most ice tanks because the ice rubble can freeze to each other. This is advantage for modelling ice ridges and relevant interaction between ice ridge and structures.

3   Experiment setup

The model tests were conducted in the Aalto Ice Tank of Aalto University. In this chapter, the information is described about the testing facilities, model ice, model and prototype structure, model-scale, and testing procedure, etc.

3.1   Testing facilities

The Aalto Ice Tank mainly contains four parts: 1) the ice basin; 2) storage and model fitting room; 3) cooling machinery room; 4) heat exchangers.

The dimension of ice basin is 40 m long, 40 m wide and 2.8 m deep. A series of wave generator are installed on one side of the basin, which is able to generate regular and irregular waves. On the opposite side, a sloping beach is built to consume the waves in order to prevent the wave reflection. A towing carriage is installed above the ice basin. The towing carriage is able to longitudinally and transversally run the model while performing the tests. Figure 3.1 shows a photo of the Aalto Ice Tank and its general arrangement is presented in Fig. 3.2.

Fig. 3.1 Photo of the Aalto Ice Tank

SECTION A

SECTION B

1. X-carriage
2. Y-carriage
3. Cooling evaporators
4. Air tubes
5. Sloping beach
6. Ice ditch
7. Overhead crane beam
8. Lifting arm
9. Heat exchangers
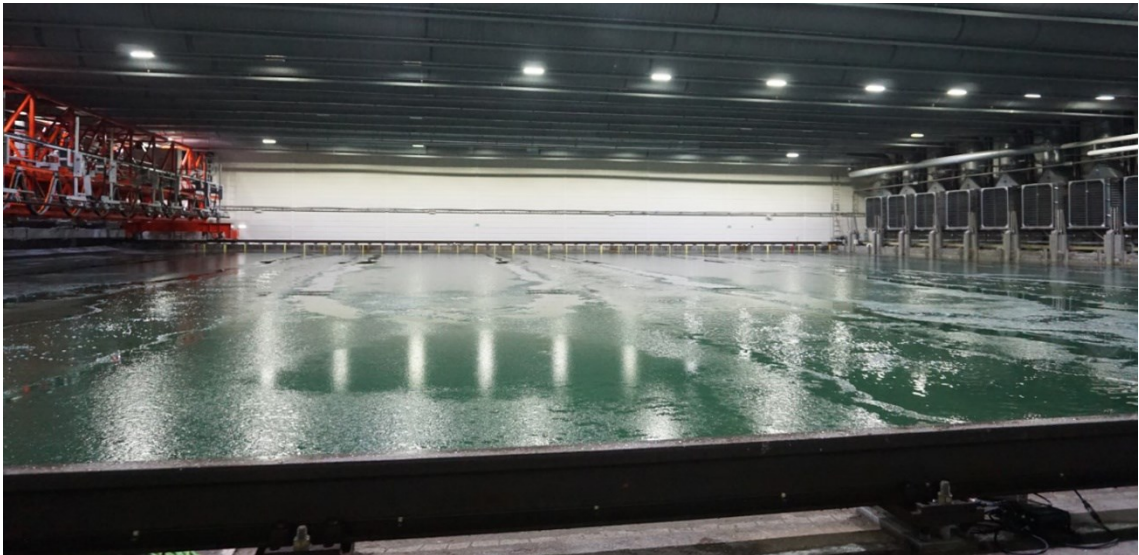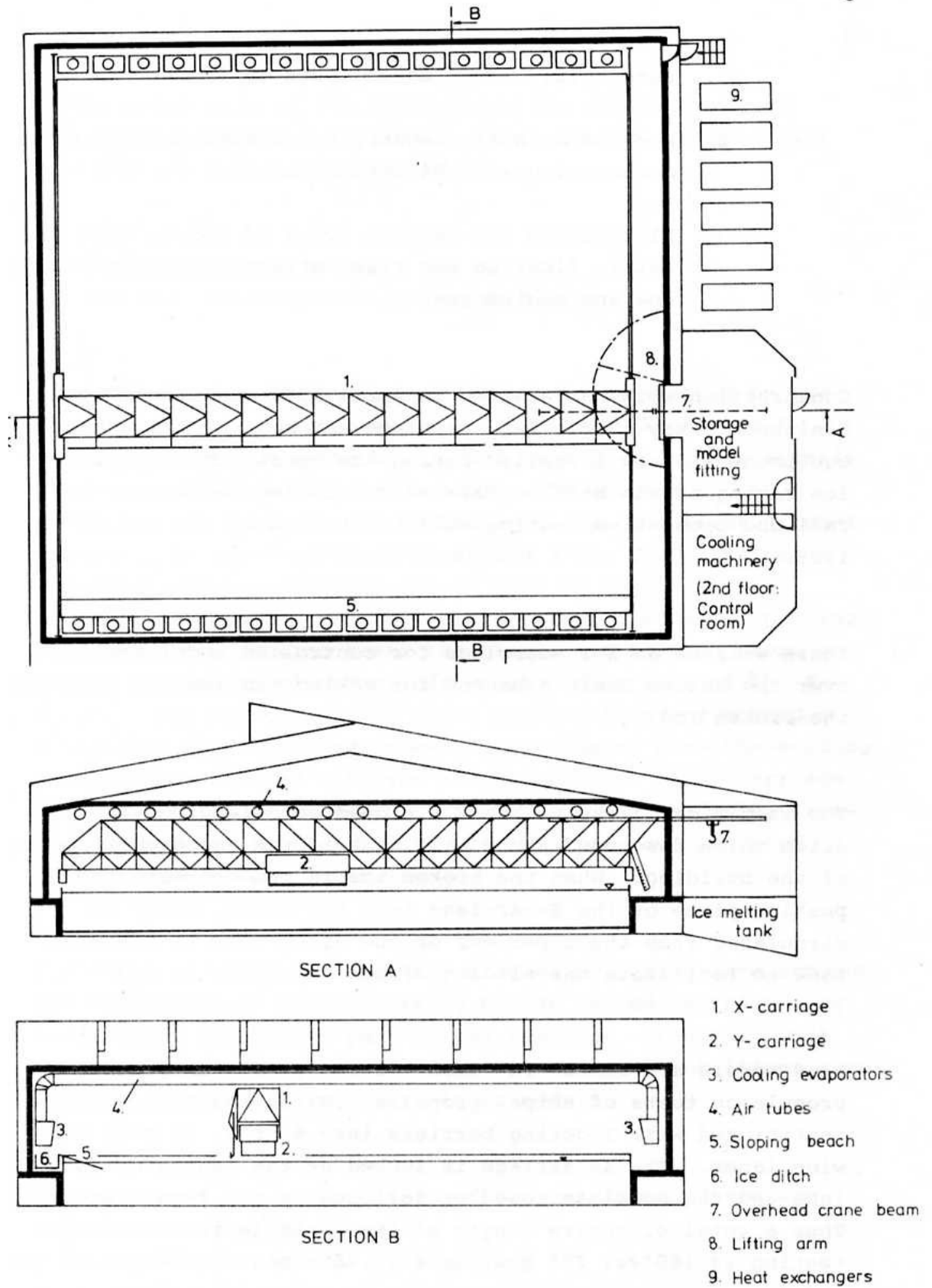
Fig. 3.2 General arrangement of the Aalto Ice Tank

The model can be built/fit before the test and stored after the test in the storage and model fitting room. The cooling machinery and heat exchangers are used to change the air temperature of the Ice tank in order to generate and temper the model ice in the ice basin.

A multicomponent sensor was installed on the model to collect the data of ice loads. It was connecting by using flange with centering and pin for positioning. This sensor contains six components for detecting and collecting the ice loads in six degrees: force in X, Y, Z directions and moments in X, Y, Z directions, as shown in Fig. 3.3. Fig. 3.3 shows that the origin of the sensor coordinates is in the geometric center (half the height of the sensor). The force and moment sensitivities have a maximum deviation of 5%.
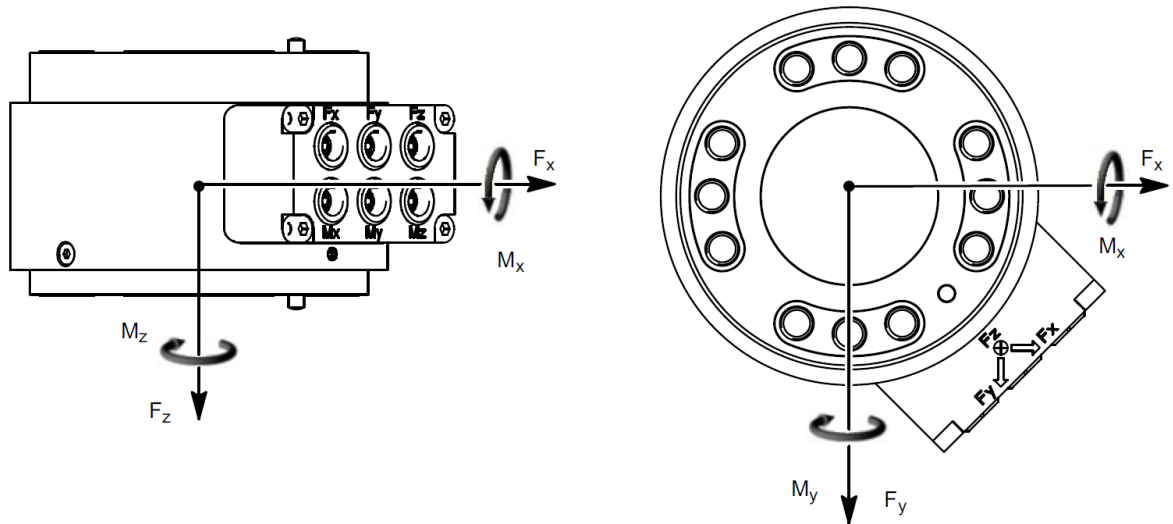
Fig. 3.3 Sensor scheme and direction of tested loads (Hottinger Baldwin Messtechnik GmbH)

The origin of the sensor coordinates was at the vertical central line of the model. The vertical distance was 0.094 m between the origin of the sensor coordinates and the top of the conical part of the model. The exact position can be found in Appendix, Test Structure Support.

Six cameras were attached to the model to watch the behaviour of structure and ice, especially to watch the failure modes of ice and the rubble accumulation. 2 cameras were above the water surface and 4 cameras were installed underwater. An underwater frame was designed for carrying the underwater cameras, which is shown in Fig. 3.4.

Fig. 3.4 Underwater frame

3.2 Model ice generation

GE-ice was used during the basin tests. GE-ice is a kind of granular model ice doped with ethanol. This type of ice is brittle and has similar bending failure characteristics to the real ice. It does not have any significant remnant force in the cantilever beam tests. A continuous spraying method was used to produce the ice with proper granular structure. The ice structure is not homogeneous so the ice is stronger in the top layer, as shown in Fig. 3.5.

Fig. 3.5 Layering of the ice, strong top layer, weak bottom layer

The water droplets of 0.3% ethanol solution were sprayed on the water surface with properly low air temperature (around -10 ºC). A layer of slush ice was formed when the droplets hit the water surface. The spraying was continuously repeated until the target ice thickness is obtained in the spraying method. The spraying nozzles were carried by the carriage. The spraying period was controlled by the consolidating period. The strength of ice can be

tempered by changing the air temperature in order to obtain the target strength after the consolidating period.

Palosuo (1975) reported that level ice thickness in the Baltic range from 0.15 to 1.2 m so a full-scale initial level ice thickness of 0.75 m was selected for this experiment. The geometrical scale factor λ is 15 so the model ice thickness is 0.05 m.

After the level ice was totally formed, a part of it (40 m X 20 m) was cut into pieces with random size. The maximum size of the ice rubble was approximately 20 ~ 25 cm. The distribution of rubble size was controlled by a chess board. After the producing of ice rubble, a plate was drawn by the carriage to push the rubbles together to generate a proper cross section, which is similar to real ice ridge. The remaining two pieces of level ice floes were pulled to the ice ridge. As a result, the gaps between the ridge and ice floes were small enough to make the level ice floes frozen together with the consolidated layer after the freezing procedure of generating consolidated layer. The above procedures are shown in Fig. 3.6. The transverse profile of keel was measured by using distributed punch holes. Some profiles are shown in Fig. 3.7 as example. The maximum depth of keel was approximate 0.4 m. The width of ridge was generally 4 m and started from the side close to the structure. It is clearly shown that the profile of keel was roughly in the shape of trapezoid, which is similar to the geometry of natural ridge keel.

The consolidated layer was generated by lowering the air temperature at -12 °C, the procedure is similar to the natural procedure of forming consolidated layer. After the consolidating step, the temperature was raised up to 4 °C to temper the strength of ice until the expected value was achieved. The history of air temperature was shown in Fig. 3.8. The temperature was measured by using four thermistors. Two strings of themistors were installed in the level ice and another two strings were installed in the ridge.
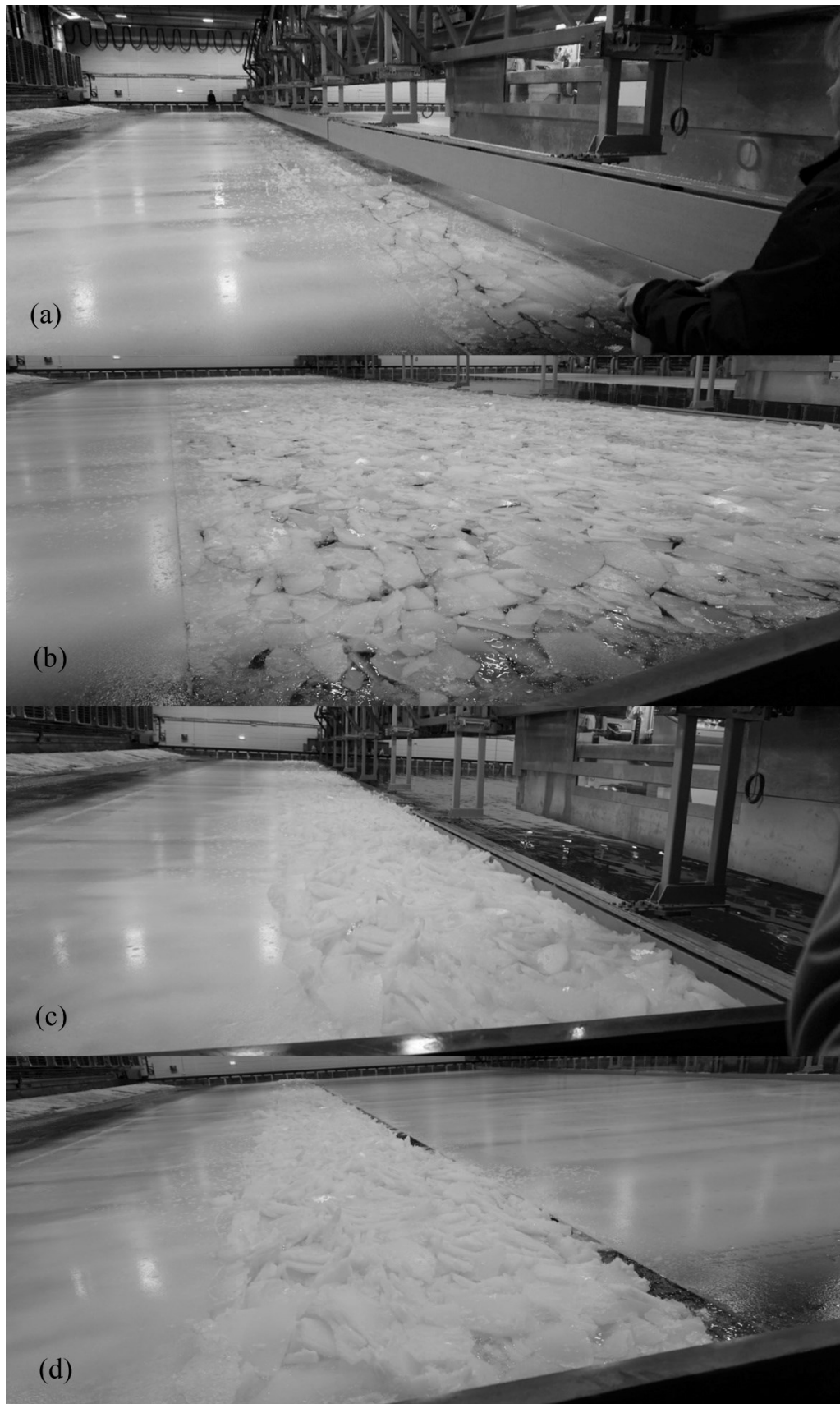
Fig. 3.6 Ridge generating procedures: (a) start cutting, (b) cutting finished, (c) pushing ice rubbles, (d) consolidating.
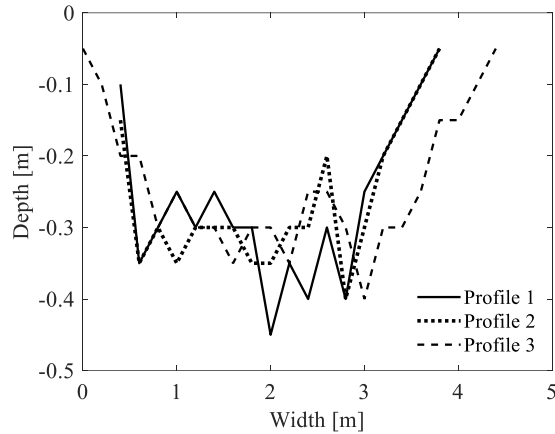
Fig. 3.7 Examples of measured keel profile
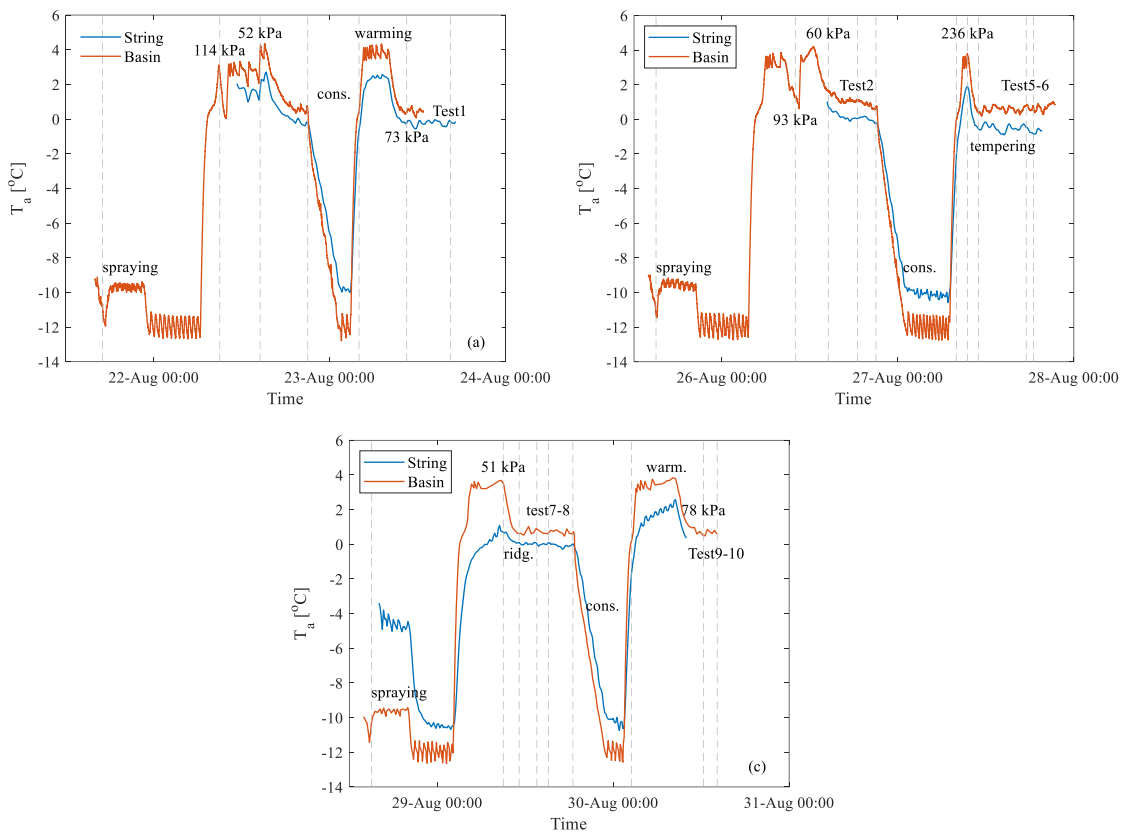
Fig. 3.8 Air temperature timeline for ice floe 1 (a), 2 (b) and 3(c)

3.3 Structure description

The prototype is the lighthouse Norströmsgrund, which locates in the north part of the Baltic Sea. The photo of the lighthouse is shown in Fig. 3.9 (a). The location is shown as a red dot with ice coverage and ice thickness in Fig. 3.9 (b). As shown in Fig. 3.9 (a), the lighthouse is a cylindrical type structure with a vertical wall contacting the level ice and ice ridge.
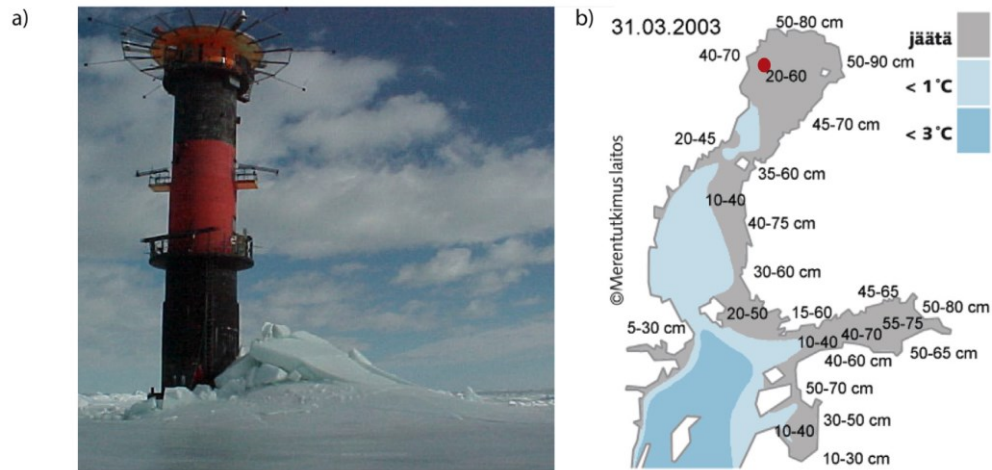
Fig. 3.9 Photo of the lighthouse Norströmsgrund (Ervik et al., 2019)

The diameter of the lighthouse is 7.5 m and the geometrical scale factor is λ = 15 so the diameter of the model is 0.5 m. In order to compare the ice loads on cylindrical structure and conical structure, a conical part was added to the model, with a slope angle of 75 degree. The main dimension of the model is shown in Table 3.1. The photo of the model is shown in Fig. 3.10.

Fig. 3.10 Structure of model, including both cylindrical part and conical part

Table 3.1 Main structure parameters

Structure parameter	Unit	Model-scale	Full-scale
Cylinder diameter	[m]	0.5	7.5
Cylinder length	[m]	1.0	15
Cone Length	[m]	0.4	6
Cone angle	[°]	75	75

3.4 Measurement of flexural strength of level ice and shear strength of ridge keel

The flexural strength of level ice and shear strength of ridge rubble are two most influential properties to the ice loads so the two types of strength should be measured before the ice loads tests. The strength measurements include floating cantilever beam tests for the level ice and punch tests for the ice ridge. The locations of the strength tests are shown in Fig. 3.11.
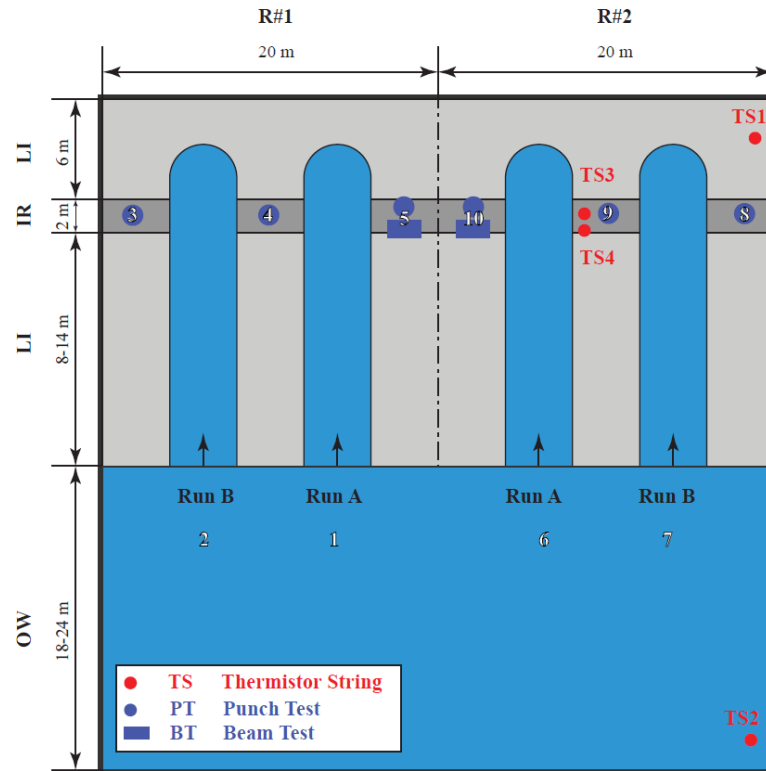
Fig. 3.11 Locations of ice loads test route, thermistor string, punch test and cantilever beam test

According to ITTC recommendation (2014), an in-situ cantilever beam should be used to determine the flexural strength of an ice sheet. The floating cantilever beam should be cut in-situ and have length of l and width of b. The length l should be five to seven times of ice thickness h and the width b should be two to three times of ice thickness h. The beam dimension is shown in Fig. 3.12. The ratio of l/b should be large enough in order to ensure the tested specimen behaves like a beam but not a plate. ITTC also recommends the limiting beam dimensions as shown in Fig. 3.13.
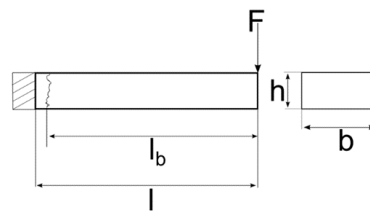
Fig. 3.12 Cantilever beam dimensions
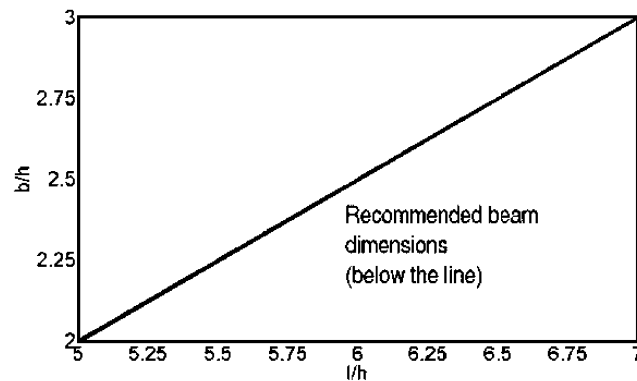
Fig. 3.13 Limiting beam dimension

The tip of beam should be loaded at a constant and proper speed until the beam fails. The speed should be slow enough to avoid significant hydrodynamic effects or specimen damage because of the local impact of the test plunger. The loading speed should fulfil the requirement on the brittle failure process. Timco (1981) proposed that the time between the start of loading and the ice failure should be about 1 s – 2 s. He also proposes a formula, following Bernoulli-beam theory, to calculate the flexural strength

$$\sigma_f = \frac{M}{W} = \frac{6Fl_b}{bh^2} \tag{3.1}$$

Where σ_f denotes the flexural strength, F denotes the load force, l_b denotes the distance from the crack location to the loading point.

Three in-situ cantilever beams were used to measure the flexural strength of level ice at one location. The average value flexural strength of these three beams is used as the measured flexural strength at the specific location. A mold was used at the exact transverse location to ascertain the proper dimensions of cantilever beam, which are 0.25 m long and 0.08 m wide, respectively. Subsequently, a vertical force was loaded at the center part of the beam tip with a constant and proper speed according to the recommendation of ITTC. Fig. 3.14 shows the loading pattern. With the measured resisting force from the ice beam, the flexural strength of level ice was calculated by using the equation 3.1.

Table 3.2 Measured flexural strength of three ice sheets

Ice sheet no.	Run no.	Unit	Model-scale	Full-scale
1	1	[MPa]	0.052	0.781
2	2	[MPa]	0.060	0.900
2	3, 5, 6	[MPa]	0.235	3.528
3	7, 8	[MPa]	0.046	0.688
3	9, 10	[MPa]	0.078	1.163

Fig. 3.14 Flexural strength measurements, cantilever beams

The shear strength of ice ridge was measured by using the punch tests. A frame with vertical cylinder was built to perform the punch test, as shown in Fig. 3.15 (a). A stiff and transparent plate was installed at the bottom of the cylinder in order to observe the situation of the rubbles, as shown in Fig. 3.15 (b). During the tests, the testing frame was pushed downward

at a speed of 0.007 m/s. According to the ITTC recommendation, the consolidated layer should be removed and the shear strength is determined by

$$\sigma_s = \frac{F}{D\pi h} \tag{3.2}$$

where σ_s is the shear strength, F is the pushing force, D is the diameter of cylinder, h is the depth of ridge keel. The measured flexural strength is shown in Table 3.2.
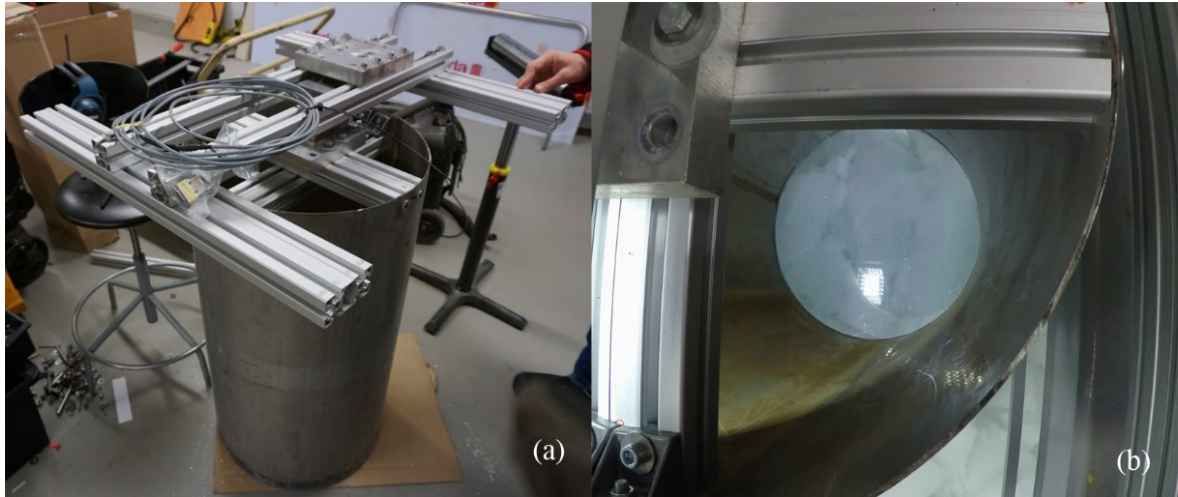
Fig. 3.15 Punch test frame (a) and testing scene (b)

3.5 Testing procedure

The experiment generated 3 ice sheets (level ice) to conduct the ice structure interaction tests. These three ice sheets had different thickness and their flexural strength was different from each other. Even for the same ice sheet, the flexural strength could be changed by using the tempering procedure. The flexural strength was measured after the tempering procedure and before the ice structure interaction tests. The measurement is shown in Table 3.2 and the thickness is shown in Table 3.3. When the ice sheets were generated, part of it was used to build the ice ridge following the procedure predicted in the previous section.

Table 3.3 Thickness of ice sheets

Ice sheet	Unit	Model-scale	Full-scale
1	[m]	0.043	0.645
2	[m]	0.040	0.600
3	[m]	0.042	0.63

The ice structure interaction tests were performed when the model ice and ice ridge were ready with proper geometric dimensions and mechanical properties. Each ice sheet could totally run four ice structure interaction tests as shown in Fig. 3.11. Only one test was performed for ice sheet 1. Four tests were performed in ice sheet 2 and 3, respectively.

In the ice structure interaction test, the structural model was fixed on the carriage and run through the ice sheet and ice ridge. It is estimated that ice drift velocity of engaging ice ridge around the Nordströmsgrund lighthouse is between 0.1 and 0.2 m/s so a full-scale ice drift velocity of 0.15 m/s was selected for the experiment. Consequently, the model-scale velocity should be 0.04 m/s according to Table 2.2. The model structure firstly run through the level

ice and subsequently through the ice ridge. When the model structure totally run out of the ridge, a whole run of ice structure interaction test stopped and withdrew to the starting position. Figure 3.16 shows the model run through the level ice and ice ridge.

(a) (b)
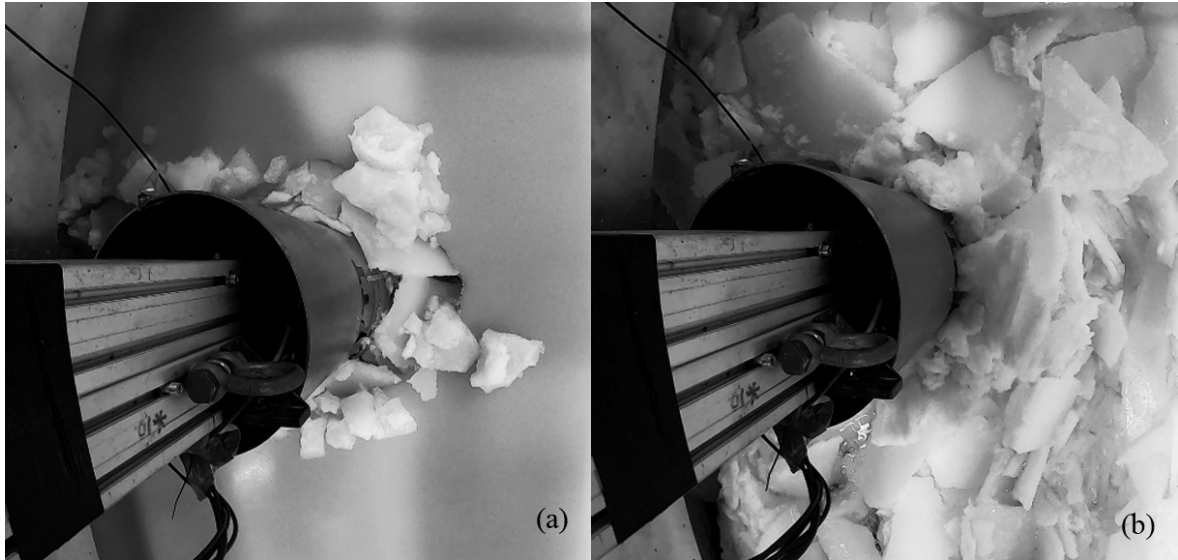
Fig. 3.16 Model structure running through the level ice (a) and ice ridge (b)

4 Data processing and analysis

The record of ice loads and relevant processed data are presented in this chapter. The history curves of ice loads are firstly shown in X, Y and Z directions. Most tests should subsequently contain curves of ice loads deriving from level ice before the ridge, ridge and level ice after the ridge. Table 4.1 shows the testing contents in each test. The symbol " √ " means this part of ice loads was measured during the test and "✕" means the absence of measurement. Tests no. 3 and 4 failed so they are not shown in this report.

Table 4.1 Testing contents of each test

Ice sheet no.	Test no.	Leve ice before ridge	Ridge	Leve ice after ridge	Structural type
1	1	✕	√	✕	vertical
2	2	√	√	√	vertical
2	3*	✕	✕	✕	vertical
2	5	✕	√	√	slope
2	6	√	√	√	slope
3	7	√	√	√	slope
3	8	√	√	√	slope
3	9	√	√	√	slope
3	10	✕	√	✕	vertical

* Test 3 failed at start because of too large ice load

Secondly, the load data is processed by using the Fast Fourier Transform (FFT) in order to show some properties of ice loads in the frequency domain. In addition, the envelope lines of ice loads are also presented in this chapter. The maximum values of ice loads are presented at the last part of this chapter, which are divided with the inducement: the rubble ice and breaking of level ice / consolidated layer.

4.1 History curve of ice loads

The load gauge measured the ice loads as three components according their directions. The X axis points in the reverse direction of motion of the model. The Y axis points the port side of the model. The Z axis points vertically upwards. For Test 1, 5 and 10, a channel was previously prepared, as shown in Fig. 4.1, so no ice loads were measured in the level ice before the ridge. The Test 1 and 10 failed before running through the ridge because the ice loads were too large and beyond the strength of the model. Nevertheless, the ice loads data could be used for studying the loads induced by the ridge so they are still presented in this report. Normally, the history curves show the data in such sequence: ice loads induced by the level ice in front of the ridge, ice loads induced by the ridge and ice loads induced by the level ice after the ridge. Figure 4.2~9 show the history curve of ice loads in X, Y and Z directions.

Fig. 4.1 Channel in the level ice before the ridge
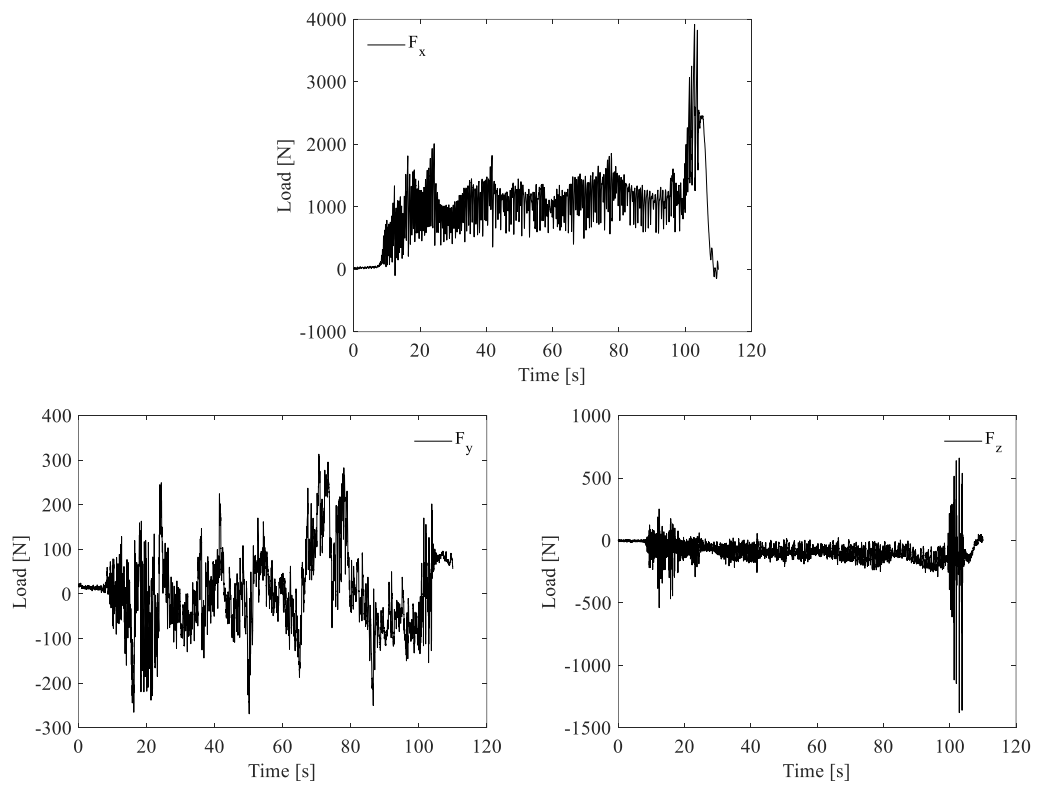
Fig. 4.2 History curve of ice loads for Test 1 (Vertical Structure)
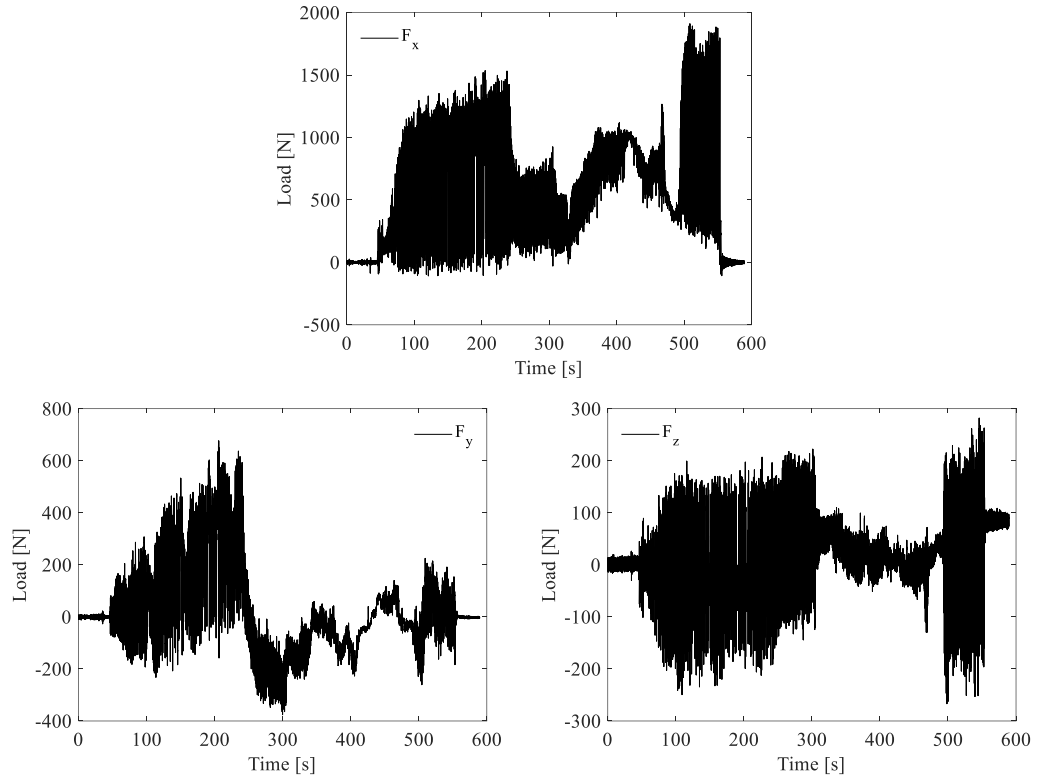
Fig. 4.3 History curve of ice loads for Test 2 (Vertical Structure)
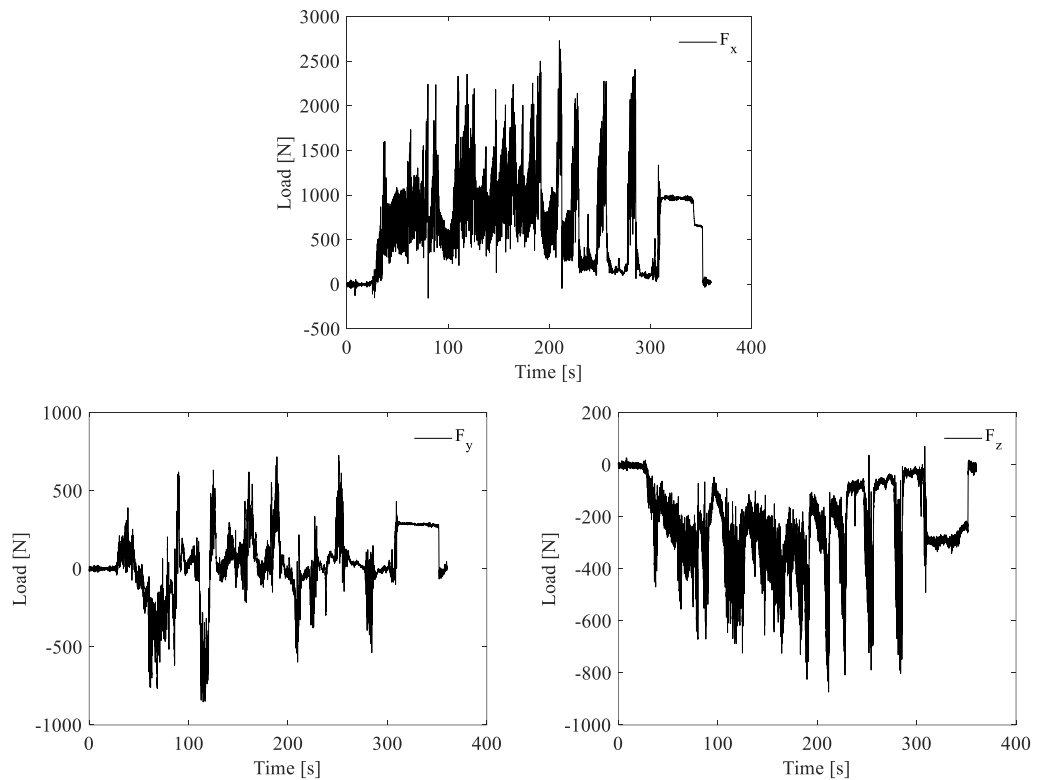
Fig. 4.4 History curve of ice loads for Test 5 (Slope Structure)
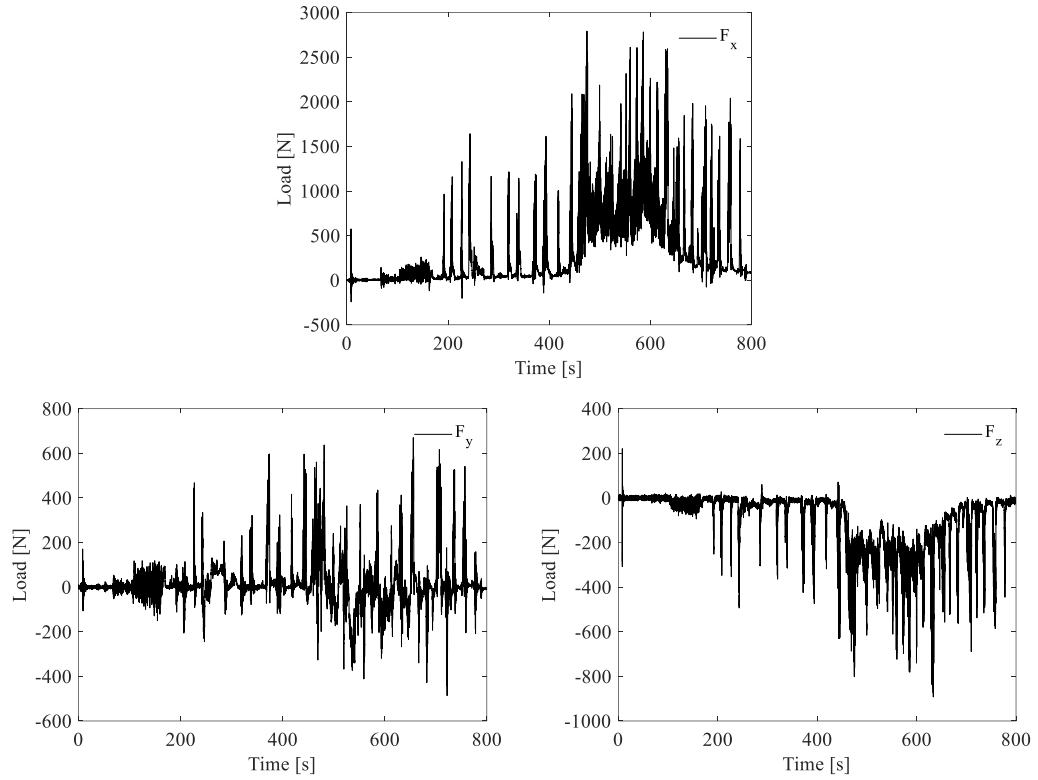
Fig. 4.5 History curve of ice loads for Test 6 (Slope Structure)
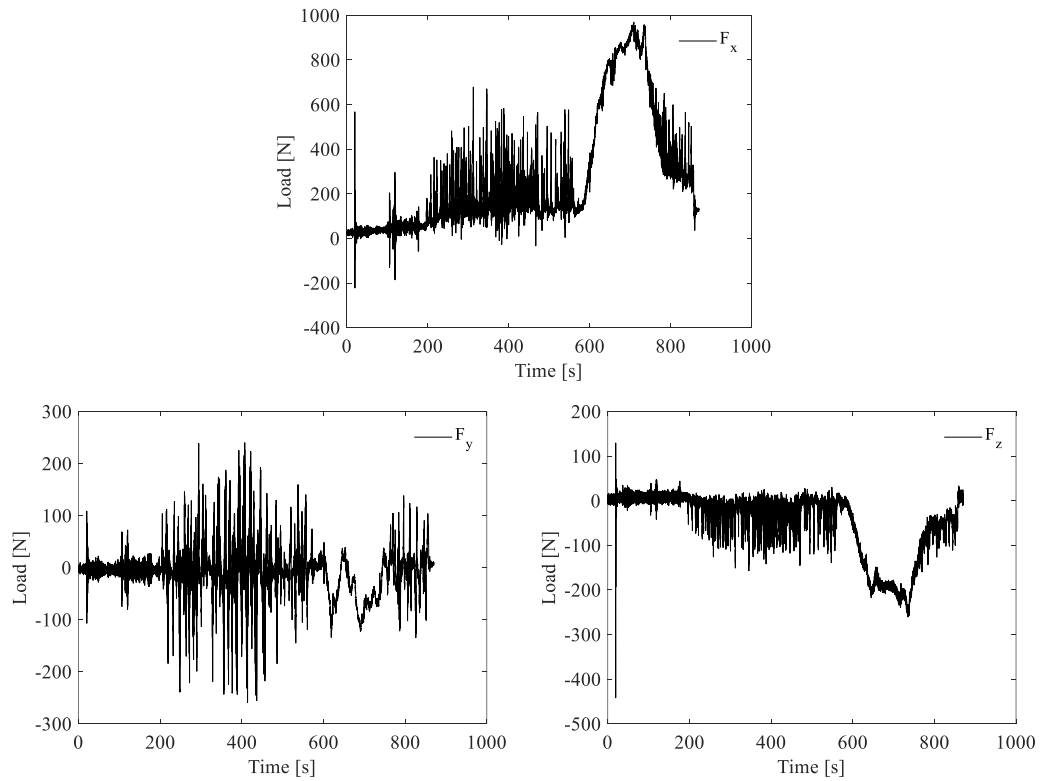
Fig. 4.6 History curve of ice loads for Test 7 (Slope Structure)
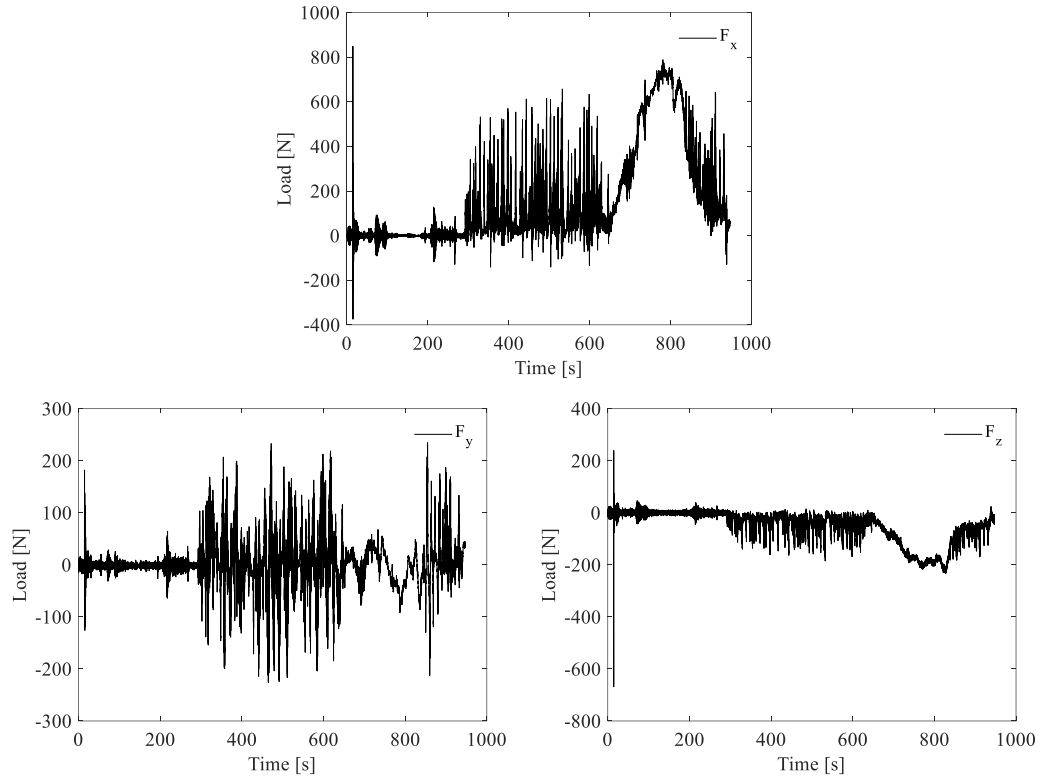
Fig. 4.7 History curve of ice loads for Test 8 (Slope Structure)
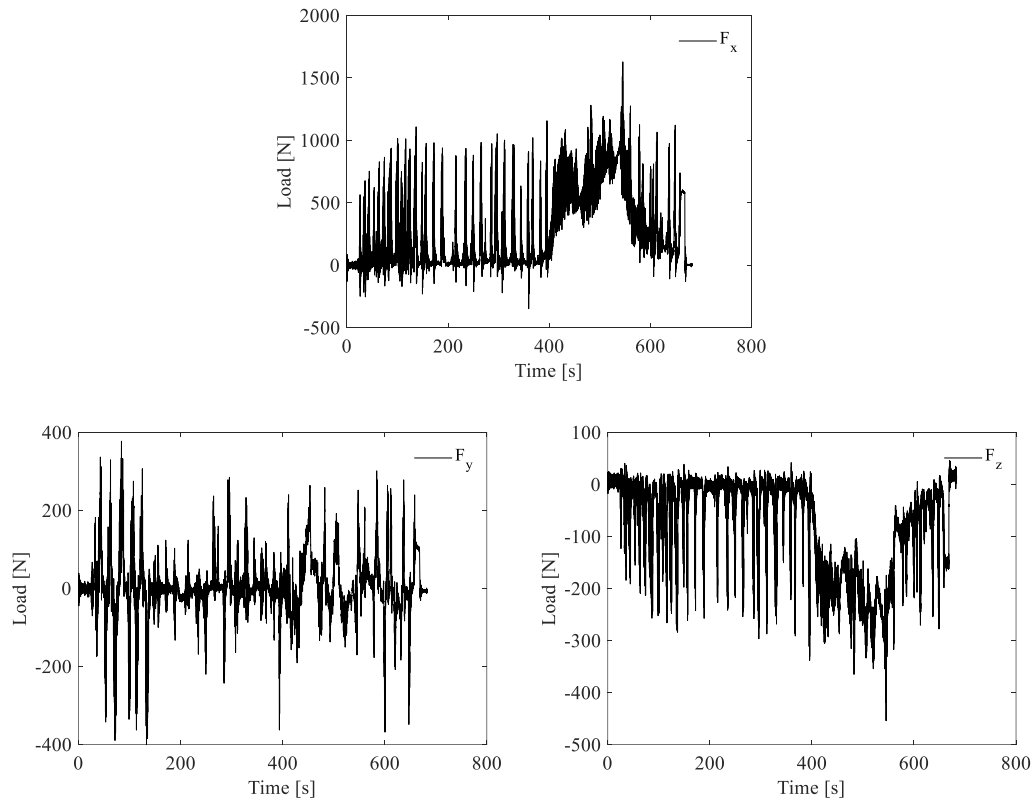
Fig. 4.8 History curve of ice loads for Test 9 (Slope Structure)
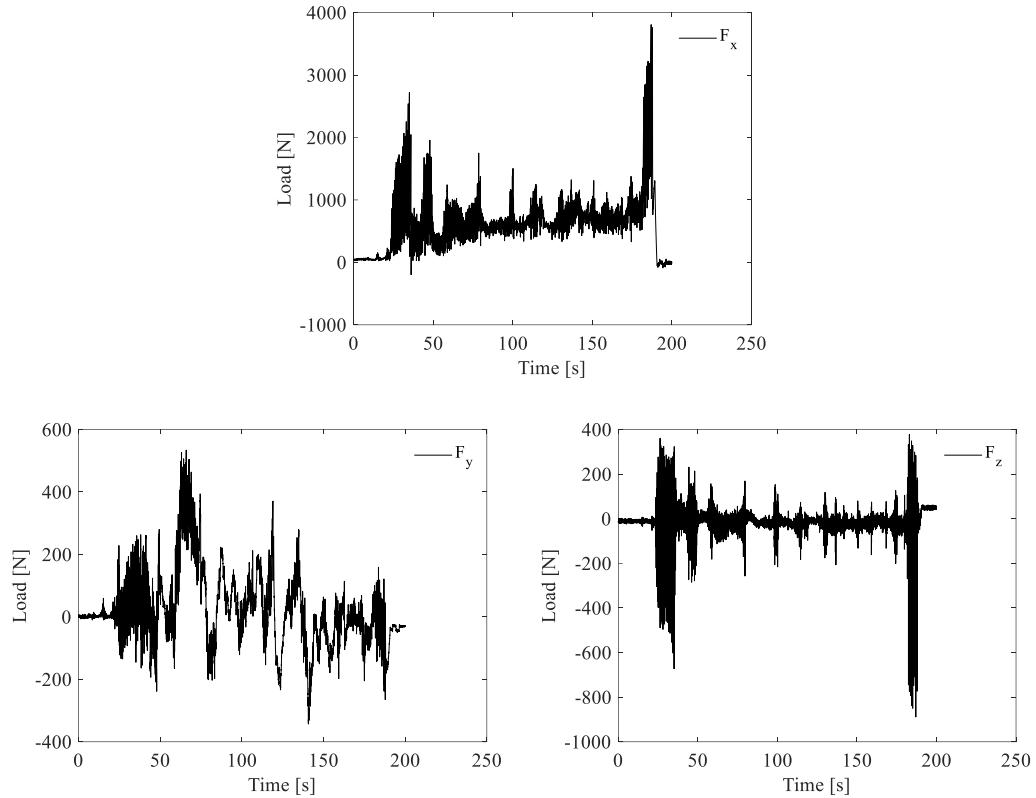
Fig. 4.9 History curve of ice loads for Test 10 (Vertical Structure)

4.2 *Envelope of history curve of ice loads*

The history curves of ice loads could be treated as an oscillation of signal. The extreme values of the curves could be outlined by using the envelope curves. The extreme ice loads, which is interesting for ice loads research, could be more apparently uncovered by using the envelope. The upper envelope could reveal the largest ice loads during a circle of ice breaking procedure. The lower envelope could reflect the trend of ice loads induced by the rubble to a certain extent. The research is most interested in the ice loads in X direction and the value of forces in X direction is much larger than those in Y & Z directions. Therefore, the upper and lower envelope curves are only presented for the ice loads in X direction, as shown in Fig. 4.10~17. Figure 10 shows the agreement between the envelope curve and the load history curve, as an example.

The upper envelope curves are considered total ice loads and the lower envelope curves are considered ice loads induced by the rubble. Thus, the difference between the upper and lower envelope curves could be considered the ice loads induced by the level ice or consolidated layer. Please note that the lower envelope could underestimate the rubble loads due to the vibration of the structure. Consequently, the level ice load could be overestimated. Nevertheless, the evolution of rubble load magnitude could be uncovered by the lower envelope.
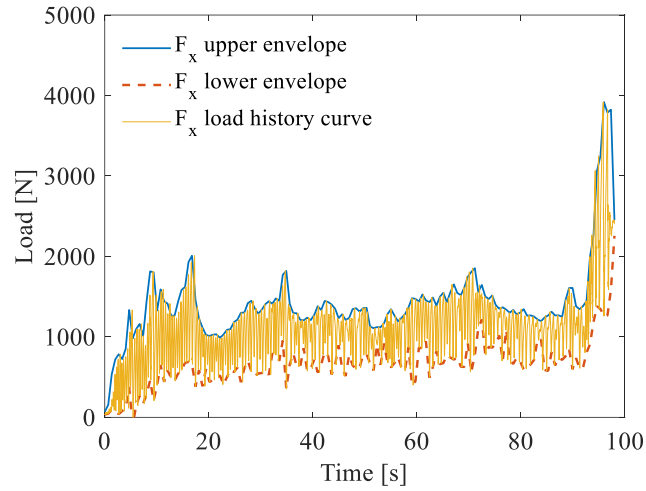
Fig. 4.10 Envelope curves of ice loads in X direction for Test 1 (Vertical Structure)
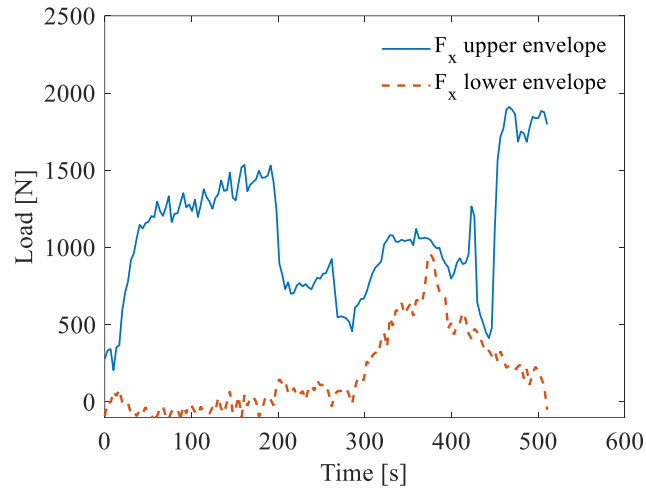
Fig. 4.11 Envelope curves of ice loads in X direction for Test 2 (Vertical Structure)
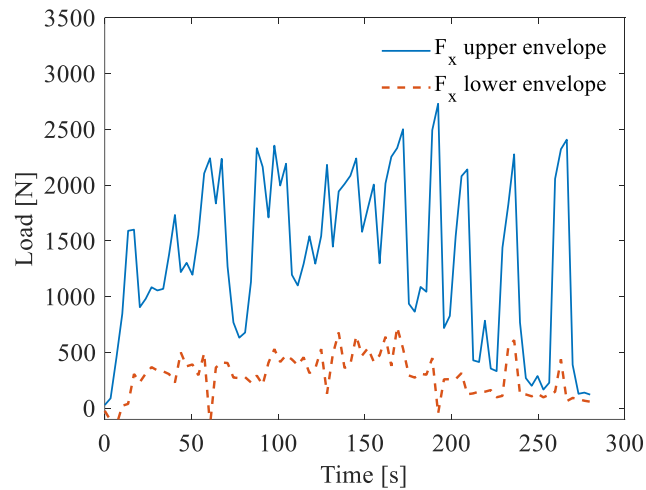
Fig. 4.12 Envelope curves of ice loads in X direction for Test 5 (Slope Structure)
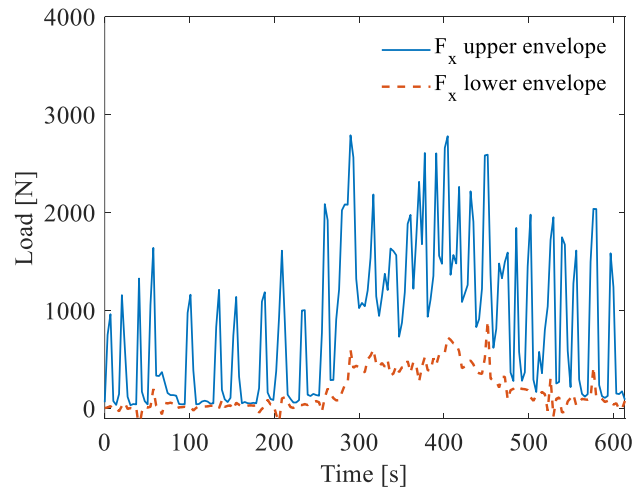
Fig. 4.13 Envelope curves of ice loads in X direction for Test 6 (Slope Structure)
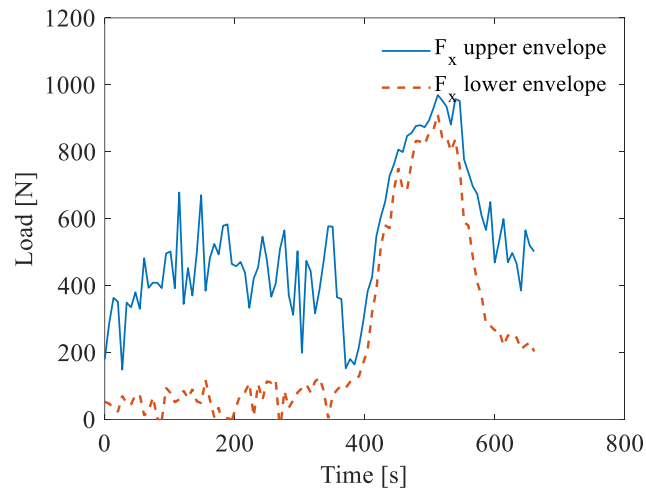
Fig. 4.14 Envelope curves of ice loads in X direction for Test 7 (Slope Structure)
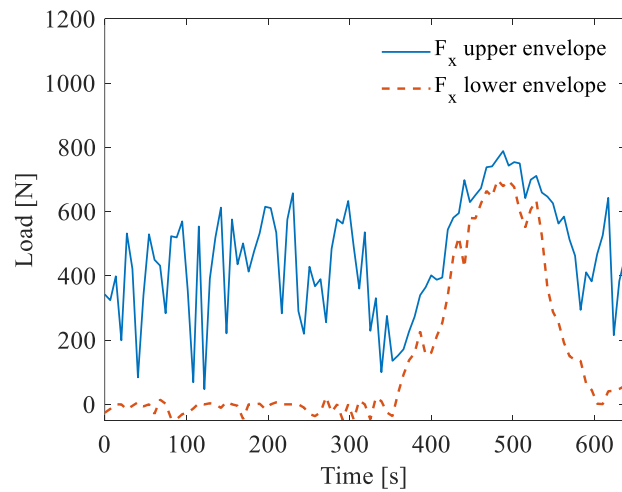
Fig. 4.15 Envelope curves of ice loads in X direction for Test 8 (Slope Structure)
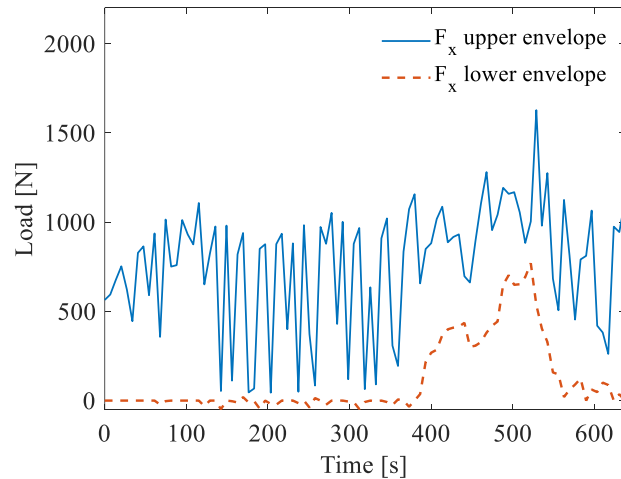
Fig. 4.16 Envelope curves of ice loads in X direction for Test 9 (Slope Structure)
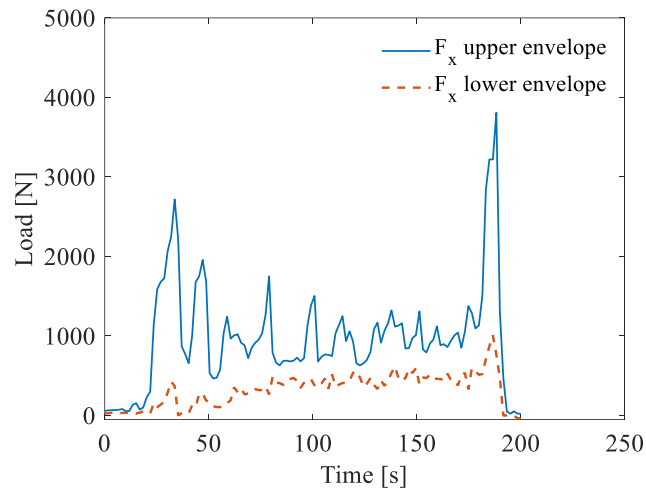
Fig. 4.17 Envelope curves of ice loads in X direction for Test 10 (Vertical Structure)

4.3 Components of ice loads

According to the inducement, the ice loads could be separated into two parts: 1) ice loads induced by the level ice or consolidated layer; 2) ice loads induced by the rubble. Based on the previous envelope curves, the level ice load is calculated with the difference between the upper and lower envelope curves. The maximum components of tests are presented in Figures 4.18~20, which present the components of ice loads in various areas: the level ice before ridge, ridge and the level ice after ridge. Please note that the maximum level ice loads and maximum rubble loads could happen at different time for each test so their sum was possibly larger than the total loads.
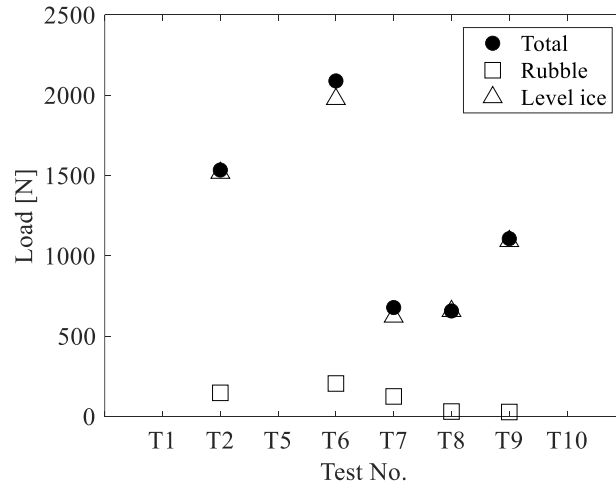
Fig. 4.18 Ice load components in the area of level ice before the ridge
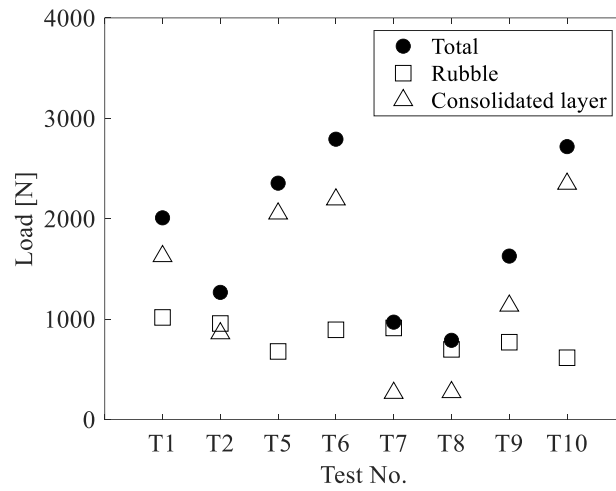
Fig. 4.19 Ice load components in the area of ridge
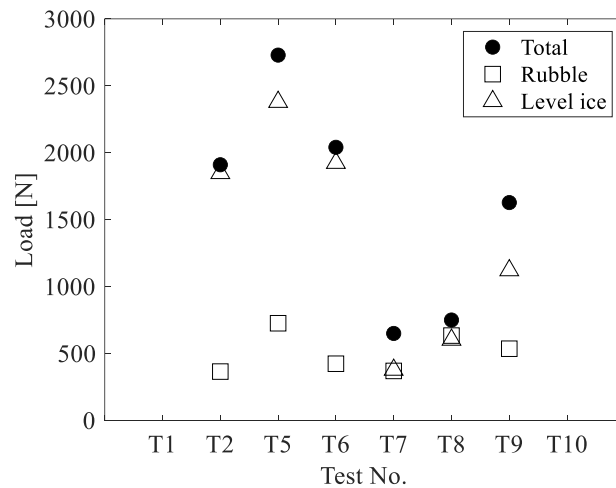
Fig. 4.20 Ice load components in the area of level ice after the ridge

4.4 Fast Fourier transform of ice loads

The Fourier transform decomposes the history curve of ice loads into constituent frequencies and presents the distribution of ice loads in the frequency domain. By using the Fourier

transform, it is obvious to show at which frequencies the ice loads most happened. This is important because the resonance might happen if the natural frequency of the structure is close to frequency at which most ice loads happens. It should note that the ice loads include the response effect of the structure and not pure dynamic ice loads. The Fast Fourier transforms of ice loads are shown in Fig. 4.21.
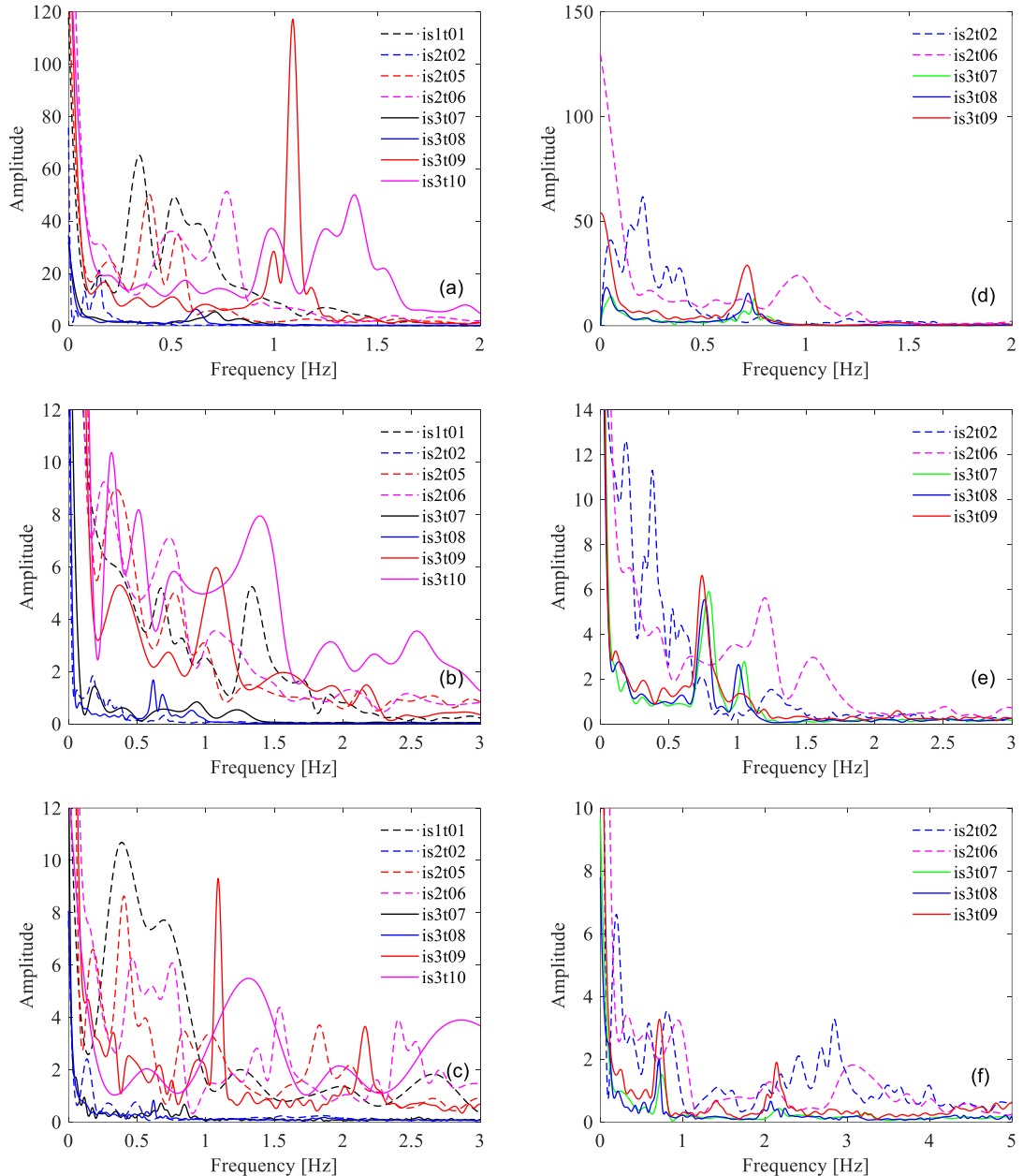
Fig. 4.21 FFT of ice loads: (a) ridge loads in X direction; (b) ridge loads in Y direction; (c) ridge loads in Z direction; (d) level ice loads in X direction; (e) level ice loads in Y direction; (f) level ice loads in Z direction

4.5 Distribution and return period of peak ice loads

The history curve of ice loads consists of a large number of oscillations due to the flaking or the procedure of bending failure. The peak value of each oscillation is selected to represent the load within this oscillation, as shown in Fig. 4.22. The oscillations with high frequency are ignored because they transmitted too little energy to the structure, which could be

disclosed in the FFT analysis. The distribution and return period are useful tools to analyze the ice loads on structures. They are of help to reveal the physical properties and mechanism of ice loads.
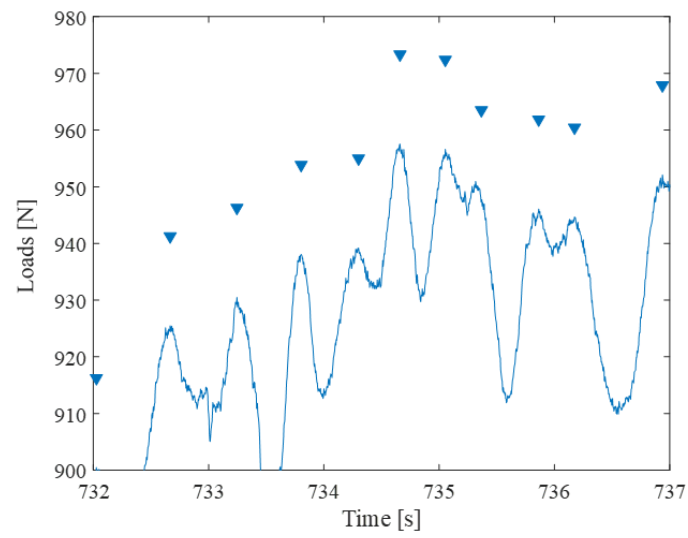
Fig. 4.22 Data selection of ice loads
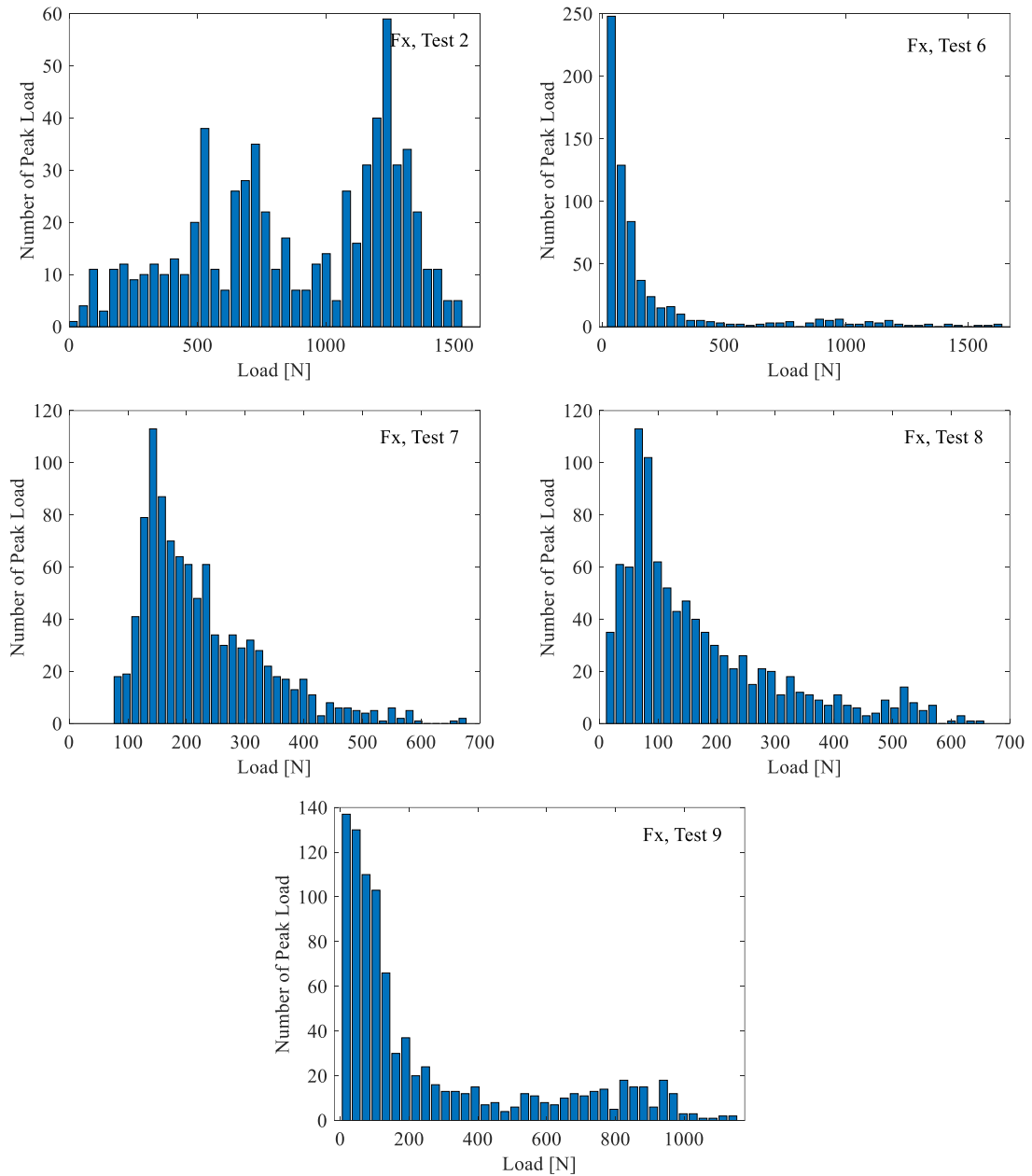
Fig. 4.23 Distribution of level ice loads in X direction (Vertical Structure: Test 2; Slope Structure: Test 6~9)
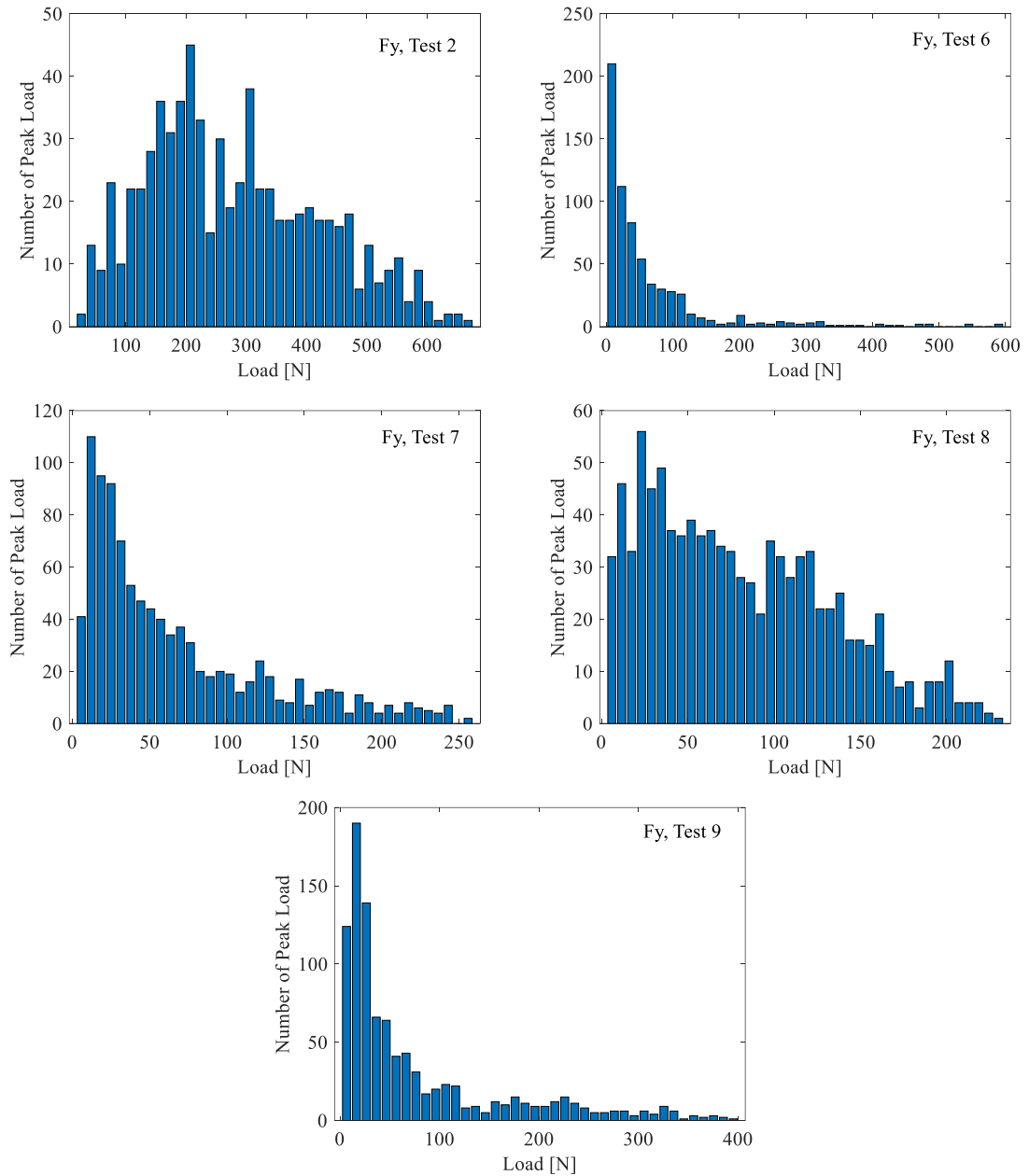
Fig. 4.24 Distribution of level ice loads in Y direction (Vertical Structure: Test 2; Slope Structure: Test 6~9)
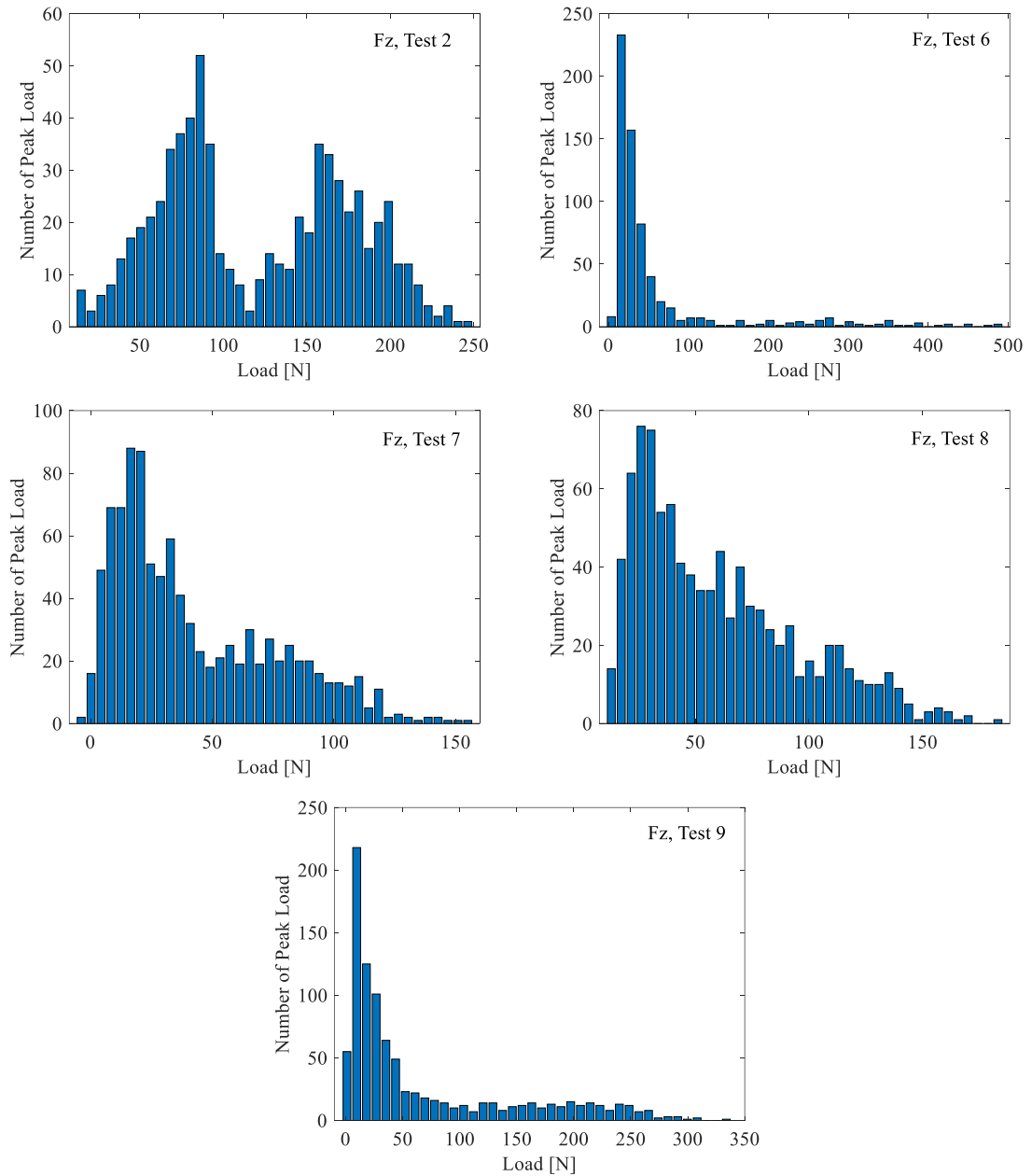
Fig. 4.25 Distribution of level ice loads in Z direction (Vertical Structure: Test 2; Slope Structure: Test 6~9)
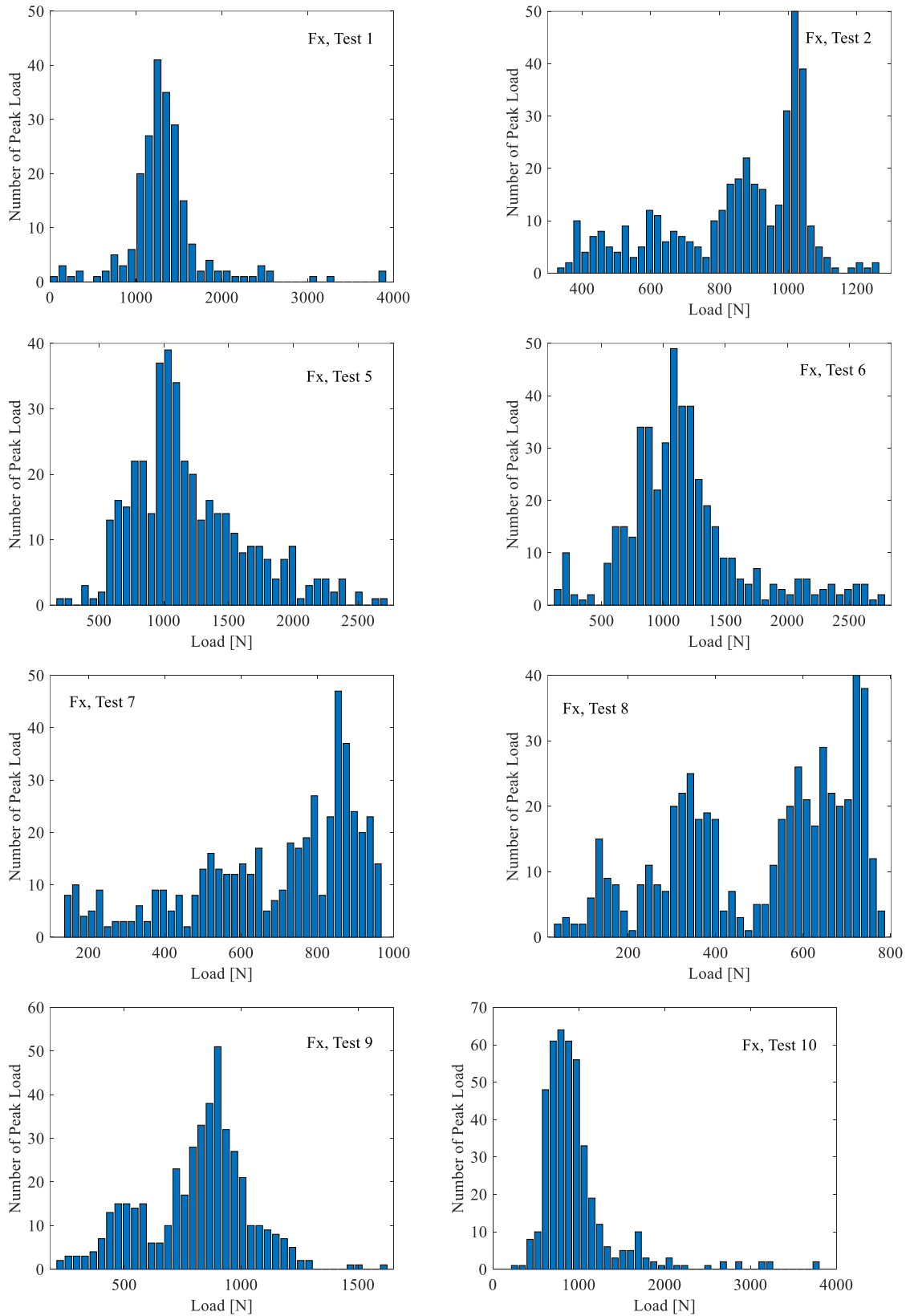
Fig. 4.26 Distribution of ridge loads in X direction (Vertical Structure: Test 1,2 & 10; Slope Structure: Test 5~9)
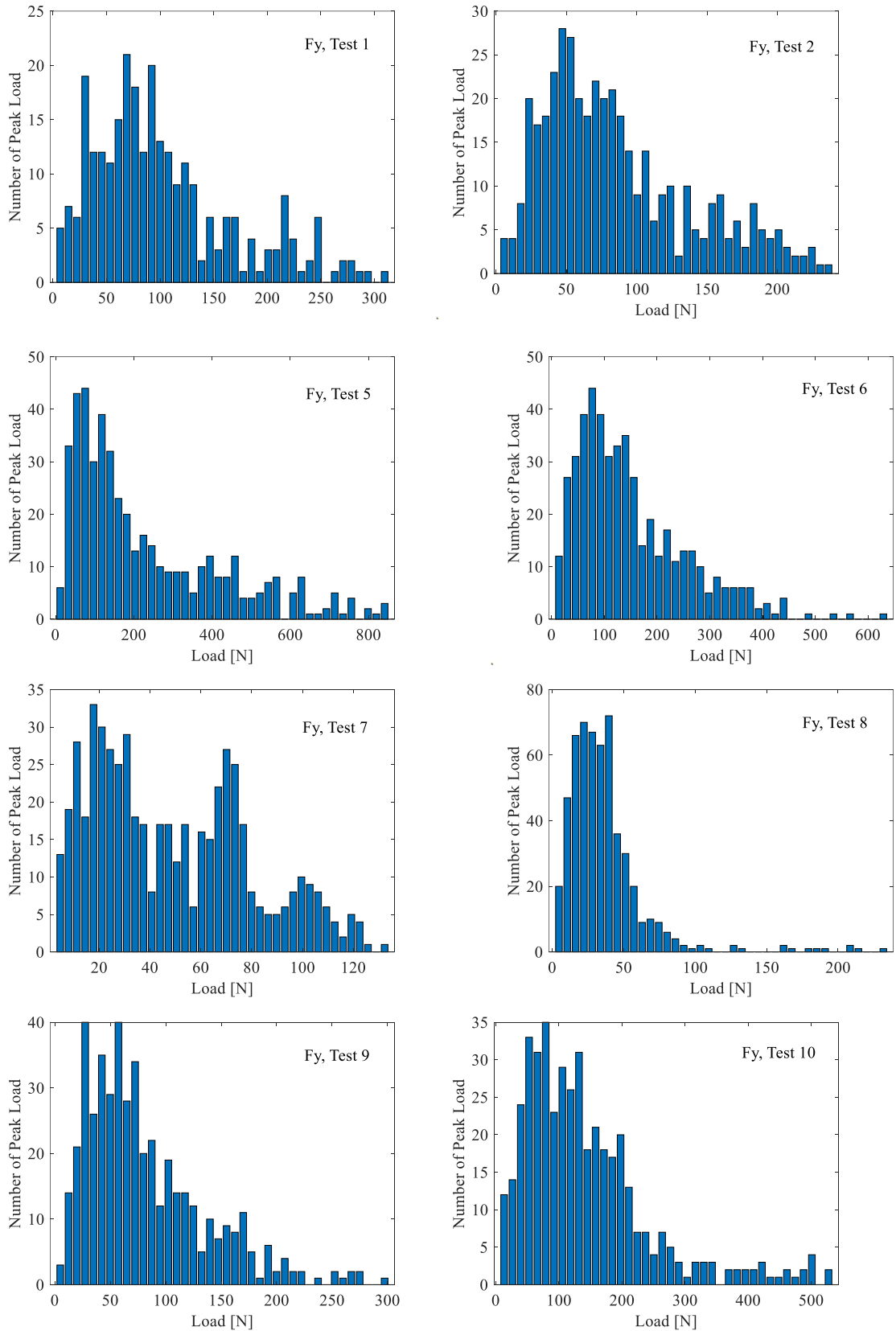
Fig. 4.27 Distribution of ridge loads in Y direction (Vertical Structure: Test 1,2 & 10; Slope Structure: Test 5~9)
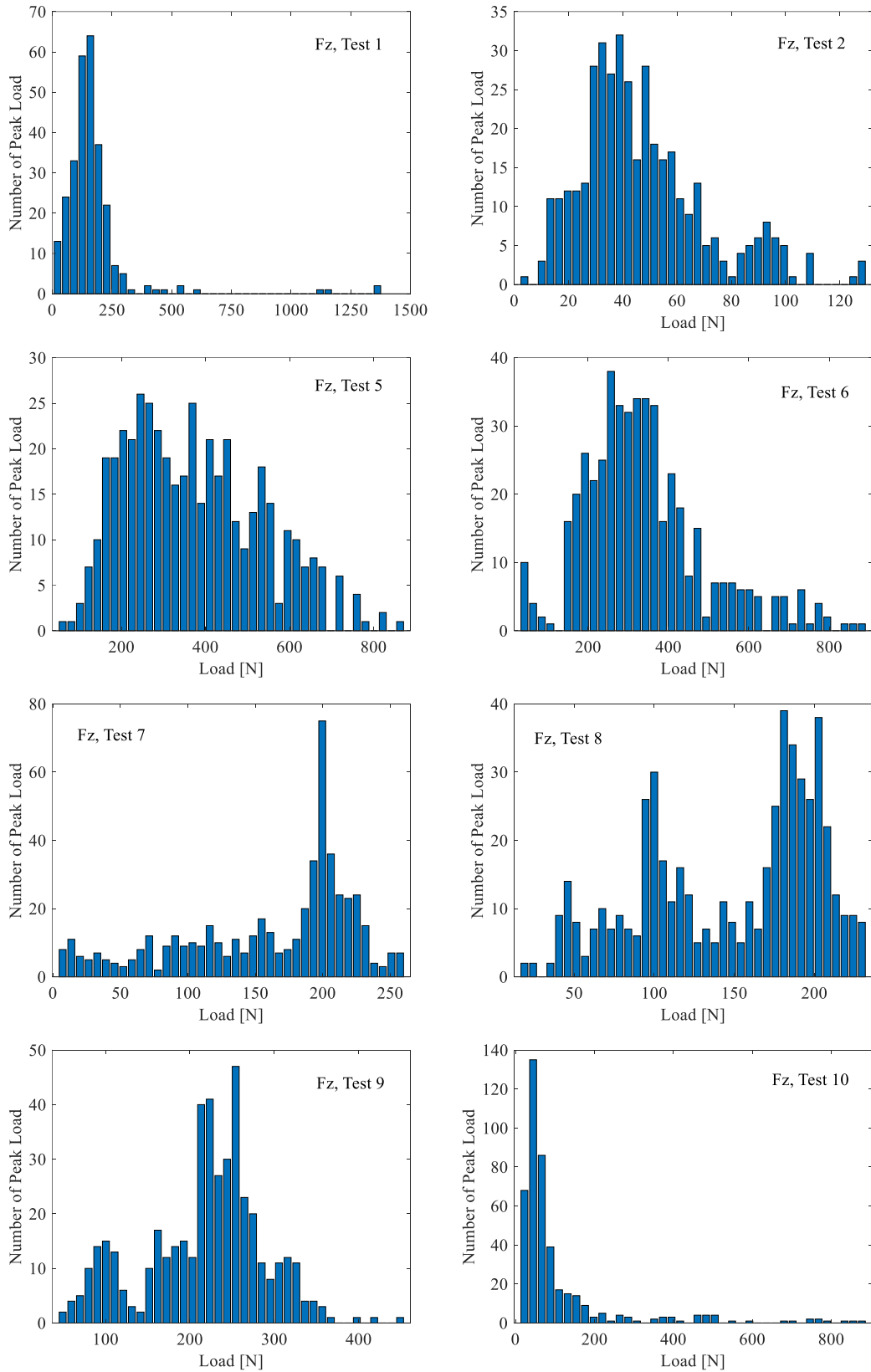
Fig. 4.28 Distribution of ridge loads in Z direction (Vertical Structure: Test 1,2 & 10; Slope Structure: Test 5~9)
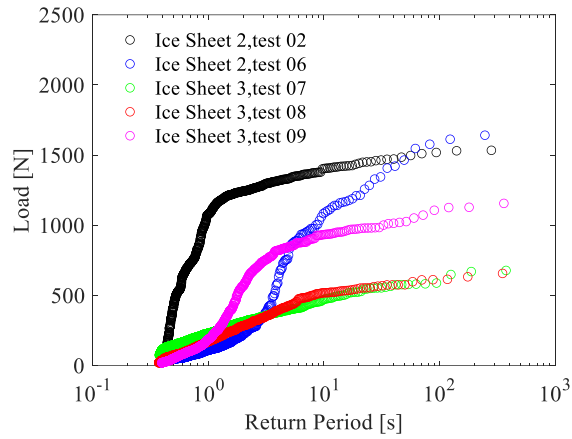
Fig. 4.29 Return period of level ice loads in X direction (Vertical Structure: Test 2; Slope Structure: Test 6~9)
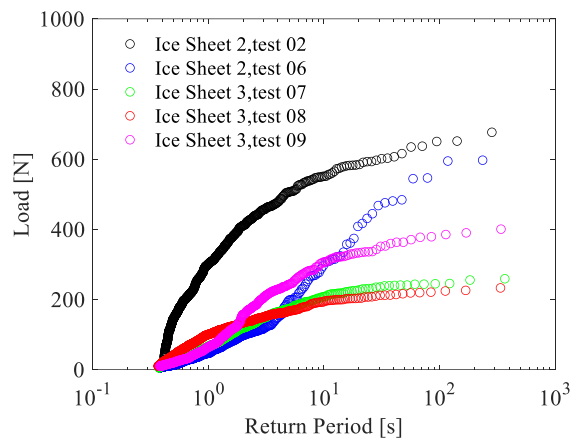
Fig. 4.30 Return period of level ice loads in Y direction (Vertical Structure: Test 2; Slope Structure: Test 6~9)
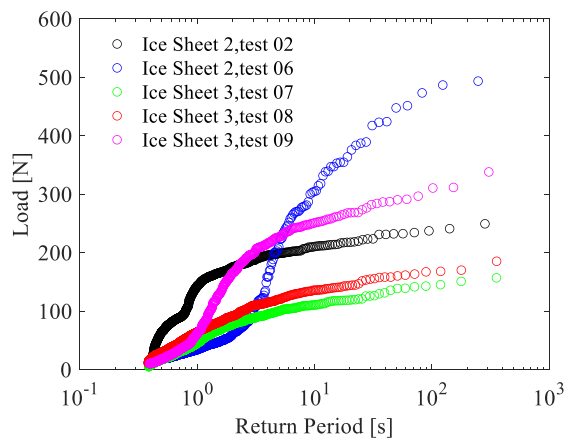
Fig. 4.31 Return period of level ice loads in Z direction (Vertical Structure: Test 2; Slope Structure: Test 6~9)
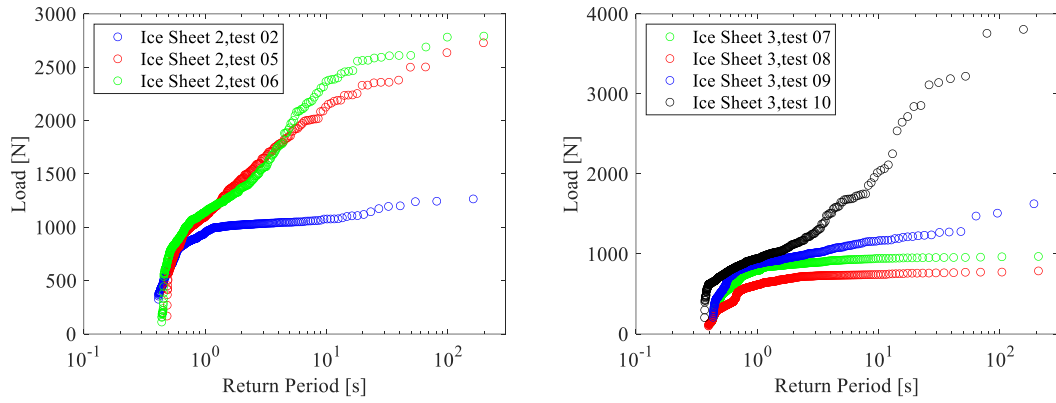
Fig. 4.32 Return period of ridge loads in X direction (Vertical Structure: Test 2 & 10; Slope Structure: Test 5~9)
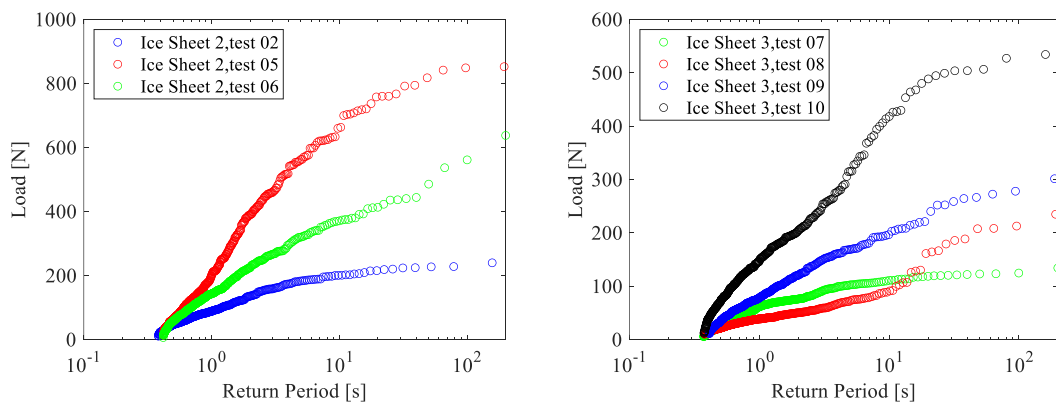
Fig. 4.33 Return period of ridge loads in Y direction (Vertical Structure: Test 2 & 10; Slope Structure: Test 5~9)
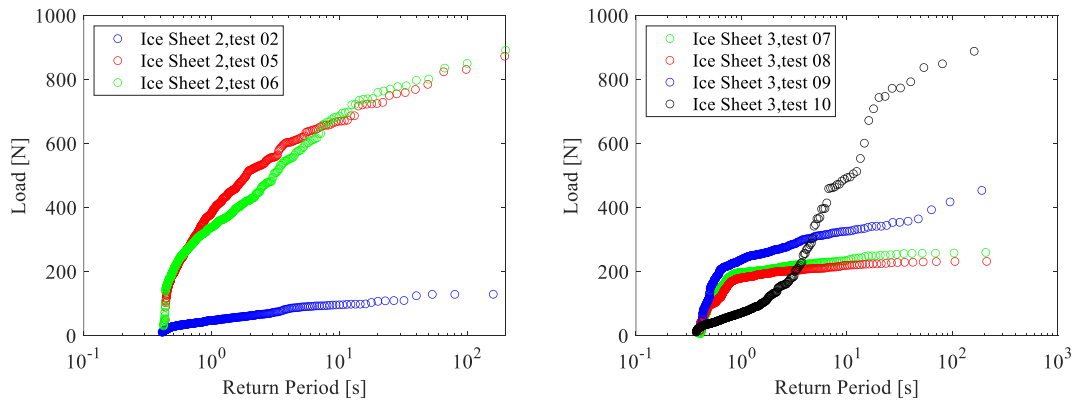
Fig. 4.34 Return period of ridge loads in Z direction (Vertical Structure: Test 2 & 10; Slope Structure: Test 5~9)

5 Summary of the main findings

The level ice and ice ridge induce loads with different features so this chapter discusses the loads induced by the level ice and the ice ridge, respectively. The ice structure interaction can be affected by many parameters, which include ice properties, structure type (vertical / slope) and boundary conditions. It should be noted that the structure type only had apparent influence on the interaction between the structure and level ice because the conical section was too short comparing to the whole length of the structure, as shown in Fig. 3.10. For the tests with conical section, the total draft was 1.12 m but the draft of conical section was only 0.2 m. Therefore, the effect of structure type is individually discussed in the section of level ice.

5.1 Level ice

5.1.1 Structure type

The model used in this experiment consisted of two sections: cylindric section and conical section. The detail of its structural dimension is described in section 3.3. Consequently, the experiment studied the interaction between the ice and cylindric column and conical structure during 9 tests. By analyzing the data from these tests, it was possible to discover the influence of vertical and slope structure on the ice loads and the ice structure interaction. Table 4.1 presents the structural type at each test.

At test 3, the flexural strength of ice was very large. For the detail, please see Table 3.2. As a result, the ice loads sharply increased to a value beyond the strength of the model so Test 3 failed and aborted at the start of this test. Figure 5.1 shows the history curve of ice loads in the X direction. It shows that the ice loads increase to approximate 4000 N in 15 s after contacting the ice. Therefore, Test 5 and 6 employed the slope section to study the ice structure interaction because the slope side can normally reduce the ice loads on the structure. The slope structure can reduce the ice loads because the ice failure mode is different from the ice failure mode during the interaction with vertical structures. The failure modes in the contact with vertical and slope structures have been introduced in the section 2.3.
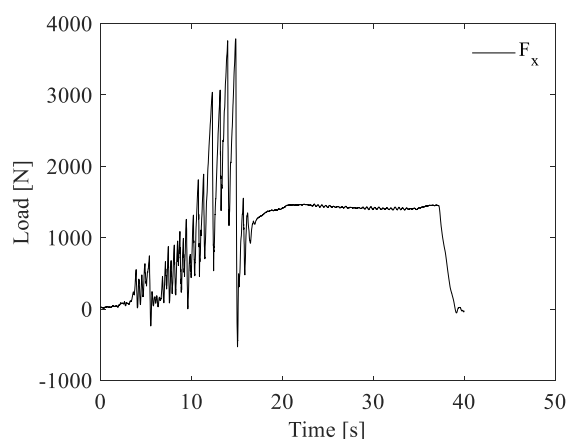
Fig. 5.1 History curve of ice loads in X direction for Test 3 (Vertical Structure)
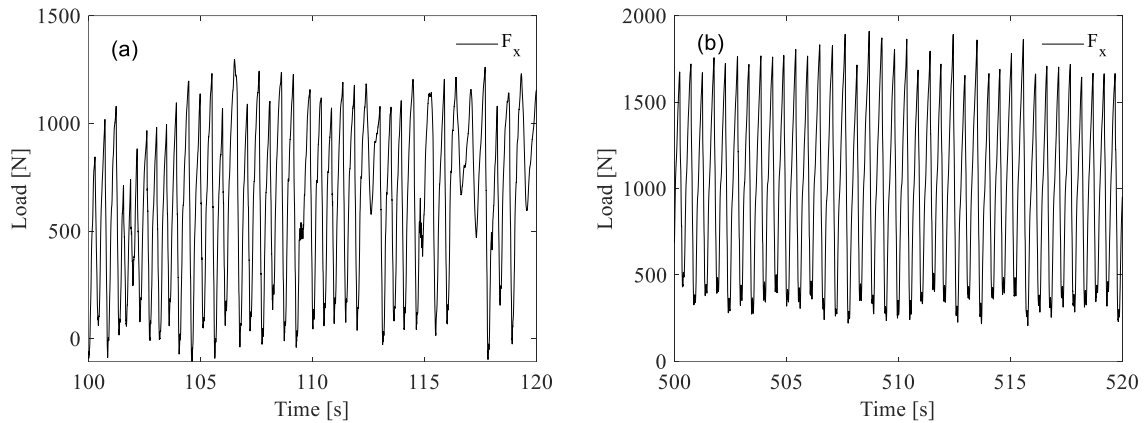
Fig. 5.2 History curve of level ice loads for Test 2; (a) before ridge, (b) after ridge
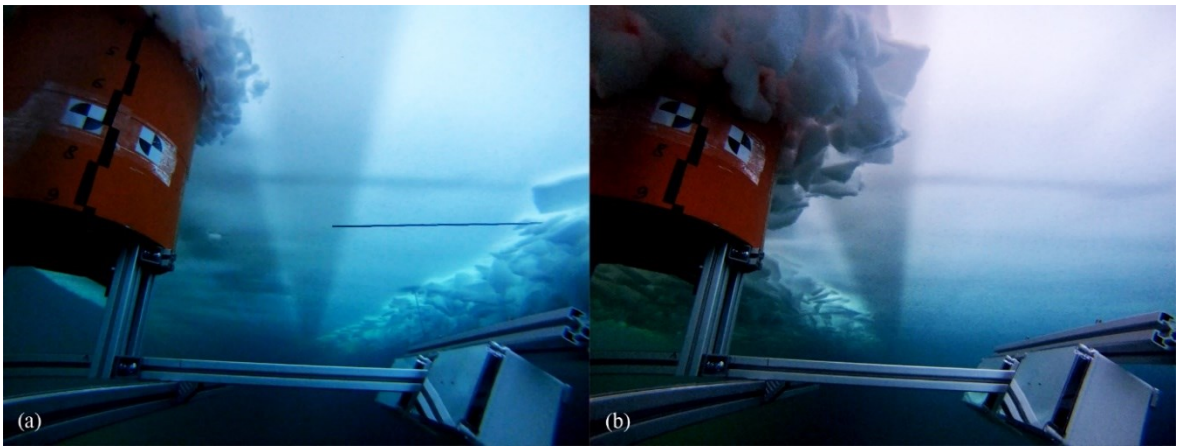
Fig. 5.3 Rubble accumulation in front of the model; (a) before ridge, (b) after ridge

Figure 5.2 shows the history curve of level ice loads on the vertical structure before and after the ridge. It shows that the high frequency oscillation is much more obvious than the low frequency oscillation. This reflects that a continuous crushing process dominates the ice failing process in front of the vertical structures. As shown in Fig. 2.18, the ice loads accumulate until they reach the peak, where the ice fails with multi-level flaking. After the peak, the ice loads suddenly drop because of the large flaking. When the ice loads drop to the lowest value, the next circle starts and the failing process continue as before. It is interesting that some troughs are lower than zero in Fig. 5.2 (a), which means the force is in the same direction with the motion of model. This phenomenon is attributed to the dynamic response of the structure. In addition, the rubble accumulation was small so the ice loads from rubble was small and could not compensate the effect of structure's dynamic response. In contrast, the troughs in Fig. 5.2 (b) are larger than zero because the rubble accumulation is much larger after the model past through the ridge, as shown in Fig. 5.3. The additional rubbles were from the ridge keel and did not clear out when the structure totally cut through the ridge. This could be verified by the size of rubbles.
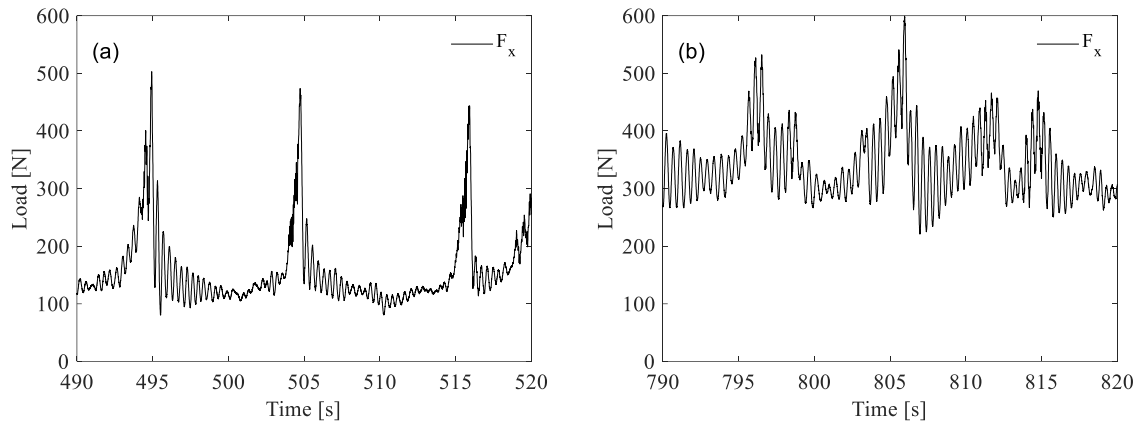
Fig. 5.4 History curve of level ice loads for Test 7; (a) before ridge, (b) after ridge

Figure 5.4 shows the history curve of level ice loads on the slope part of the model. It is obvious that the low frequency oscillation was much stronger than the high frequency oscillation. The highest ice loads occurred at the crests of low frequency oscillation. The period of low frequency oscillation depended on the moving velocity and the distance between the contact point and the bending failure point. As shown in Fig. 5.5, the failure mode consisted of three stages. At stage 1, the structure started to contact the ice and the ice loads accumulated until they reached the highest value, where the ice was failed by bending. Here, the high frequency oscillation was attribute to the crushing or flaking of the ice. At stage 2, the ice loads dropped because of the bending failure. This stage lasted very short time. In this example, the time was shorter than 0.5 second. At stage 3, the structure vibrates due to the sudden drop of the ice loads and the vibration declines due to the damping of rubbles, water and structure.
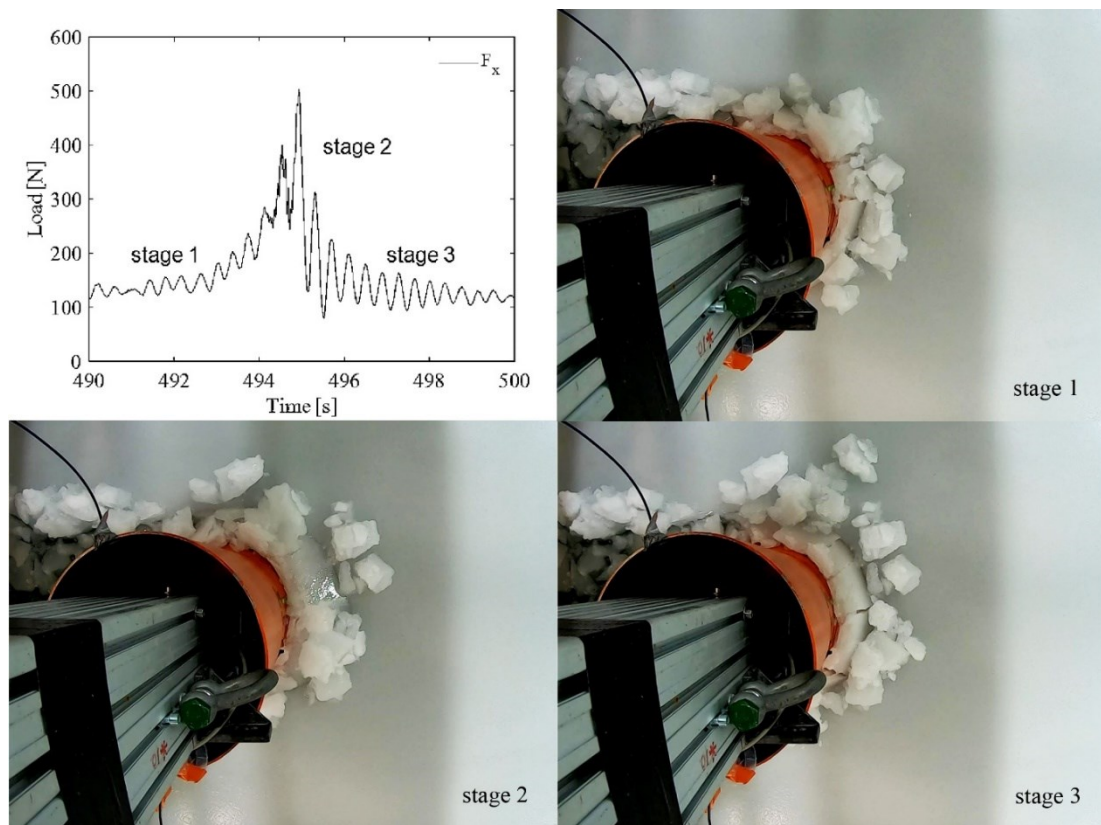
Fig. 5.5 Stages of bending failure mode, Test 7 (Slope Structure)

The amplitude of low frequency oscillation was smaller in Fig. 5.4 (b) than that in Fig. 5.4 (a). This was attributed to the larger accumulation of rubble, which could provide larger buoyant force. Thus, less vertical force was needed from the structure to fail the ice by bending. However, the ice loads from the rubble was larger so the total ice loads might be larger.

5.1.2 Components of level ice loads

The total ice loads could be decomposed into two parts according to the inducement: ice loads from rubble and ice loads from breaking level ice / consolidated layer. Figure 4.18~20 present the components of ice loads at each test. By comparing the data from Test 2 and Test 9, the research shows that the slope structure could reduce the total ice loads by reducing the loads for breaking level ice. The flexural strength and ice thickness at Test 2 were 0.06 MPa and 0.04 m, respectively. The flexural strength and ice thickness at Test 9 were 0.078 MPa and 0.042m, respectively. It is clear that both flexural strength and thickness were larger at Test 9. However, the maximum total ice loads were larger before and after the ridge at Test 2. This was mainly because of the obvious decrease of the load for breaking the level ice. As to the rubble loads, it was not obvious to discover the influence of the structure type.

The international standard (ISO 19906, Petroleum and natural and industries – Arctic offshore structures) is employed to calculate the ice loads on vertical structures. The parameters for Equation 2.14 and 2.15 are: C_R=1.8 MPa (This value is selected because the prototype locates in the Baltic Sea); w=8.13 m; the ice thickness h=0.645 m for Test 1, h=0.6 m for Test 2 and h=0.63 m for Test 10. All the values were from the experimental measurement except C_R. Please note that the values of above parameter are the full-scale value so the calculated ice loads should be divided by the cubic of geometric scale λ in order to compare to the measurement.

The Ralston's model (1977) is employed to calculate the ice loads on slope structures. The parameters for Equation 2.26 and 2.27 are: the flexural strength σ_f=3.53 MPa for Test 5 & 6, σ_f=0.69 MPa for Test 7 & 8, σ_f=1.16 MPa for Test 9; the ice thickness h=0.6 m for Test 5 & 6, h=0.63 m for Test 7, 8 & 9; ρ_w=1025 kg/m^3; D=8.1 m; D_t=5.2 m; the coefficients A_i (i=1~4) and B_i (i=1~2) are obtained from Fig. 2.31.

The calculated results are presented with red symbols in Fig. 5.6 and 5.7. It shows that both methods were conservative for the total ice loads except the ice load after the ridge at Test 9. The components of level ice were always conservative or similar to the measurement by using the Ralston's model. However, the rubble components were overestimated in the region before the ridge but underestimated in the region after the ridge. It is understandable because the structure brought much rubbles from the ridge keel when it passed through the ridge, especially before clearing the additional rubbles.
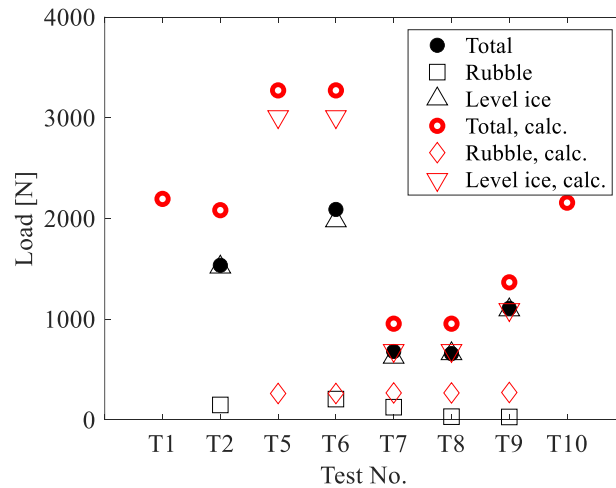
Fig. 5.6 Ice load components in the area of level ice before the ridge

The rubble accumulation was small before the ridge, as shown in Fig. 5.3(a) so the rubble loads were small, as shown in Fig. 5.6, and the main contribution was from the breaking of level ice. Thus, the total ice loads were dominated by the properties of level ice, such as the flexural strength and thickness. Test 2 was conducted before the consolidating procedure and Test 6 was conducted after the consolidating procedure, as shown in Fig. 3.8. As a consequence, the flexural strength at Test 6 was 3.53 MPa, much larger than 0.9 MPa at Test 2. Therefore, the maximum total ice load was larger at Test 6 even though the structure type was slope at Test 6 and it is vertical at Test 2. Test 7, 8 & 9 had identical ice thickness and structure type. The only difference was the flexural strength so the difference of ice loads could be considered dominated by the flexural strength and larger strength yielded larger ice loads.
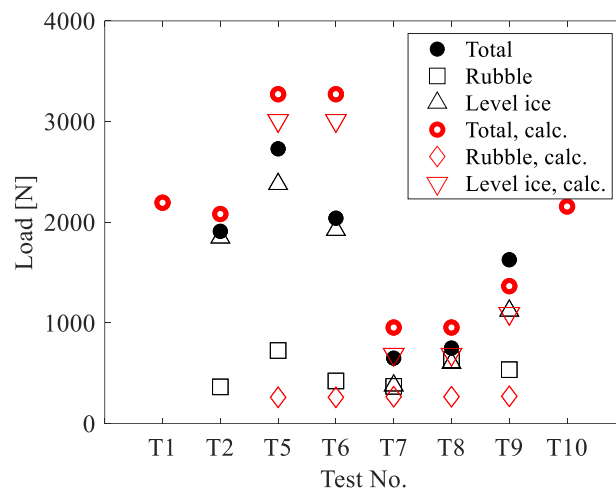
Fig. 5.7 Ice load components in the area of level ice after the ridge

Figure 5.7 shows the level ice loads are distinctly larger than the rubble loads at Test 2, 5,6 & 9. However, the level lice loads are close to the rubble loads at Test 7 & 8. This could be attributed to the small flexural strength. In addition, the rubbles taken from the ridge increased the rubble loads. These two reasons resulted in the close magnitude of level ice loads and rubble loads.

According to equation 2.26, the rubble loads are dependent on the geometric dimension of slope structure so the calculated values are equal for all test with slope structures, as shown in Fig. 5.7. However, the maximum measured rubble loads were rather divergent between

tests. For example, the measured rubble load at Test 5 was approximately 2 times the value of Test 7 even though the structures have identical geometric dimension at these two tests. Another example is the obvious difference between Test 5 and 6. Test 5 and 6 were conducted in the same ice sheet and they all had the same structure type. However, the maximum rubble loads apparently diverse.

This phenomenon was in compliance with the full-scale experiments, which show a large scatter of measured peak ice load values (Daley et al., 1998; Jordaan, 2001). Ranta et al. (2018a) indicates that the random values of ice loads are induced by the complex interaction process, which includes many physical parameters. These parameters could slightly vary from one breaking to one breaking. As a result, the ice loads could be random in value in different breaking cycles. The varying parameters could be the properties of ice material, such as thickness and flexural strength. Paavilainen and Tuhkuri (2012) report that the ice thickness has a strong effect on the horizontal ice loads but the effect of tensile strength is not observed, where the tensile strength is used to describe the ice strength instead of flexural strength. Unfortunately, the thickness was not measured at these locations of bending failure. Ranta et al. (2018b) propose an equation to show the relationship between the maximum horizontal peak loads P and the broken rubble length L_f

$$P = \frac{k^2 L_f^3 + 4k(K_1+K_2)L_f^2 + 12K_1K_2L_f}{12(kL_f+K_1+K_2)} \tag{5.1}$$

where $k = \rho_w g$ is the modulus of the foundation, ρ_w is the water density, g is the gravitational acceleration, K_1 & K_2 are the spring constant at two ends of the broken rubble. The definition of broken rubble length is

$$L_f = \chi L_c = \chi \sqrt[4]{4EI/k} \tag{5.2}$$

where L_c is the characteristic length of the ice beam, E is the modulus of elasticity and I is the moment of area of the ice beam. According to the equation 5.1, it could be deduced that the maximum horizontal ice load is proportional to the broken rubble length. This was in compliance with the observation of this experiment. Fig. 5.8 shows the broken rubble when the maximum loads happened. The length of broken rubbles at Test 5 was obviously larger than that of Test 6. Please note that the distance between the structural wall and the circumferential crack is equal to L_f, which is a concept of two-dimensional study.
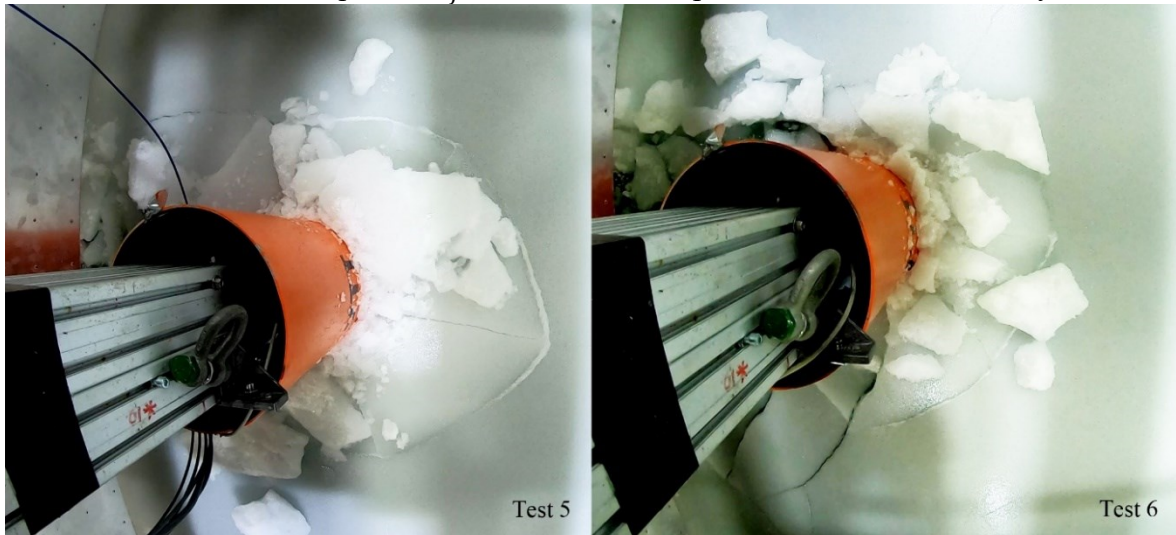
Fig. 5.8 Broken rubbles when the maximum loads happened at Test 5 & 6

5.1.3 Splitting in the level ice

The splitting was observed in the level ice in front the ridge at Test 2, 7 and 8, as shown in Fig. 5.9. The structure was vertical at Test 2 and slope at Test 7 and 8. This observation coincided with the common sense that the splitting can occur under the interaction with vertical and slope structures (Lu et al., 2015). The reason might be the connect between the level ice and ridge was too weak. It changed the front boundary condition of the level ice. When the model was close to the ridge, the size of ice sheet became not much larger than the characteristic dimension of the structure, which satisfied the condition of occurring ice splitting (Kärnä and Jochmann, 2003). The splitting reduced the force for breaking the level ice and consequently the total ice loads. This could be clearly observed from the envelope of the ice loads, as shown in red boxes in Fig. 5.10. It could be also observed that the time span of reduced ice loads was proportional to the length of splitting.
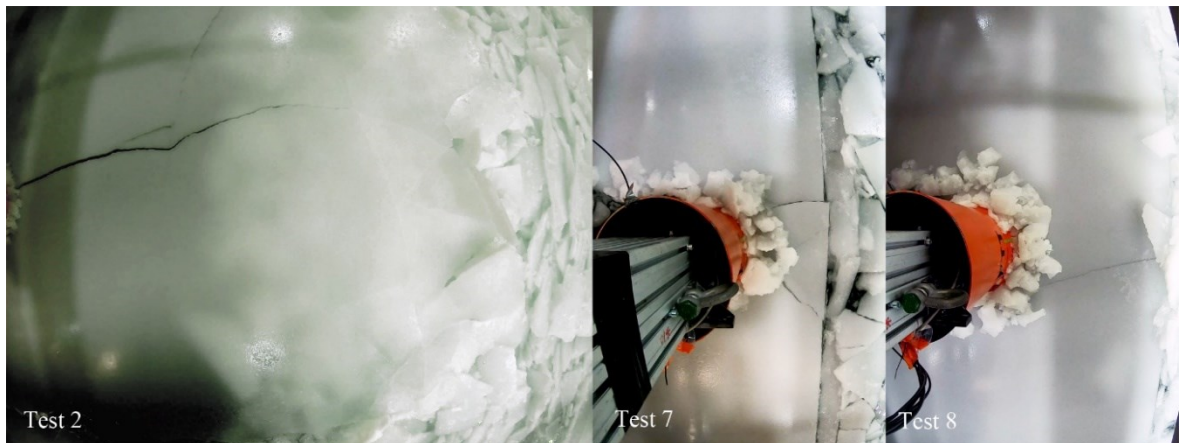
Fig. 5.9 Level ice splitting at Test 2, 7 and 8 (Vertical Structure: Test 2; Slope Structure: Test 7 & 8)
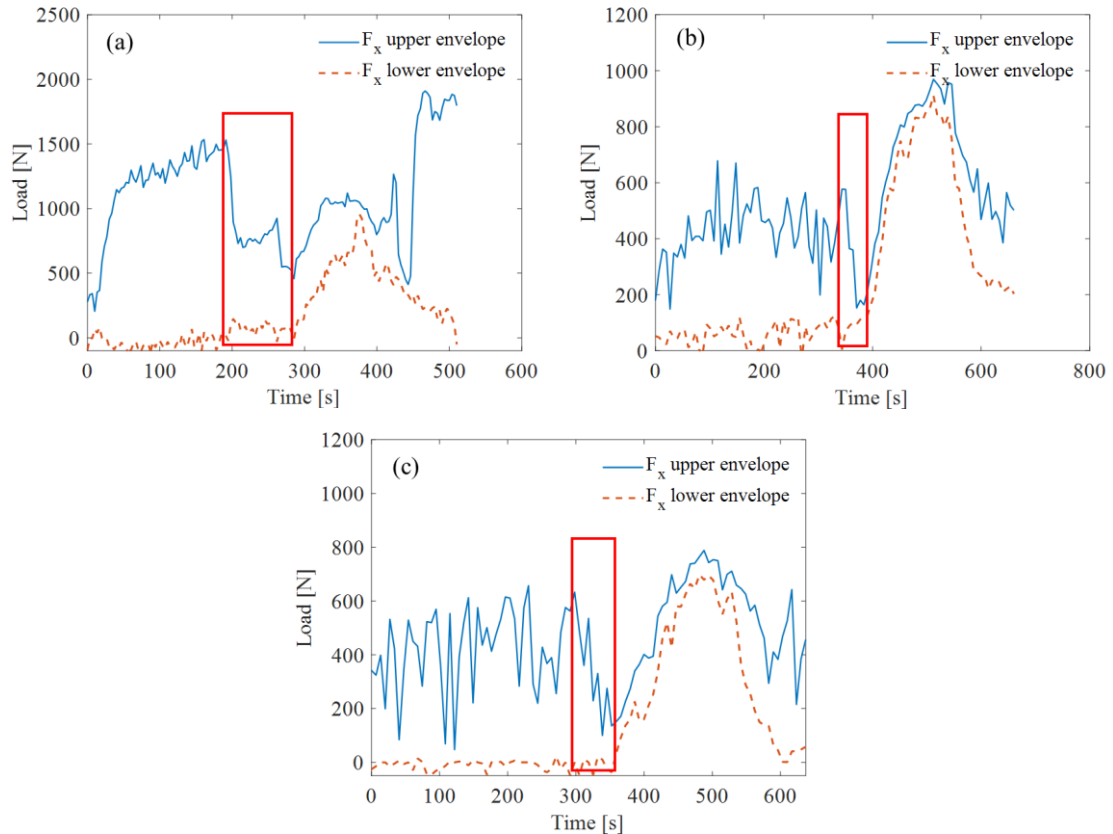
Fig. 5.10 Ice loads reduction due to splitting: (a) Test 2 (Vertical Structure), (b) Test 7 (Slope Structure), (c) Test 8 (Slope Structure)

5.1.4 Frequency domain analysis

The Fast Fourier Transform is helpful to study the ice loads from the aspect of frequency domain. It reveals at what frequency spectrum the energy of ice loads distributes. Thus, the designer could be aware of keeping the natural frequency of the structure out of the frequency spectrum where the ice loads concentrates to reduce the dynamic response of the structure.

Figure 4.21(d) presents the energy distribution of ice loads in X direction at frequency domain. The vertical structure had one dominating peak in the region of level ice before and after the ridge. Nevertheless, the slope structure had two dominating peaks in the same region. This was attributed to the different failure modes of ice structure interaction of vertical and slope structures. The failure mode of vertical structures was dominated by the continuous crushing. However, the slope structures have two dominating failure modes: bending and crushing. The frequency of crushing is much higher than that of bending, which is in accordance with the observation of history curve of ice loads. The magnitude of bending peaks was obviously higher than crushing peaks. This means more energy was consumed by bending. Figure 5.11 shows the frequency locations of these peaks of each test. The Test 2 only had one peak so it is denoted with distinctive black dot.
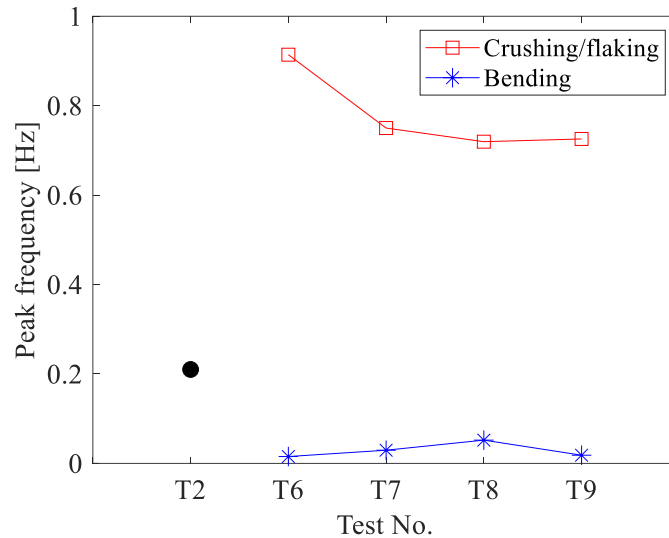
Fig. 5.11 Frequencies of the highest peaks

Test 7, 8 and 9 were all performed in the Ice sheet 3 and the structure type were all slope so their crushing peaks located at similar frequency. The peak height of Test 9 was higher than that of Test 7 and 8 because the flexural strength at Test 9 was much higher.

Figure 4.21 (e) and (f) show the energy distribution of ice loads in Y and Z direction, respectively. Generally, the amplitude of curves was lower than the curve in Fig. 4.21 (d). This reflected that the energy of ice loads was mainly consumed in X direction.

5.1.5 Distribution of level ice loads

Figure 4.23 shows the distribution of level ice loads in X direction. It shows that the structure type and flexural strength of ice could influence the spread, mean and maximum magnitude of longitudinal loads. For the vertical structure, the distribution was more scattered at Test 2 and two peaks appeared in the histogram. This was attributed to the splitting of the level ice. One peak approximately located at 700 N and the other peak approximately located at 1200 N. This agreed with the envelope of ice load in Fig. 5.10 (a). The envelope had two plateaus, which were around 700 N and 1200 N, in the part of level ice loads. For the slope structure, the distributions of Test 6, 7, 8 and 9 were similar in shape. Many loads concentrated at low magnitude and the number of loads gradually reduced along with the increase of load magnitude. According to the analysis at 5.1.1, the very large loads were induced by bending. Between two bending failures, the structure only sustained the loads induced by rubbles and structural vibration. The interval between bending failures was relatively large so the number of very large loads was small for slope structures at Test 6~9. In contrast, the number of very large loads was larger at Test 2 because the dominant failure mode was crushing/flaking, which had much smaller interval than that of bending failure. According to the analysis at 5.1.2, the broken rubble length was proportional to the load magnitude induced by bending. Due to the constant advancing speed of structure, it could be deduced that the interval between bending failures was proportional to the magnitude of bending load. Thus, the number of loads continuously decreased along with the increase of load magnitude. As a result, the tail of distribution was longest at Test 6 among Test 6~9. The spread was also influenced by the flexural strength of ice. More low-magnitude ice loads occurred when the flexural strength was large. For example, the flexural strength was largest at Test 2 and the ice loads more concentrated at low-magnitude region. As discussed above, the interval between bending failures was proportional to the magnitude of bending load. During the

interval, the ice loads were mainly induced by the broken rubbles, which were small in magnitude. Thus, the number of low-magnitude ice loads was proportional to the flexural strength of ice. As to the maximum magnitude, Test 2 and Test 6 were at the similar level around 1500N even though the flexural strength of ice was much higher at Test 6 than that of ice at Test 2. This reflected that the slope structure could reduce the maximum magnitude of level ice loads. As to the mean of ice loads, the dominant failure mode was crushing for the vertical structures and bending for the slope structures so it was understandable that the mean of ice loads was larger on vertical structures than slope structures.

Figure 4.24 shows the distribution of level ice loads in the lateral direction. It should note that all values shown in this figure are absolute values and the direction of force (port or starboard) was not considered in this analysis. The distribution was similar to the distribution of ice loads in X direction. The structure type and flexural strength of ice showed similar influence on the lateral ice loads.

Figure 4.25 shows the distribution of level ice loads in the vertical direction. The structure type and flexural strength of ice showed similar influence on the vertical ice loads. The load distribution of Test 2 had two peaks, which is similar to the load distribution in X direction. The distributions of the other four tests also had shapes similar to those in X direction. This could be explained by the close correlation between the longitudinal loads and the vertical loads.

5.1.6 Return period of level ice loads

Figure 4.29 shows the return period of level ice loads in X direction. According to the shape, the curves could be divided into three groups. The curve of Test 2 had a shape of Γ. The curves of Test 6 and 9 had a shape of S. The curves of Test 7 and 8 were close to straight lines. The structure type at Test 2 was vertical so there were many large ice loads with short return period. As a result, the curve of return period rapidly climbed up to a high level of load magnitude. As to Test 6~9, the structure types were slope. The slope can reduce the ice loads in magnitude. Therefore, the curve did not rise up with an angle as high as Test 2, especially at the initial stage. The difference in shape between the Test 7/8 and Test 6/9 was attributed to the flexural strength of level ice. If the strength of ice was weak, the distribution of ice loads would be more scatted. Thus, the return period curve would smoothly rise up. The curves of Test 7 and 8 were very close because the level ice had same thickness and flexural strength at these two tests.

Figure 4.30 shows the return period of level ice loads in Y direction. The curve of Test 2 was higher than any other test. This means the ice loads were higher on the vertical structure at the same return period. The curve of Test 6 crossed the curve of Test 9 at the return period of 1 s. This might be caused by the difference in thickness and flexural strength but more investigation should be performed to reveal the mechanism.

Figure 4.31 show the return period of level ice loads in Z direction. All curves had shapes similar to their peers in X direction. This displayed the correlation between the ice loads in X direction and Z direction again. However, the curve of Test 2 was not as high as that in X direction. The structure was vertical at Test 2 but the structure type was slope at the other tests. The vertical components of ice loads were smaller at Test 2. Thus, the number of large loads and the magnitude of largest load would be smaller. This reflected to the return period curve is that the loads had larger return period when its magnitude reached a threshold, which was approximately 200 N between Test 2 and Test 6.

5.2 Ice ridge

Totally, eight testes were carried out within three ice sheets and relevant ice ridges, as shown in Table 4.1. The structure fully cut through the ridges in six of the eight tests. At Test 1 and Test 10, the structure could not fully cut through the ridges due to too large ice loads. The structure stopped in order to protect the testing facility and structure when the structure touched the level ice after the ridge. It should note that the ridge was built by using the level ice to push and squeeze floating ice rubbles so some rubbles moved under the level ice sheet. Consequently, there was a belt type of overlap formed of the level ice and keel rubbles at the margin of ice sheet. The width of the overlapping belt was approximately 0.5 m. In the experiment, the level ice was stronger than the consolidated layer so larger loads could be generated by the level ice and keel rubbles. In addition, the structure type is vertical cylinder at Tests 1 and 10 so the level ice was broken by crushing so the vertical structure suffered larger level ice loads than the slope structure.

The ridge loads are normally considered consisting of two parts: 1) loads induced by the consolidated layer; 2) loads induced by the keel rubbles. In order to study the structure-ice interaction in pure keel rubbles and the influence of consolidated layer, the tests were divided into two groups. Test 1, 5, 6, 9 and 10 were carried out after the consolidating procedure so the ridges had consolidated layer. In contrast, Test 2, 7 and 8 were performed in ridges without consolidated layer before the consolidating procedure.

5.2.1 Structure type

Figure 5.12 presents the history curve of ridge loads at Test 9 and 10, which represents ice interaction with the slope structure and vertical structure, respectively. In Fig. 5.12 (a), there was no the typical 3 stage procedure of bending failure even though the bending failure mode could be observed at Test 9. Nevertheless, the amplitude of high frequency oscillation was smaller than that in Fig. 5.12 (b). The high frequency oscillation has approximately same period, which means it could be induced by the consolidated layer but not the keel. The keel consists of rubbles with random size so the period should be random if the high frequency oscillation was induced by the keel. Thus, smaller amplitude of high frequency oscillation could reflect that the slope structure was able to reduce the loads for breaking the consolidated layer. Figure 4.19 also shows that the maximum load for breaking the consolidated layer at Test 9 is much smaller than that at Test 10. However, the maximum rubble loads of the ten tests did not fluctuate much as shown in Fig. 4.19. This might reflect that the effect of structure type was not strong on the rubble loads. It is reasonable because the conical part is short compared to the total length of the structure and the depth of rubble accumulation.

Even though the bending failure mode could not be obviously observed in the ridge, the slope structure could also reduce the loads induced by the consolidated layer. The fail of Test 1 and 10 could proof this hypothesis. Test 1 and 10 failed due to large loads and the structural type was vertical at these two tests. In contrast, all other tests with slope structure successfully completed the tests.
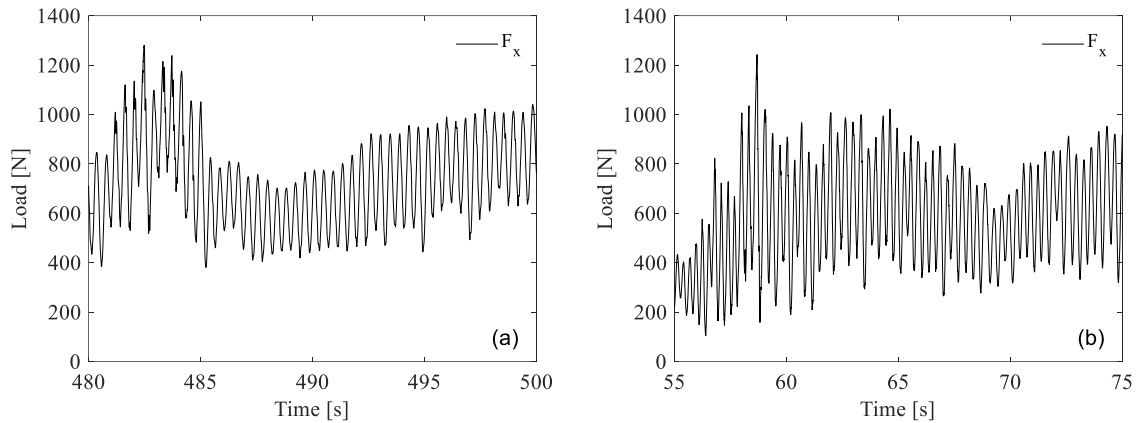
Fig. 5.12 History curve of ridge loads; (a) Test 9 (Slope Structure), (b) Test 10 (Vertical Structure)

5.2.2 Consolidating procedure

As shown in Fig. 5.13, the fluctuation of force history curve is much smaller during tests without consolidated layer (Test 2, 7 & 8) than the tests with consolidated layer (Test 1, 5, 6, 9 & 10). The reason of small fluctuation in ridges without consolidated layer could be induced by breaking the freeze bond between rubbles. Furthermore, the amplitude of fluctuation has a close and positive relationship with the flexural strength of consolidated layer. For example, the structure type was slope at Test 7, 8 and 9 and the fluctuation amplitude was larger (around 500 N) at Test 9 than the amplitude (less than 100 N) at Test 7 and 8. The bending failure mode is more obvious at Test 9 too because the loads induced by consolidated layer were larger due to stronger flexural strength. This could be verified by the load curves in the overlapping belt. When the structure cut through the overlapping belt, it broke stronger level ice so the fluctuation amplitude became larger and the failure mode was increasingly close to the failure mode of level ice as the influence of keel reduced along with the clearing of rubble accumulation. Figure 4.14~16 show that the largest rubble loads (lower envelope) were approximately 900 N, 700 N and 800 N at Test 7, 8 and 9, respectively. Thus, the consolidating procedure did not show a clear influence on the rubble loads. However, the largest total ridge load was around 1600 N at Test 9, which was much larger than the largest ridge loads at Test 7 and 8, as shown in Fig. 5.13. Therefore, it could be deduced that the consolidating procedure could increase the ridge loads by increasing the loads for breaking the consolidated layer.
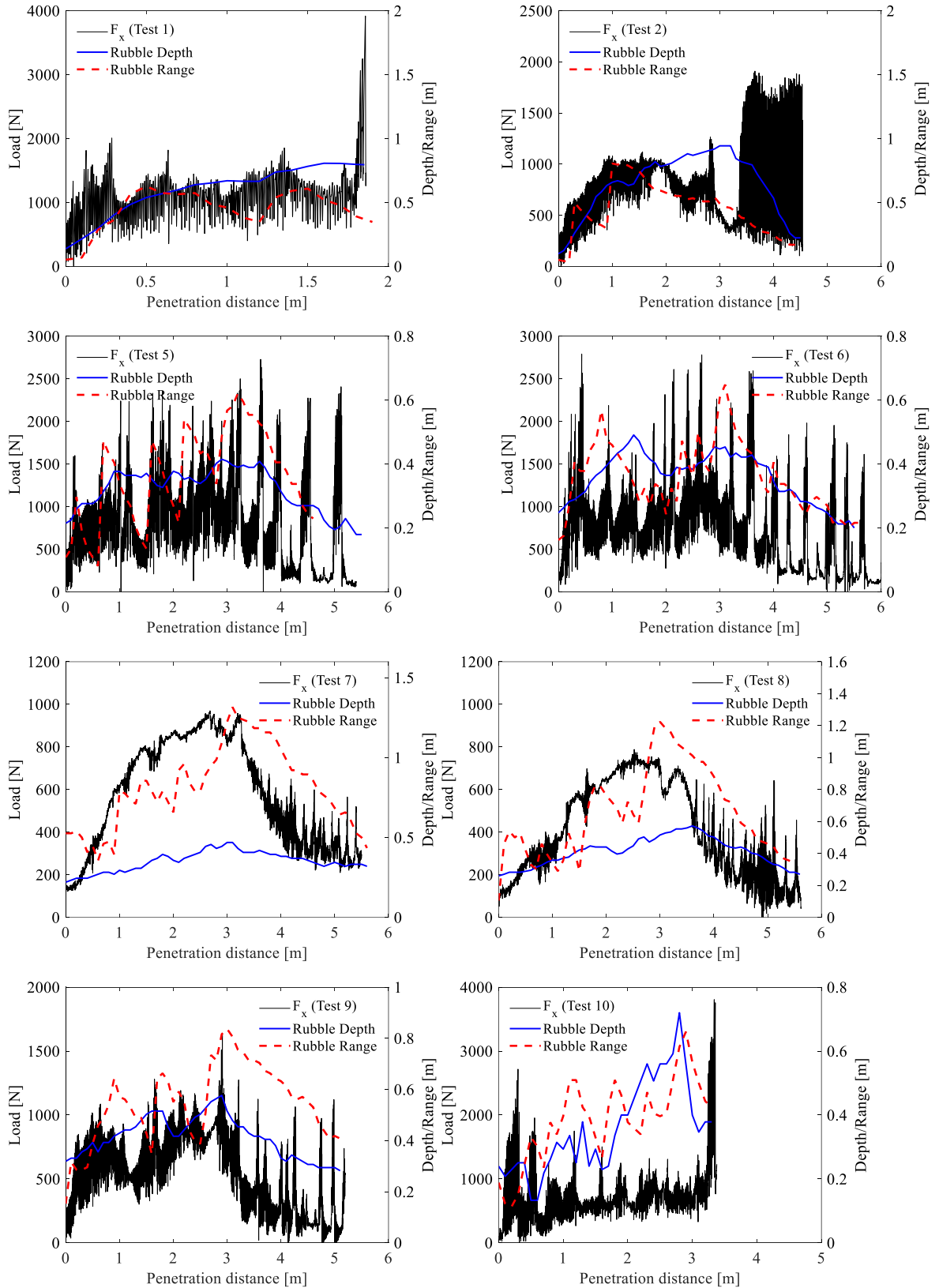
Fig. 5.13 History curve of ridge loads, keel profile, rubble depth and rubble range

5.2.3 Rubble accumulation

The load induced by keel rubbles could have a relationship with the amount of rubbles accumulated in front of the structure. According to the observation via the underwater camera, the longitudinal central section of the rubble accumulation can be roughly considered triangle. One example is shown in Fig. 5.14.
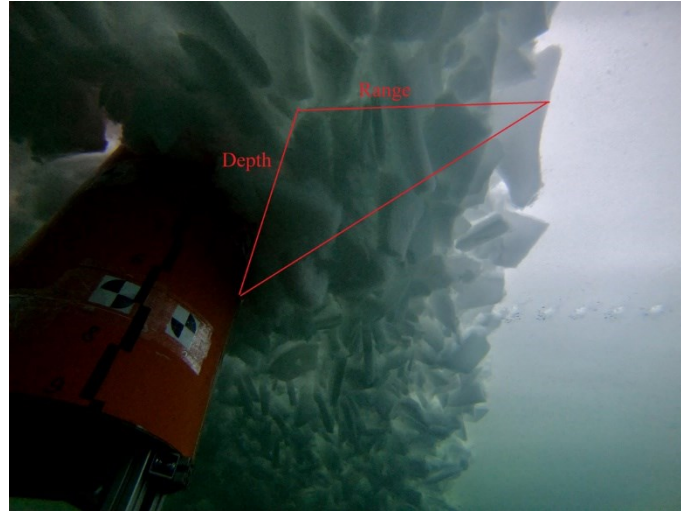
Fig. 5.14 Rubble accumulation in front of the structure

Therefore, two parameters are employed to represent the variation of rubble volume accumulated in front of the structure. One parameter is the maximum depth of the rubble accumulation and the other is the maximum horizontal range of rubbles moving along with the structure, as shown in Fig. 5.14.
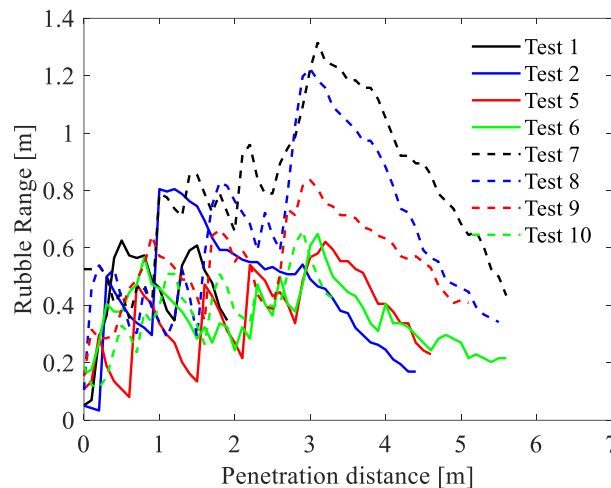
Fig. 5.15 Horizontal moving rubble range in front of the structure (Vertical Structure: Test 1,2 & 10; Slope Structure: Test 5~9)

Figure 5.15 shows the maximum horizontal range of moving rubble against the penetration distance of the structure. In most cases, the largest peaks located at 3 m of penetration distance. The total width of ridge is 4 m for ice ridge 2 and 3 so the range of moving rubbles reached its highest value at around 75% ice ridge width. However, it should note that it is not clear this highest value was connected to the ice ridge width or the diameter of the column type structure. One exception is Test 2. At Test 2, the highest range of moving rubbles located at around 1.2 m penetration distance. At Test 1 and 10, the structure did not

fully penetrate the ice ridge so the data could not clearly show the highest range. At the ascending stage before the summit, the curves rose up with a zigzag pattern. When the structure contacted the keel, the contacting force firstly broke the freeze bond between rubbles and pushed the rubbles to move forward but the force was consumed so it was continuously reduced along with the enlarging distance. As a result, the moving rubbles had a specific range. On the boundary of moving range, the contacting fore was less than the freeze bond. This was the situation on the left side of a tooth in the moving rubble range curve. On the right side, the structure continuously pushed the rubbles to reduce the porosity between rubbles. The range shrank and the contacting force rose up until the contacting force became large enough to break the freeze bond out of the boundary. At this time, the range of moving rubbles turned into expansion and another round started. The expanding speed depends on the size of rubbles and the magnitude of freeze bond.
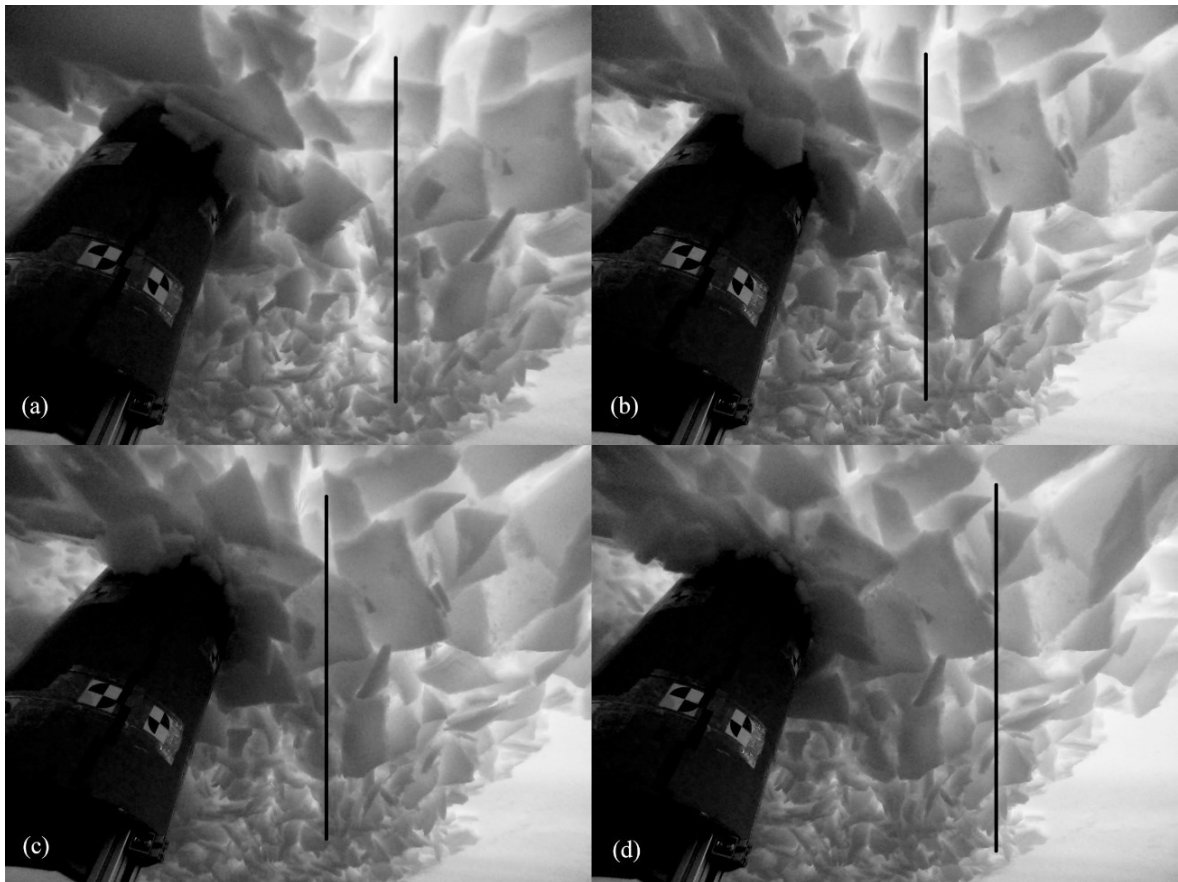
Fig. 5.16 Shrinkage and expansion of maximum moving rubble range at Test 5 (Slope Structure), penetration distance is 1.6 m (a), 1.8 m (b), 2.1 m (c) and 2.2 m (d).

Figure 5.16 presents an example of the whole procedure of range shrinkage and expansion. The straight lines point out the range of moving rubbles at each penetration distance. When the range reached the opposite boundary of the keel, its magnitude also rose up to the maximum in most cases. After this point, the value of range continuously decreased due to the clearing of rubbles. At the descending stage, all freeze bond between rubble was broken and the structure only needed to push the rubbles forward so the curves were smoother than those at the ascending stage.
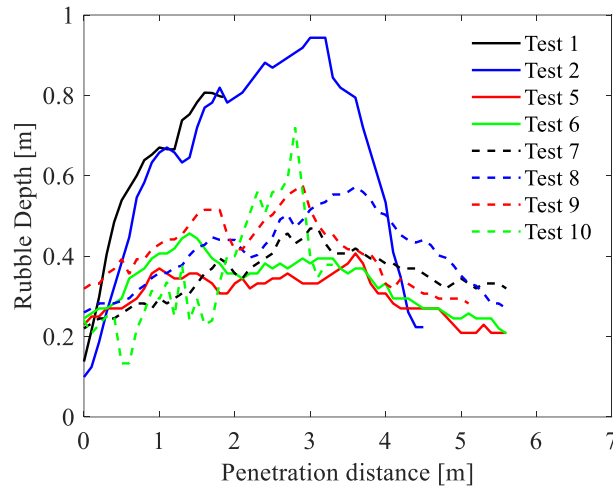
Fig. 5.17 Maximum depth of rubble accumulation in front of the structure (Vertical Structure: Test 1,2 & 10; Slope Structure: Test 5~9)

Figure 5.17 shows the maximum depth of rubbles accumulating in front of the structure. The summits of most cases located at the second half of the keel, approximately after 3 m penetration distance. However, the curve of Test 6 had a summit at around 1.5 m penetration distance. Test 1 did not finish penetrating the whole keel and the width of the keel was approximately 2 m wide so its summit location could not be observed during the test. The first half of curves rose up to the summit with severer fluctuation. It was attributed to combining effect of rubble accumulation and clearing. Generally, the accumulation dominated the variation of rubble depth but the clearing might exceed the accumulation sometimes. As a consequence, the rubble depth decreased and resulted in a dent at the curve of rubble depth. After the summit, the rubble depth was only influenced by the rubble clearing so the curves were smoother.

As shown in Fig. 5.14, the longitudinal central section of rubble accumulation was triangle in geometry according the observation. Therefore, the area of the section A is employed to represent the amount of accumulation

$$A = D \times R \qquad (5.3)$$

where D denotes the rubble depth and R denotes the maximum range of rubble. Thus, the area of the section A could reflect the influence of depth and range on the rubble loads together.

Figure 5.18 shows the lower envelop of ridge loads and area of section A of Test 1 ~ 10. It was clear that the trend of load curve fairly matched the trend of section area curve for each case. For example, the summit of two kinds of curves had close location at X axis. Gong et al. (2019) report a discrete element simulation to predict resistance of a ship in unconsolidated ridges. According to their research, the deformation force maintains a constant maximum value when the ship bow fully enters the ridge and the deformation force is proportional to the volume of mass of ice rubbles moved by the ship. Our observation matches their discovery. The rubble area curves also showed that the rubble accumulation was larger at the tests with unconsolidated keel. In ice sheet 2, the curve of Test 2 was generally higher than the curves of Test 5 and 6. In ice sheet 3, the curves of Test 7 and 8 were generally higher than the curves of Test 9 and 10. This could be attributed to the difference of freeze bond strength in different cases. In the ridge with consolidated layer, the freeze bond between rubbles was stronger than that of ridge without consolidated layer so

the structure could move fewer ice rubbles by breaking their freeze bond. As a result, the rubble accumulation was smaller. It should note that the lower envelope underestimated the loads induced by the keel because of the structure's vibration. The underestimation might be larger if the vibration was stronger. Thus, the tests in ridge with consolidated layer were more underestimated than the tests in ridge without consolidated layer. Therefore, the curves could not be applied for comparing the keel loads between various cases.
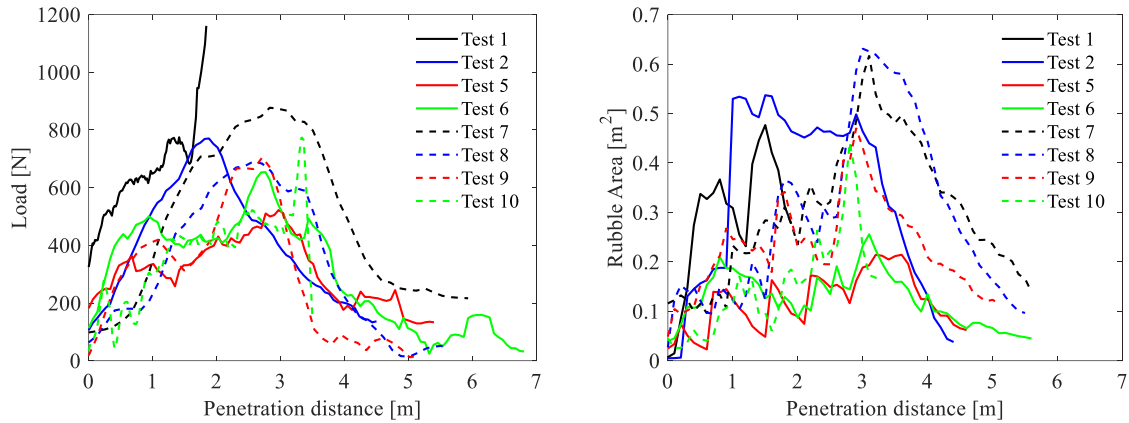
Fig. 5.18 Lower envelope of ridge loads and longitudinal central section area (Vertical Structure: Test 1,2 & 10; Slope Structure: Test 5~9)

5.2.4 Distribution of ridge loads

Figure 4.26 shows the distribution of ice ridge loads in X direction. It is shown that the distribution is more scattered with multiple peaks at Test 2, 7 and 8. This phenomenon could be attributed to the effect of consolidating procedure of the ridge because all the three tests were conducted before the consolidating procedure. After the consolidating procedure, the freeze bond forms between ice rubbles. The rubbles were more stable and connected together before broken by the structure. Thus, the volume of rubbles scattered by the structure was more stable in front of the structure. In contrast, the rubbles were not evenly capable of holding position in front of the structure because they were not connected by the freeze bond. Some rubbles were easy to move and some rubbles were stable because they were confined by neighboring rubbles and not so easy to move. Thus, the volume of scattered rubbles was scattered and this resulted in more scattered loads distribution. The volume variation could be verified by the measurement of rubble area as shown in Fig. 5.16. For ice sheet 3, the curve of Test 7 and 8 varies approximately from 0.05 to 0.63. This is much larger than the variation of Test 9 and 10, which approximately ranged from 0.05 to 0.47 and from 0.025 to 0.44, respectively. The loads of Test 7 and 8 was more scattered than Test 9 and 10. For ice sheet 2, the range of Test 2 was approximately from 0 to 0.54 and the range of Test 5 and 6 was approximately from 0.03 to 0.21 and from 0.05 to 0.25, respectively. The loads of Test 2 were more scattered than Test 5 and 6.

The existence of freeze bond also had a positive relationship with the distribution of ice ridge loads. If the tests were performed after the consolidating procedure, more larger loads could be measured during the tests. The summit of the distribution located at larger load. The maximum value of ice loads could be larger. More ice loads were distributed on the right side of the summit. For example, the summits of Test 5 & 6 approximately located at 1000 N and the summits of Test 7 & 8 approximately located at 800 N. Around 50% loads located on the right side of the summits at Test 5 & 6 and most loads located on the left side of the

summits at Test 7 & 8. The maximum loads were over 2500 N at Test 5 & 6 and the maximum loads were under 1000 N at Test 7 & 8.

The influence of structure type was not strong on the ice loads distribution. For example, the structure types at Test 9 & 10 were slope and vertical, respectively. They all performed after the consolidated procedure. The summits of these two tests all located around 800 N and the percentages are also similar on both sides of the summits. This could be attributed to the scheme of the structure. At Test 9, the slope part was only 200 mm in depth and the other part was vertical cylinder below 200 mm depth. In addition, the rubble depth was much larger than 200 mm, as shown in Fig. 5.15. Therefore, the structure type could mainly influence the breaking of level ice and consolidated layer but the influence was not so much on the breaking of ridge keel. This could be verified by the largest loads at Test 9 & 10, which were induced by breaking the level ice overlapping the ridge. As shown in Fig. 4.26, the maximum load was much larger at Test 10 than that at Test 9.

Figure 4.27 shows the distribution of ice ridge loads in the lateral direction. It should note that all values shown in this figure are absolute values and the direction of force (left or right) was not considered in this analysis.

Firstly, the influence of the freeze bond was not clear on the degree of scatter of the distribution. For example, the shape of histogram of Test 1 was similar to that of Test 2 although Test 1 was performed after the consolidating procedure and Test 2 was performed before the consolidating procedure. However, the freeze bond could generate larger loads. It is shown that the number of loads over 100 N at Test 7 & 8 was much less than that of Test 9. In addition, the maximum load was much large at Test 9.

The influence of structure type was obvious on the distribution of the loads in Y direction. For example, the summit location and maximum loads at Test 10 were larger than those at Test 9 although these two tests had similar histogram shape. This could be attributed to the location of contacting line between the structure and consolidated layer / level ice. The contacting line was not always symmetrical to the X axis so the magnitude of lateral component depended on the asymmetry and the magnitude of loads for breaking the ice. The probability distribution of asymmetry was assumed equivalent and the vertical structure needed larger force to break the consolidated layer / level ice so more loads were distributed in the zone of larger value.

Figure 4.28 presents the distribution of ice ridge loads in vertical direction. All values shown in this figure are absolute values and the direction of force (upward or downward) was ignored by this analysis.

The influence of freeze bond on vertical loads had a close relationship with the loads in X direction because the vertical force and longitudinal force were the two components of ice loads. The vertical force was directly proportional to the longitudinal force. For example, the distribution of Test 1 horizontally moved to the right compared to the distribution of Test 2. The situation was similar to that of the loads in X direction.

The slope structure suffered larger vertical force from the ice due to the slop side. The summits of distribution of slope structure located at larger loads and more loads distributed on the right side of the summits, comparing to the vertical structure. This phenomenon was more apparent for the tests performed after the consolidating procedure. For these tests, the ridges had consolidated layer, which mainly contacted the slop and nearly all the force loaded on the slop side and generated large vertical component of the force. The comparison between Test 7 & 8 and Test 9 clearly shows this phenomenon.

5.2.5 Return period of ridge loads

Figure 4.32 shows the return period of ice ridge loads in X direction. The left figure shows that the curves of Test 5 & 6 are higher than the curve of Test 2 even though the structure type was vertical at Test 2 and slop at Test 5 & 6. Test 5 & 6 were conducted after the consolidating procedure so the freeze bond in between rubbles was larger and, as a consequence, the ice loads on the structure were larger. The same phenomenon happened at Test 7 & 8 and Test 9. Test 9 was carried out after the consolidating procedure and had stronger freeze bond in the keel so the ice loads were larger on the structure.

The curves of Test 9 and Test 10 are initially close and depart after 2 s return period. At the adjacent part, it was considered the loads were induced by the keel. The keel was deep in water and the slop part of structure was only 200 mm in depth so the keel contacted same vertical structure at Test 9 and Test 10. Thus, it was reasonable that the loads induced by the keel rubble were similar in both tests. At the departing part, the loads were induced by the consolidated layer or the level ice. The consolidated layer and level ice floating on the surface so they mainly contacted the slop part at Test 9. Consequently, the ice loads were much less than those at Test 10.

Fig. 5.19 Illustration of rubble size at Test 5 (a & b) and Test 6 (c & d)

Figure 4.33 shows the return period of lateral ice ridge loads. It was understandable that the curve of Test 2 is lower than the curves of Test 5 and Test 6 due to stronger freeze bond. However, it is interesting that the divergence is so large between the curves of Test 5 and that of Test 6 even though the type of structure were both slop in these two tests and they were all conducted after the consolidating procedure of ice sheet 2. The divergence was attributed to the difference in the size of ice rubbles that formed the ridge. During Test 5, the

structure encountered more large ice rubbles. This resulted in more large lateral ice loads. One example is illustrated in the Fig. 5.19. The lateral force mainly derived from two sources: 1) the unsymmetrical interaction between the structure and consolidated layer; 2) the unsymmetrical clearing of accumulated rubbles. For the first source, the structure often broke the consolidated layer in between rubbles because the freeze bond, connecting the rubbles, were weaker than the strength of rubbles. Large rubbles had large acting area of freeze bond and consequently induced large reacting forces. For the second source, the volume of accumulated rubbles changed when a rubble cleared away from the structure. Large rubbles meant large volume change and consequently induce large lateral forces.

The difference of freeze bond could also explain the difference of lateral loads at Test 7, 8 9 and 10. Stronger freeze bond in the ridge of Test 9 and 10 induced larger lateral force on structures. The large divergence between the curves of Test 9 and Test 10 was attributed to the different failure modes of consolidated layer due to different structure types. The structure type was vertical at Test 10. Thus, it was reasonable that the failure mode was mainly crushing and resulted in larger loads if we considered the Test 9 and Test 10 had the same probability of unsymmetrical breaking.

Figure 4.34 shows the return period of vertical ice ridge loads. It was understandable that the slope structures at Test5 & 6 bore larger vertical loads. In addition, the Test 5 & 6 were conducted after the consolidating procedure and experienced stronger freeze bond. The same reason could be utilized to explain the difference between Test 7 & 8 and Test 9.

The vertical force on Test 10 surpasses the force on Test 9 when the curve was beyond 4 s return period. This was in compliance with the curves of loads in X direction, as shown in Fig. 4.32. It is shown that the two curves of Test 9 and Test 10 were close before 4 s return period in Fig. 4.32. The slop side generated a large vertical component of loads at Test 9. Thus, the curve of Test 9 was much higher than the curve of Test 10 in Fig. 4.34. After 4 s return period in Fig. 4.32, the curve of Test 10 is obviously higher than the curve of Test 9. The large ice loads induced large deformation of the structure and tilt angle. Thus, the vertical component of the force could be large.

5.2.6 Frequency domain analysis

Figure 4.21 (a)~(c) show the Fourier transform of ridge loads in X, Y and Z direction, respectively. The amplitude of ice loads is much larger in X direction. This means the energy was mainly transmitted to structures through the loads in X direction. If the rubble loads were assumed constant, they had infinitely small frequency. Therefore, the energy generated by the rubble loads could not be presented by using the Fourier transform. As a result, the curves only reflect the energy generated by the consolidated layer. There was no consolidated layer at Test 2, 7 and 8 because the tests were performed before the consolidating procedure. Thus, the curves at these three tests should be much lower, which was correctly presented in the Fig. (a)~(c). Most curves had multiple peaks and these peaks randomly distributed along the frequency. This might reflect that the rubbles intensively affected the breaking of consolidated layer.

6 Conclusions

The experiment was conducted in the Aalto Ice Tank to study the ice loads on cylindrical and conical structures. Eight tests were successfully performed by running the model through three ice sheets with an embedded ridge. These three ice sheets had constant thicknesses, ranging from 0.04m to 0.043m, and various flexural strength. The value of flexural strength and ice thickness were chosen to represent designed ice condition around lighthouse Nordströmsgrund locating in the north Baltic sea, which is also the prototype of the vertical structure model. The model was fixed on the carriage and towed to run through the ice. It consisted of conical part and cylindrical part. Eight tests were successfully conducted. At each test, only one part was utilized to investigate the properties of interaction between the ice and vertical/slope structures. The ice loads on structures were measured and recorded as three components in three directions according to the Cartesian coordinates.

Based on the investigation of the ice loads measurements and the breaking process of level ice and ridge, the following conclusions could be proposed:

Interaction between level ice and structures
(1) For the vertical structure, the high frequency oscillation dominated the history curve of ice loads induced by flaking. For the slope structure, the low frequency oscillation dominated the history curve of ice loads induced by bending. The low frequency oscillation consisted of three stages: 1) load accumulation, 2) load dropping, and 3) oscillation induced by the structure vibration. The accumulated rubbles could help the slope structure bend the level ice with their buoyancy and their contribution was proportional to their volume.

According to the frequency domain analysis, the energy spectrum of vertical structure had one peak and the energy spectrum of slope structure had two peaks. This reflected to the failure modes of vertical and slope structures: the vertical structure had crushing failure mode and the slope structure had bending and crushing modes. The frequency of bending was much lower than that of crushing so the energy concentrated at two regions.

(2) The ice loads were dominated by breaking the level ice and the accumulated rubbles made a small contribution to the total ice loads. However, the accumulated rubbles' contribution increased when the structure totally penetrated the ridge because the structure carried considerable rubbles from the keel.

For the slope structure, the measured maximum ice loads had a large deviation in magnitude, which were induced by the complex interaction process. The value of peak ice loads was proportional to the distance between the structure and the circumferential crack.

(3) The structure type and flexural strength of level ice was able to influence the spread, mean and maximum magnitude of level ice loads. The ice loads on vertical structure was more scattered than those on the slope structures. For the slope structure, the degree of scatter of ice loads was inversely proportional to the flexural strength of ice. The ice loads in the direction of structure movement had stronger correlation with the loads in the vertical direction than the loads in the lateral direction.

(4) The ISO model and Ralston's model overestimated the total ice loads in most cases. The Ralston's model overestimated the rubble loads in the region before the ridge but underestimated the rubble loads in the region after the ridge. That was because the

structure carried considerable amount of rubbles from the ridge when it just penetrated through the ridge.

Interaction between ice ridge and structures

(1) The slope structure reduced the ice loads induced by the consolidated layer even though the bending failure mode was not as apparent as that in the level ice. The reason was the rubble accumulation could assist the structure in bending the consolidated layer. The bending failure mode was more obvious if the consolidated layer was stronger after the consolidating procedure.

(2) The rubble loads were proportional to the volume of accumulated rubbles, which could be represented by the horizontal range of rubble moved by the structure and the depth of rubble accumulation. The summit of horizontal range usually appeared accompanying with the summit of rubble accumulation volume. The curve of horizontal range had a zigzag pattern before its summit. The zigzag reflected the pattern of breaking freeze bond between rubbles in the keel. The depth was influenced by the accumulating and clearing of rubbles before the summit of volume. However, it was only influenced by the clearing after the summit.

(3) The consolidating procedure could reduce the spread of ridge loads in the longitudinal and vertical directions. However, the influence was not obvious on the lateral loads. The consolidating procedure increased the mean of ice loads by resulting in more large loads. The influence of structure type was weak on the spread of longitudinal ice loads but strong on that of lateral and vertical loads. The lateral ice loads on vertical structures were more distributed in the zone of large value than the slope structures. The vertical ice loads on slope structures were more distributed in the zone of large value than the vertical structures.

(4) The magnitude of lateral ice loads was proportional to the size of rubbles in the ridge. The magnitude of lateral ice loads was potentially proportional to the strength of freeze bond because more large loads were measured when the test was conducted after the consolidating procedure.

References

Aly, M. 2018. Analysis of scale effect in ice flexural strength. Mater thesis, Memorial University of Newfoundland.

Ashton, G.D., 1989. Thin Ice Growth. Journal of Water Resources Research. Vol. 25, No. 3. pp.564–566

Barker, A., et al. (2005). "Ice loading on Danish wind turbines: part 1: dynamic model tests." Cold Regions Science and Technology 41(1): 1-23

Claude Gerard Daley, 1991. Ice Edge Contact - A Brittle Failure Process Model. Doctoral thesis, Helsinki University of Technology.

Cox, G. F., Weeks, W. F., 1983. Equations for determining the gas and brine volumes in sea ice samples. Journal of Glaciology (Vol. 29, No. 102), 306-316.

Cox, G.F.N. & Weeks, W.F. Salinity variations in sea ice. Journal of Glaciology, Vol. 13(67), 1974.

Croasdale, K.R. (1980): "Some implications of ice ridges and rubble fields on the design of Arctic Offshore Structures", Proc. Nat. Res. Council of Canada Workshop on Sea Ice Ridging, Calgary, Technical Memo 134, pp. 157-180, NRC of Canada, Ottawa, Canada

D. S. Sodhi and H. E. Hamza, 1977. Buckling analysis of a semi-infinite ice sheet, Proceedings of Fourth International Conference on Port and Ocean Engineering under Arctic Conditions (POAC '77), Memorial University of Newfoundland, Canada, 26-30 September, 1977, pp. 593-604.

Daley, C., Tuhkuri, J., and Riska, K. 1998. The role of discrete failures in local ice loads. Cold Regions Science and Technology, 27: 197-211.

Dolgopolov, Y., Afanasiev, V., Korenkov, V., Panfilov, D., 1975. Effect of hummocked ice on the piers of marine hydraulic structures. In: Proc. of the 3 Int. Symp. on Ice (IAHR), Hanover, USA. 469-477.

Ervik, A., Nord, T.S., Høyland, K. V.,, Samardzija, I. & Li, H.T. 2019. Ice-ridge interactions with the Norströmsgrund lighthouse: Global forces and interaction modes. Cold Regions Science and Technology (158), 195-220.

Ettema, R., Urroz-Aguirre, G. E., 1989. Friction and cohesion in ice rubble reviewed. Cold Regions Engineering (12), 317-326.

Fernandes, A.C., and Kroff, S.A.B., Bi-linear Modelling of Wider, Longer and Continuous Bilge-keels for FPSOs Roll Motion Control, paper no. OFT-4072, Proc. ETCE/OMAE2000 Joint Conference, New Orleans, 2000.

Gagnon R, Bugden A. 2007 Ice crushing tests using a modified novel apparatus. In Proc. Port and Ocean Engineering under Arctic Conditions, POAC-07, Dalian, China, pp. 235–244.

Gagnon R. 1994 Generation of melt during crushing experiments of freshwater ice. Cold Reg. Sci. Technol. 22, 385–398.

Gagnon R. 1998 Analysis of visual data from medium scale indentation experiments at Hobson's Choice Ice Island. Cold Reg. Sci. Technol. 28, 45–58.

Gong, H., Polojärvi, A., & Tuhkuri, J. (2019). Discrete element simulation of the resistance of a ship in unconsolidated ridges. Cold Regions Science and Technology, 167, 102855.

Gow, A.J & Tucker, W.B. 1991. Physical and Dynamic Properties of Sea Ice in the Polar Oceans. U.S. Army Corps of Engineers, Cold Regions Research and Engineering Laboratory (CRREL), Monograph 91-1. 46 p.

Han, H., et al. (2015). "Flexural strength and effective modulus of large columnar-grained freshwater ice." Journal of cold regions engineering 30(2): 04015005.

Han, H., Li, Z., Huang, W., Lu, P., & Lei, R. (2015). The uniaxial compressive strength of the Arctic summer sea ice. Acta oceanologica sinica, 34(1), 129-136.

Hendrikse, H. and Metrikine, A., 2016. Ice-induced vibrations and ice buckling. Cold Regions Science and Technology, 131, 129-141.

Hetényi, M. (1946). Beams on elastic foundation: Theory with applications in the fields of civil and mechanical engineering. Ann Arbor: The University of Michigan Press.

Hottinger Baldwin Messtechnik GmbH. Production description booklet. www.hbm.com

Høyland, K. V., 2002. Consolidation of first-year sea ice ridges. Journal of Geophysical Research 107 (C6, 10.1029/2000JC000526), 15,1-15,15.

Høyland, K. V., 2007. Morphology and small-scale strength of ridges in the North-western Barents Sea. Cold Regions Science and Technology (48), 169-187.

Høyland, K.V. Lecture note of Arctic Marine Measurement Techniques, Operations and Transport, Module I Sea Ice and Icebergs, Longyearbyen, 2019.

Huse, E., and Matsumoto, K., Viscous Damping of Floating Production Vessels Moored at Sea, Proc. Offshore Mechanics and Arctic Engineering Conference, The Hague, March 1989.

ITTC – Recommended Procedures (7.5-02-04-02), Test Methods for Model Ice Properties. R02, 2014.

Jalonen, R. & Ilves, L.: Experience with a Chemically-Doped Fine-Grained Model Ice. IAHR Ice Symposium 1990, Volume 2, Espoo, Finland, August 20-23, 1990.

Joensuu A. and Riska, K., "Jään ja rakenteen välinen kosketus" (Contact between Ice and a Structure) Helsinki University of Technology, Laboratory of Naval Architecture and Marine Engineering, Report M-88, 1989 (in Finnish).

Jordaan, Ian J., 2001. Mechanics of ice-structure interaction. Engineering Fracture Mechanics, 68, 1923-1960.

Kankaanpää, P., 1998. Distribution, morphology and structure of sea ice pressure ridges in the baltic. Ph.D. thesis, Helsinki University, 100 p.

Kärnä, T. and P. Jochmann (2003). Field observations on ice failure modes. Proceedings of the 17th International Conference on Port and Ocean Engineering under Arctic Conditions, Trondheim, Norway, June.

Kärna, T., Nykänen, E., 2004. An approach for ridge load determination in probabilistic design. In: Proc. of the 17th Int. Symp. on Ice (IAHR), St.Peterburg, Russia. 2: pp. 42-50.

Karulina, M., et al. (2019). "Full-scale flexural strength of sea ice and freshwater ice in Spitsbergen Fjords and North-West Barents Sea." Applied Ocean Research 90: 101853.

Kerr, A.D., 1978. On the determination of horizontal forces a floating ice plate exerts on a structure. Journal of Glaciology, 20(82), 123-134.

Langhaar, H. (1951). Dimensional analysis and theory of models. John Wiley and sons. 166 p.

Larsen, K., and Huse, E., Practical Procedures for Estimation of Viscous Scale Effects in Model Testing of Floating Structures, Proc. 3rd Intl. Offshore and Polar Engineering Conference, Singapore, Vol. III, pp. 677-685, 1993.

Leppäranta, M., Hakala, R., 1992. The structure and strength of first-year ridges in the Baltic Sea. Cold Regions Science and Technology (20), 295-311.

Leppäranta, M., Lensu, M., Koslof, P., Veitch, B., 1995. The life story of a first-year sea ice ridge. Cold Regions Science and Technology (23), 279-290.

Leppäranta, M., Manninen, T., 1988. The brine and gas content of sea ice with attention to low salinities and high temperatures. Tech. Rep. 1988(2), Finnish Institute of marine research, 14p.

Li, Z., Wang, Y., and Li, G. (2002). On the flexural strength of DUT-1 synthetic model ice. Cold Regions Science and Technology, (35). 67-72.

Liferov, P., Bonnemaire, B., 2005. Ice rubble behaviour and strength, Part I: Review of testing methods and interpretation of results. Cold Regions Science and Technology (41, 2), 135-151.

Maattanen, M. (1975). "On the flexural strength of brackish water ice by in-situ tests." Proceedings of the 3rd International Conference on Port and Ocean Engineering Under Arctic Conditions (POAC), 349-359.

Masterson D.M., Frederking R.M.W., Wright B., Kärnä T., Maddock W.P. 2007. A revised ice pressure-area curve. Proceedings, Nineteenth International Conf. on Port and Ocean Engineering under Arctic Conditions, Dalian, vol. 1, Dalian University of Technology Press (2007), pp. 305-314.

Muhonen A. 1991 Medium scale indentation tests—PVDF pressure measurements, ice face measurements and interpretation of crushing video. Client Report to National Research Council of Canada, Canadian Hydraulics Center by Helsinki University of Technology, Ship Laboratory, 20 February 1991.

Nadreau, J.P. and B. Michel (1984): "Ice Properties in relation to Ice Forces". Proc. 7'th Int. Assoc. of Hydr. Res. (IAHR) Ice Symposium, Vol. 4, pp. 63-115, Hamburg, West Germany.

Niskanen, T. (2005). Review of model ice tests. Technical Report AT-323 project, Arctic Technology, The University Courses on Svalbard, UNIS. 11 p. + app.

Nortala-Hoikkanen, A. (1990). FGX model ice at the Masa-yards Arctic research centre. In Proc. of the 10th Int. Symp. on Ice (IAHR), Espoo, Finland, 20-24 August 1990, 3: pp. 247-259.

Paavilainen, J., Tuhkuri, J., 2012. Parameter effects on simulated ice rubbling forces on a wide sloping structure. Cold Reg. Sci. Technol. 81, 1–10.

Palosuo, E. (1975) Formation and structure of ice ridges in the Baltic, University of Helsinki / Finish board of navigation, Helsinki, Winter navigation research board, rep no. 12, 54 p.

Park, I.K., Shin, H.S., and Ham, K.S., Cho, J.W., An Experimental Study of Roll Damping for Tanker-based FPSO, Proc. Ninth International Offshore and Polar Engineering Conference, Brest, 1999.

Peyton, H.R., 1966. Sea ice strength. University of Alaska Report UAG-182. Fairbanks: Geophysical Institute.

Ralston, T.D., 1977. Ice force design considerations for conical offshore structures. Proc. POAC'77, St. John's, Newfoundland, pp. 741-752.

Ranta, J., Polojärvi, A., & Tuhkuri, J., 2018a. Scatter and error estimates in ice loads–Results from virtual experiments. Cold Regions Science and Technology, 148, 1-12.

Ranta, J., Polojärvi, A., & Tuhkuri, J., 2018b. Limit mechanisms for ice loads on inclined structures: buckling. Cold Regions Science and Technology, 147, 34-44.

Riska K, Rantala H, Joensuu A., 1990 Full scale observations of ship–ice contact. Helsinki University of Technology, Laboratory of Naval Architecture and Marine Engineering, Report M-97, Espoo, 1990.

Rist, M., et al. (1994). "Microcracking and shear fracture in ice." Annals of Glaciology 19: 131-137.

Sanderson, T. (1988). Ice Mechanics, Risks to Offshore Structures. Graham & Trotman Inc. Kluwer Academic Publishers Group.

Schulson, E., Jones D.E. and Kuehn, G.A. (1991). "The effect of confinement on the brittle compressive fracture of ice." Annals of Glaciology 15: 216-221.

Schulson, E.M. and Duval, P. 2009. Creep and Fracture of Ice. Cambridge University Press. 401 p.

Schwarz, J. and Jochmann, P. 2001. Ice force measurements within the LOLEIF-project. Proc. International conf. on Port and Ocean Eng. under Arctic Cond (POAC), Ottawa, Ontario, Canada

Sodhi, D.S. Haynes, F.D., Kato, K. and Hirayama, K., 1983. Experimental determination of the buckling loads of floating ice sheets. Annals of Glaciology, 4, 260-265.

Surkov, G. A., 2001. Internal structure of first-year hummocks. In: Proc. of the 17th ISOPE Conf., Stavanger, Norway,17-22 June 2001.

Timco, G. (1981). On the test methods for model-ice. Cold Regions Science and Technology. Vol. 4 pp. 269-274.

Timco, G. W., & Weeks, W. F. (2010). A review of the engineering properties of sea ice. Cold Regions Science and Technology, 60(2), 107-129.

Timco, G., Croasdale, K., Wright, B., 2000. An overview of first-year sea ice ridges. Tech. Rep. HYD-R-047, PERD/CHC 5-112, Canadian Hydraulics Centre, National Research Council of Canada, 157 p.

Timco, G.W. and O.'Brienb, S., 1994. Flexural strength equation for sea ice. Cold Regions Science and Technology, 22(3), 285-298.

Tuhkuri, J. (1996). Experimental observations of brittle failure process of ice and ice-structure contact. Cold Regions Science and Technology, 265-278.

Tuhkuri, J. Lecture note of Ice Mechanics, Aalto University, Espoo, 2018.

Varsta, P. (1983). On the mechanics of ice load on ships in level ice in the Baltic Sea. PhD thesis, Helsinki University of Technology.

Vaudrey, K. (1975). Ice engineering: Elastic property studies on compressive and flexural sea ice specimens, CIVIL ENGINEERING LAB (NAVY) PORT HUENEME CA.

Vaudrey, K. D. 1977. Ice engineering: Study of related properties of floating sea-ice sheets and summary of elastic and viscoelastic analysis. US Navy Civil Engineering Lab Rept no TR-860. Port Hueneme, CA.

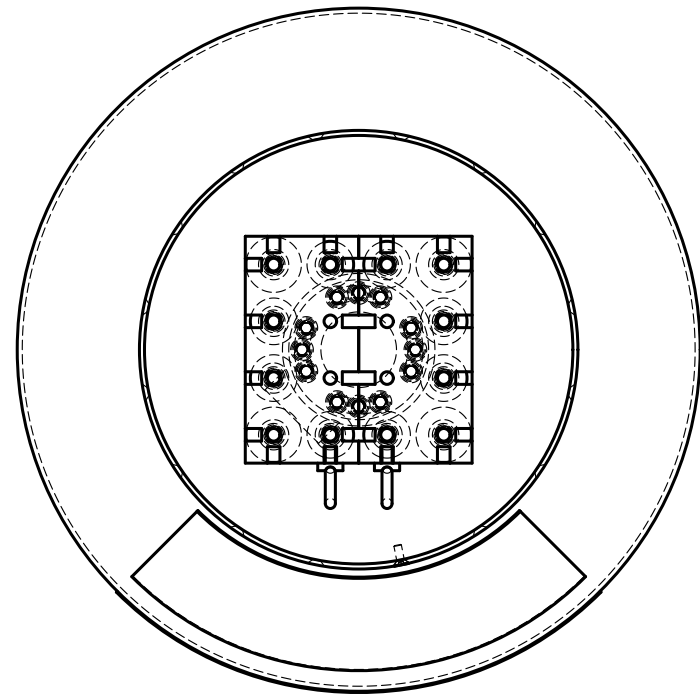Weeks, W.F. 2010. On Sea Ice. University of Alaska Press. 664 p.

List of Appendices

Appendix 1. Drawing of test structure support. 1 page.

Appendix 1. Drawing of test structure support
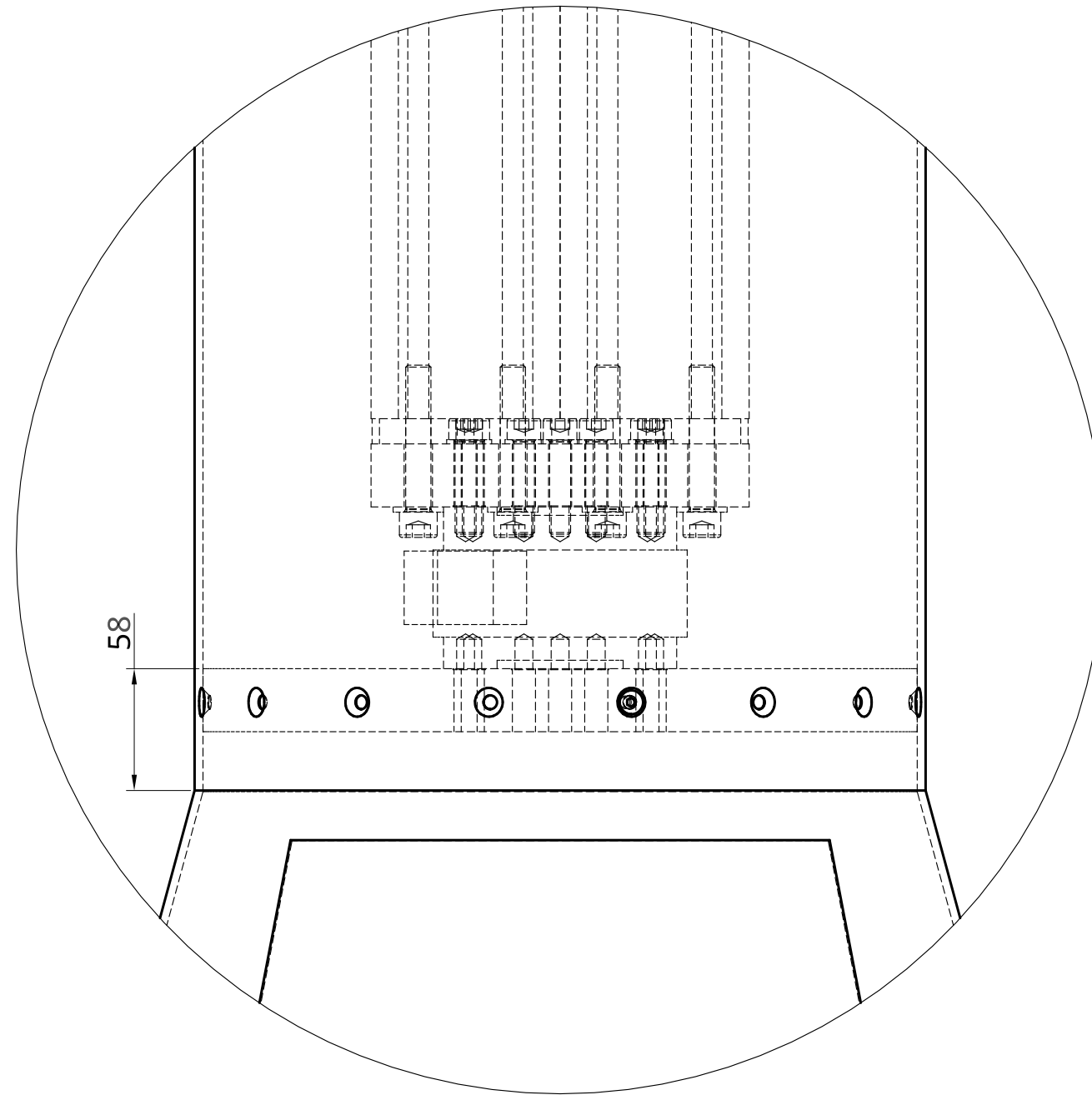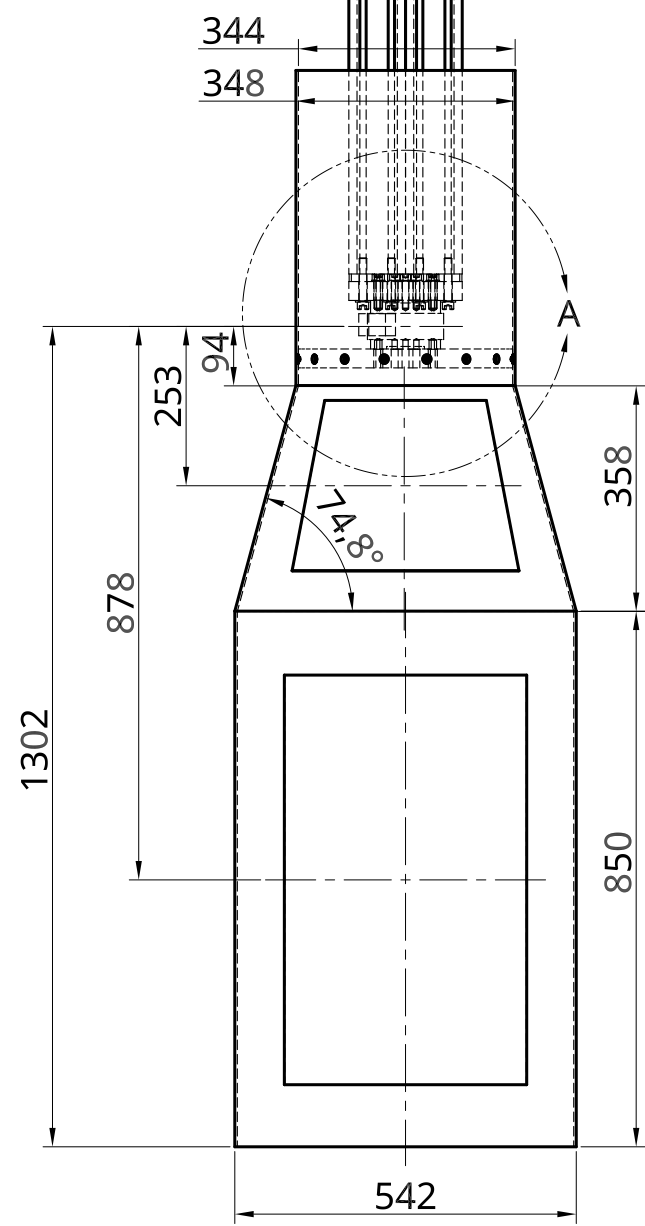
344

348

94

253

74,8°

358

878

1302

850

542

58

A

A
1:3

1:6
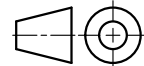
	NAME	SIGNATURE	DATE
DRAWN	OTTO PUOLAKKA		2019-06-27
CHECKED			
APPROVED			

MATERIAL   FINISH

TITLE

Hydralab+_H06
Test structure support

SIZE
A3

DWG NO.

REV.
2

SCALE   1:12   WEIGHT   SHEET   1 of 1